



Ground-based MAX-DOAS observations of tropospheric aerosols, NO₂, SO₂ and HCHO in Wuxi, China, from 2011 to 2014

Y. Wang¹, J. Lampel^{1,2}, P. H. Xie^{3,4,5}, S. Beirle¹, A. Li³, D. X Wu³, and T. Wagner¹

¹ Max Planck Institute for Chemistry, Mainz, 55128, Germany

5 ² Institute of Environmental Physics, University of Heidelberg, Heidelberg, 69120, Germany

³ Anhui Institute of Optics and Fine Mechanics, Key laboratory of Environmental Optics and Technology, Chinese Academy of Sciences, Hefei, 230031, China

⁴ CAS Center for Excellence in Urban Atmospheric Environment, Institute of Urban Environment, Chinese Academy of Sciences, Xiamen, 361021, China

10 ⁵ School of Environmental Science and Optoelectronic Technology, University of Science and Technology of China, Hefei, 230026, China

Correspondence to: Y. Wang (y.wang@mpic.de); P.H. Xie (phxie@aiofm.ac.cn)

Abstract.

15 We characterize the temporal variation and spatial distribution of nitrogen dioxide (NO₂), sulphur dioxide (SO₂), formaldehyde (HCHO) and aerosol extinctions using vertical profiles derived from long-term Multi Axis - Differential Optical Absorption Spectroscopy (MAX-DOAS) observations from May 2011 to November 2014 in Wuxi, China. A new inversion algorithm (PriAM) is implemented to retrieve profiles of the trace gases (TGs) and aerosol extinction (AE) from the UV spectra of scattered sunlight recorded by the MAX-DOAS instrument. We investigated two important aspects of the
20 retrieval process. We found that the systematic seasonal variation of temperature and pressure (which is regularly observed in Wuxi) can lead to a systematic bias of the retrieved aerosol profiles (e.g. up 20% for the AOD) if it is not explicitly considered. In this study we take this effect for the first time into account. We also investigated in detail the reason for the differences of tropospheric VCDs derived from either the geometric approximation or by the integration of the retrieved profiles, which were reported by earlier studies. We found that these differences are almost entirely caused by the limitations
25 of the geometric approximation (especially for high aerosol loads). The results retrieved from the MAX-DOAS observations are compared with independent techniques not only under cloud free sky conditions, but also under various cloud scenarios. Under most cloudy conditions (except fog and optically thick clouds), the trace gas results still show good agreement. In contrast, from the aerosol results only near-surface AEs could be still well retrieved under cloudy situations.

After a quality controlling procedure, the MAX-DOAS data are used to characterize the seasonal, diurnal, and weekly
30 variations of NO₂, SO₂, HCHO and aerosols. A regular seasonality of the three trace gases is found, but not for aerosols. Similar diurnal variations are found for SO₂, HCHO and aerosols in different seasons, but not for NO₂. Similar annual variations of the profiles are found in different years, especially for the trace gases. Considerable amplitudes of weekly cycles occur for NO₂ and SO₂, but not for HCHO and aerosols. Good correlations between the TGs and aerosols are found,



especially for HCHO in winter. Significant wind direction dependencies of the trace gases, especially for the near-surface concentrations, are found, but only a weak dependence is found for aerosol properties, especially the AOD. Our findings imply that the local emissions from the industrial area (including traffic emissions) dominate the amount of local pollutants while long distance transport might also considerably contribute to the local aerosol levels.

5 1 Introduction

Nitrogen dioxide (NO₂), sulphur dioxide (SO₂), and formaldehyde (HCHO) are important atmospheric constituents which play crucial roles in tropospheric chemistry (Seinfeld and Pandis, 1998). NO₂ is involved in many chemical cycles such as the formation of tropospheric ozone. NO₂ and SO₂ can be converted to nitrate and sulfate through the reaction with the OH radical. HCHO is formed mainly from the oxidation of volatile organic compounds (VOCs) and methane. Primary emissions of HCHO could be also important, especially in industrial regions (Chen et al., 2014). Due to the short life time of HCHO, it can be used as a measure of the level of the local VOC amount. The VOCs can then be eventually oxidized to form organic aerosols. NO₂, SO₂ and VOCs (marked by HCHO) are essential precursors of aerosols. During the industrialization and urbanization, anthropogenic emissions from traffic, heating, industry, and biomass burning have significantly increased the concentrations of these gases in the boundary layer in urban areas (Environmental Protection Agency, 1998; Seinfeld and Pandis, 1998). Nowadays, strong haze pollution events occur frequently around megacities and urban agglomerations, especially in newly industrializing countries like China, and have a significant impact on human health (Fu et al., 2014a). Recent studies found that in megacities in different regions of China most of aerosol particles are formed through photochemistry of precursor gases during haze pollution events (Crippa et al., 2014 and Huang et al., 2014). Understanding the temporal variation and spatial distribution of the trace gases (TGs) and aerosols through long-term observations is thus helpful to identify the dominating pollution sources, distinguish the contribution of transport and local emission as well as the relation between aerosols and their precursors. To accomplish this, one Multi Axis - Differential Optical Absorption Spectroscopy (MAX-DOAS) instrument was operated from 2011 to 2014 in Wuxi (China).

Since about 15 years, the MAX-DOAS technique has drawn lots of attention because of the potential to retrieve the vertical distribution of TGs and aerosols in the troposphere from the scattered sunlight recorded at multiple elevation angles (Hönninger and Platt, 2002; Hönninger et al., 2004; Bobrowski et al., 2003; Wagner et al., 2004; Van Roozendaal et al., 2003 and Wittrock et al., 2004) using relatively simple and cheap ground-based instrumentation. Ground based measurements of TG profiles are complementary to global satellite observations and allow for inter-comparisons and validation exercises (Irie et al., 2008; Roscoe et al., 2010; Ma et al., 2013; Kanaya et al., 2014; Vlemmix et al., 2015a). Using different inversion approaches, the column densities, vertical profiles and near-surface concentrations of the TGs and aerosols can be derived and provide additional information compared to in-situ monitoring or satellite observations.

The tropospheric vertical column density (VCD) of TGs is either derived by the geometric approximation (e.g. Brinksma et al., 2008) or by integration of the retrieved concentration profiles (Vlemmix et al., 2015b). The near-surface concentration



can be derived using simplified rapid methods (Sinreich et al., 2013 and Wang et al., 2014b) or directly from the derived profile. The existing profile inversion schemes developed by different groups can be subdivided into two groups: the ‘full profile inversion’ based on optimal estimation (OE) theory (Rodgers, 2000; Frieß et al., 2006, 2011; Wittrock et al., 2006; Yilmaz, 2012; Clemer et al., 2010; Irie et al., 2008, 2011; Hartl and Wenig, 2013 and Wang et al., 2013a and b) and the so called parameterization approach using look-up tables (Li et al., 2010, 2012; Vlemmix et al., 2010, 2011; Wagner et al., 2011). In comparison with the look-up table methods, the OE-based inversion algorithms are in principle easily applied to different species, different measurement locations and instruments, but they require radiative transfer simulations during the inversion and can therefore be computationally expensive for large datasets. Clemer et al. (2010), Frieß et al. (2011), Kanaya et al. (2014), Hendrick et al. (2014), Wang et al. (2014a) applied their OE approaches to long-term MAX-DOAS observations in different locations of the world. The stability or flexibility of the inversion algorithms depends on the choice of the inversion approach, the iteration scheme and the a-priori constraints (Vlemmix et al., 2015b). Designing an approach balancing stability and flexibility is quite important for long-term observations because of the occurrences of various atmospheric scenarios caused by natural variability and human activities.

In this study, we use the Levenberg-Marquardt modified Gauss-Newton numerical procedure (Yilmaz, 2012) with some modifications to optimally balance stability and flexibility, which will be referred to in the following as “**Profile inversion algorithm of aerosol extinction and trace gas concentration developed by Anhui Institute of optics and fine mechanics, Chinese academy of sciences (AIOFM, CAS) in cooperation with Max Planck Institute for Chemistry (MPIC)**” (PriAM) (Wang et al., 2013a and b). The PriAM algorithm joined the intercomparison exercise of aerosol vertical profiles retrieved from MAX-DOAS observations, between five inversion algorithms during the Cabauw Intercomparison Campaign of Nitrogen Dioxide measuring Instruments (CINDI) in summer 2009 (Frieß et al., 2016). The intercomparison displayed good agreements of the aerosol extinction (AE) profiles, AODs and near-surface AEs retrieved by the PriAM algorithm with those by other algorithms and with a collocated ceilometer instrument, a sun photometer and a humidity controlled nephelometer. In this work the PriAM is applied to the long-term MAX-DOAS observations in Wuxi, China. The retrieved results of NO₂, SO₂ and HCHO and aerosols are verified by comparisons with several independent data sets for a period longer than one year.

Under cloudy skies the retrieval algorithm could be subject to large errors because of the increased complexity of the atmospheric light paths inside clouds (e.g. Erle et al., 1995; Wagner et al., 1998, 2002, 2004; Winterrath et al., 1999), which are usually not considered in the forward model. Previous studies usually simply discard cloud-contaminated measurements. However, depending on location and season, a large fraction of measurements might be affected by clouds, e.g. about 80% of all MAX-DOAS measurements in Wuxi (Wang et al., 2015). We investigate the effect of clouds on the different MAX-DOAS retrieval results of aerosols and TGs, especially the near-surface concentrations by comparisons with results from independent techniques under various cloud scenarios. Information on different cloud scenarios is directly derived from the MAX-DOAS observations and can thus be assigned to each MAX-DOAS result without temporal interpolation. Tropospheric TG VCDs are also important for satellite validation. So far, most studies used the so called geometric



approximation to derive TG VCDs from MAX-DOAS measurements. However, considerable systematic discrepancies of tropospheric TG VCDs derived by the geometric approximation and by integration of the TG profiles are already reported in Hendrick et al. (2015), but which of the two values is closer to reality remains unclear. It is essential to answer this question in order to use a trustworthy method to determine the tropospheric TG VCDs. In this study we show evidence that the dominant error is associated with the geometric approximation, thus the TG VCDs by integration of the profiles are used for further studies here. After the series of verification exercises, the MAX-DOAS results are used to characterize temporal variations and vertical distributions of aerosols and TGs in Wuxi. The relation between aerosols and TGs are also discussed.

The paper is organized as follows: in section 2 the observations and different steps of the data analysis are described and results are verified. Moreover, the cloud effect on the retrievals and the errors of the geometric approximation are discussed. In section 3 we characterize seasonal variations and inter-annual trends, diurnal variations, weekly cycles and wind dependencies of the aerosols and TGs. The relation between aerosols and TGs are also discussed. In section 4 the results are discussed and conclusions are given.

2 MAX-DOAS measurements

2.1 MAX-DOAS in Wuxi station

A MAX-DOAS instrument developed by AIOFM shown in Fig. 1a is located on the roof of a 11-story building in Wuxi City (Fig. 1b), China (31.57°N, 120.31°E, 50 m a.s.l.) at the transition between the urban and suburban area. The suburban area with lots of farmlands is located in the east, and Taihu Lake is located in the north. The heavily industrialised area and the urban centre (living and business area) are in southwest and northwest direction of the MAX-DOAS station, respectively.

Wuxi city belongs to the Yangtze River delta industrial zone and is located about 130 km north-west of Shanghai (Fig. 1c). Wuxi is an important industrial city and has about six million inhabitants. Because of the high population density and high industrial activity, relatively high abundances of NO₂, SO₂ and VOCs are found (Fu, et al, 2013). Fig. 1d displays the mean distributions of NO₂ (Boersma et al., 2011), HCHO (de Smedt et al., 2010) and SO₂ (Theys et al., 2015) as derived from the Ozone Monitoring instrument (OMI) (Levelt et al., 2006 b). In north-west direction of Wuxi city the large industrial zone of North China plain is located, which has even higher pollution loads.

The MAX-DOAS instrument was operated by the Wuxi CAS Photonics Co. Ltd from May 2011 to December 2014. The instrument was pointed to the north and automatically recorded spectra of UV scattered sunlight at sequences consisting of five elevation angles (5°, 10°, 20°, 30° and 90°). One elevation sequence scan took about 12 min depending on the received radiance. More details of the instrument can be found in Wang et al. (2015). During the whole observation period, the instrument stopped twice: 15 December 2012 to 29 February 2013 and 16 July to 12 August 2013.



2.2 Retrievals of the tropospheric profiles of aerosol extinctions, NO₂, SO₂ and HCHO volume mixing ratios.

2.2.1 Retrieval of slant column densities

The slant column densities (SCDs) of the oxygen dimer (O₄), NO₂, SO₂ and HCHO are retrieved from scattered sunlight spectra measured by the MAX-DOAS instrument using the DOAS technique (Platt and Stutz, 2008) implemented by the WINDOAS software (Fayt and van Roozendaal, 2009). SCD represents the TG concentrations integrated along the effective atmospheric light path. The TG cross sections, wavelength ranges and additional properties of the DOAS analysis are provided in Table 1. Fig. 2 shows typical DOAS fit examples. We skip data for SZAs larger than 75 ° because of stronger absorptions of stratospheric species and low signal to noise ratio. We also skip the data with large root mean square (RMS) of the residuals and large relative intensity offset (RIO). All thresholds of the quantities used for filtering the results and the percentages of screened data of the total number of observations are listed in Table 2. Detailed discussions of the DOAS fit parameters for each species can be found in section 1 of the supplement.

2.2.2 The PriAM algorithm

In the first step of the retrieval, tropospheric vertical profiles (in the layer from the ground to the altitude of 4 km) of aerosol extinction are retrieved from the O₄ dSCDs. Afterwards, the profiles of NO₂, SO₂ and HCHO volume mixing ratios (VMRs) are retrieved from the respective dSCDs in each MAX-DOAS elevation angle sequence by using the PriAM algorithm, which is described in Wang et al., 2013a and b, both in Chinese language. We summarize the basic concept of the PriAM algorithm and its implementation settings for this study below, while details can be found in the section 2 of the supplement. In PriAM the retrieval problem is solved by the Levenberg-Marquardt modified Gauss-Newton numerical iteration procedure (Rodgers, 2000). Considering the frequent variation of aerosols and the TGs, very little is known about the expected profiles. Thus a set of fixed a-priori profiles is used for each species. A smoothed box-shaped a-priori AE profile (Boltzmann distribution) (Yilmaz, 2012), exponential a-priori profiles of NO₂ and SO₂ (similar to Yilmaz, 2012 and Hendrick et al., 2014), and a Boltzmann distribution a-priori HCHO profile (based on the MAX-DOAS and aircraft measurements in Milano during summer of 2003 reported in Wagner et al., 2011) are used by the PriAM algorithm and denoted by the grey curves in Fig. 7, respectively. Besides these standard a-priori profiles, we tested the effect of changing the profile shape and absolute value on the fit results. The description of these sensitivity tests is provided in section 2.1 of the supplement. We conclude that the standard a-priori profiles are an optimum choice for the application to the long term MAX-DOAS measurements in Wuxi. We also find that improper a-priori profiles can strongly impact the aerosol profile retrievals, but only slightly impact the TG results.

PriAM uses the radiative transfer model (RTM) SCIATRAN 2.2 (Rozanov et al., 2005). Based on the wavelength intervals of the DOAS fit, the RTM simulations are done at 370 nm for the retrieval of aerosols and NO₂, at 339 nm for HCHO and at 313 nm for SO₂. The surface height and surface albedo are set as 50 m a.s.l. and 0.05, respectively. The single scattering albedo (0.9±0.05) and asymmetry factor (Heney and Greenstein, 1941) (0.72±0.03) are chosen according to inversion



results from the Taihu AERONET station from 2011 to 2013 (the data in 2014 is unavailable). The retrieved aerosol extinction at 370 nm is converted to those around 313 nm for the SO₂ and 339 nm for the HCHO retrieval using Ångström exponents derived also from the Taihu AERONET data sets.

In addition, here it should be noted that, the Levenberg-Marquardt modified Gauss-Newton procedure is based on the assumption that the probability distribution function (pdf) of the atmospheric state (x) can be described by a Gaussian pdf (P) around the a-priori state (x_a) (Rodgers, 2000):

$$-2 \ln P(x) = (x - x_a)^T S_a^{-1} (x - x_a) + c \quad (1)$$

Here c is a constant value and S_a is the covariance matrix of the a-priori. Thus the solution can not reach the true state when the pdf of the atmospheric state (x) is skew or asymmetric (Rodgers, 2000). In this study the retrieval of the AE for extremely high aerosol loads (e.g. fog and haze) belongs to cases, which do not fulfil this assumption. In such cases the AE is underestimated by the inversion (see session 2.2.6).

2.2.3 Correcting the effect of the variation of ambient temperature and pressure

In previous studies (Clemer et al., 2010; Hendrick et al., 2014; Wang et al. 2014a) usually fixed temperature and pressure (TP) profiles are used (e.g. obtained from the US standard summer atmosphere for the measurements in China). However for locations with a significant and systematic annual variation of TP, as in this study, this simplification can affect the retrieved AODs and AE profiles (and thus also the TG profiles) systematically, yielding virtual seasonal variations. The time series of TP near the surface from the weather station nearby the MAX-DOAS instrument are shown in Fig. 3 for the year 2012 (similar patterns are found for other years, see Fig. S10 of the supplement). A regular annual variation of surface TP is obvious with amplitudes between winter and summer of about 20 K and 30 hPa, respectively. The O₄ VCDs derived from the fitted curves of surface TP (the method is described in the section 3 of the supplement) is also shown in Fig. 3. The O₄ VCD in summer is systematically lower than in winter by about 15% of the yearly mean O₄ VCD. Ignoring this systematic seasonal variation can cause a 20-30% bias of the AOD and near-surface aerosol extinction (see details in section 3 of the supplement). The error of the aerosol retrieval can further nonlinearly impact the TG profile retrievals. To account for this effect, the seasonal variation of TP and the O₄ VCD is parameterized and explicitly considered in the forward model during the MAX-DOAS retrievals by the PriAM algorithm. Figure 4 shows the AOD retrieved by PriAM using either explicit TP information or the TP profiles from the US summer standard atmosphere. The consistency of the AOD retrieved based on the explicit TP data with the simultaneous Taihu AERONET level 1.5 AOD data sets (see section 2.2.5) is better than for TP profiles from the US standard summer atmosphere.

2.2.4 Evaluation of the internal consistency of the inversion algorithm

In this section the retrieval quality is evaluated for favourable measurement conditions, namely cloud-free sky with relatively low aerosols (average AOD of about 0.6), and the performance of the retrievals in different seasons is discussed.



Comparing the measured TG dSCDs to the modelled dSCDs (the results of the forward model corresponding to the retrieved AE and TG profiles) is a direct way to evaluate how close to the real profile the retrieved profile is. Ideally, the differences between measured and modelled dSCDs are minimized by the inversion. However because of measurement errors, deviations of the forward model from reality (e.g. for cloudy skies, shown in section 2.2.6) and the not always realistic assumption of the Gauss-Newton Algorithm in Eq. (1) (especially under the condition with strong aerosol load, also shown in section 2.2.6), the derived profiles might strongly deviate from the real profiles. Figure 5 shows the mean differences (and standard deviations denoted by error bars) between the measured and modelled dSCDs for the four species during the whole measurement period. Almost symmetrical Gaussian-shape histograms of the absolute differences for the different elevation angles are found and shown in Fig. S11 of the supplement. For the aerosol retrieval, a larger negative difference of the O_4 dSCD of 2.9×10^{41} molecules² cm⁻⁵ is found for 5° elevation angle, indicating an underestimation of the aerosol extinction in the layer close to the surface; however the magnitude of the underestimation is only about 2% based on the mean O_4 dSCD of about 1.6×10^{43} molecules² cm⁻⁵ for 5° elevation angle. For the TG retrievals, in general the differences for high elevation angles are slightly larger than those for low elevation angles. This finding probably indicates the higher sensitivity of the inversion algorithm to lower altitudes. This is also indicated by the averaging kernels in Fig. 6b. Even so, the mean deviations of the dSCDs for the 30° elevation angle are only -0.28×10^{15} molecules cm⁻² for NO₂ (mean dSCD of 2.6×10^{16} molecules cm⁻²), -0.07×10^{15} molecules cm⁻² for SO₂ (mean dSCD of 3.3×10^{16} molecules cm⁻²) and 0.65×10^{15} molecules cm⁻² for HCHO (mean dSCD of 1.6×10^{16} molecules cm⁻²).

The mean averaging kernels (AKs) for retrievals of AE and the NO₂ VMR are shown in Fig. 6. AKs for SO₂ and HCHO are similar to NO₂ (see Fig. S14c and S15c of the supplement). They indicate that the inversions are sensitive to the layers from the surface up to 1.5 km. The degrees of freedom (DoF) are about 1.5 for aerosols (similar to Frieß et al., 2006), 2 for NO₂ and 2.3 for SO₂ and HCHO. AKs are generally similar for different seasons (see Fig. S12d -S15d of the supplement), indicating the consistent response of the measurements to the true atmospheric state. The slight seasonality is probably related to the variation of the SZA. The same reason probably causes the weak diurnal variation of the DoF of the inversions shown in Fig. S16 of the supplement. The averaged profiles retrieved from the measurements during the whole period and in different seasons are shown in Fig. 7 together with the corresponding a-priori profiles. The retrieved profiles below 1.5 km are quite different from the a-priori profiles, indicating that the measurements contain sufficient information for the altitude below 1.5 km. The mean contributions of the noise and the smoothing error (this error originates from the limited resolution of the inversion) of the retrievals are shown in Fig. S12b - S15b of the supplement. The total (absolute) retrieval errors have a maximum around 1 km and decrease towards the surface. The relative errors are minimal close to the surface (10% for AE, NO₂ and SO₂, and 30% for HCHO). Most of the errors originate from the smoothing error, which largely contributes to the total error at high altitudes.



2.2.5 Comparisons with independent data sets under clear skies

To validate the results from MAX-DOAS observations, the column densities and averaged concentrations in the lowest layer from 0 to 200m are compared to independent measurements:

- (a) AODs at 380 nm (level 1.5) from the sun photometer at the AERONET (Holben et al., 1998 and 2001) Taihu station. The data is downloaded from the website of <http://aeronet.gsfc.nasa.gov/>. The AERONET sun photometer is located 18 km south west of the MAX-DOAS instrument. AERONET data in the period from May 2011 to October 2013 is included in the study. In the level 1.5 data, a cloud screening scheme is used to filter most of the cloud contaminated data (Smirnov et al., 2000).
- (b) Visibilities near the ground from a forward-scattering visibility meter (Manufacturer: Anhui Landun Photoelectron Co. Ltd. Model: DNQ2 forward-scattering visibility meter) (Wang et al., 2015), which is located at the same site as the MAX-DOAS instrument. The data from May 2011 to December 2013 is available.
- (c) NO₂ and SO₂ VMRs (no HCHO data are available) near the ground from a long path DOAS (LP-DOAS) instrument (Qin et al., 2006) located at the same site as the MAX-DOAS instrument. The LP-DOAS is directed to the East with a total light path length of about 2km. The data from May 2011 to April 2012 is available

MAX-DOAS results are compared to the available independent measurements within 15 minute time difference. In this section only the data recorded during clear sky conditions with low aerosol load are compared to the MAX-DOAS results (comparisons for different cloud conditions are shown in the section 2.2.6). Almost symmetrical Gaussian-shape histograms of the absolute difference of the AODs from MAX-DOAS and AERONET for different seasons except summer are found and shown in Fig. S17a of the supplement. The averaged absolute differences and standard deviations (indicated by the error bars) of the AODs are shown in Fig. 8a. The mean differences are smaller than 0.16. The AODs from MAX-DOAS and AERONET show correlation coefficients (Pearson's product moment correlation coefficient is applied in this paper) within 0.56 to 0.91 (see Fig 9). The highest coefficient of 0.91 is found in summer, probably related to the wider range of AODs covered, but in that season also the largest absolute difference of -0.16 is found probably due to the stronger aerosol load than in other seasons. Underestimation of high aerosol amounts by MAX-DOAS will be discussed in session 2.2.6. In spring, there are several points (mostly in May of 2011 and 2012) above the 1:1 line. For this finding we have currently no explanation. Several previous studies applied a correction factor to measured O₄ dSCDs to improve the consistency between the AODs derived from MAX-DOAS and those from AERONET (e.g. Wagner et al., 2009; Clemer et al., 2010 and Frieß et al., 2016). And so far there is no credible explanation for this correction factor. In this study we don't apply any correction factor, because we achieve reasonable consistency between MAX-DOAS and AERONET results without the application of a correction factor.

The averaged AEs in the lowest layer derived from the MAX-DOAS are compared with those from the visibility meter. Here it has to be noted that both instruments do not probe exactly the same air masses: the visibility meter is sensitive to air masses at the measurement location while the MAX-DOAS is sensitive to the air masses along the line of sight for up to



several kilometres away from the instrument and up to a few hundred meters above the ground. Fig. S17b of the supplement shows almost symmetrical Gaussian-shape histograms of the absolute differences of the AEs between the two techniques. The mean differences are $< 0.18 \text{ km}^{-1}$ as shown in Fig. 8b. The highest correlation coefficient of 0.74 is found in summer probably related to the wider range of values and the stronger vertical convection, which causes a higher boundary layer and possibly a smoother vertical distribution of aerosols than in other seasons (see Fig. 10). In spring, the worst correlation is found and might be related to the occurrence of long-distance transport of dust with elevated aerosol layers (see section 3.2). The VMRs of NO_2 and SO_2 in the lowest layer derived from MAX-DOAS are compared with the values from LP-DOAS measurements for the individual seasons. Like for the AE, it has to be noted that both instruments do not probe exactly the same air masses; as the LP-DOAS yields the mean TG concentration for the light path defined by the set-up of instrument and reflector. In general the mean absolute differences are smaller than 5 ppb for NO_2 and 6 ppb for SO_2 (see Fig. 8c). Almost symmetrical Gaussian-shape histograms of the absolute differences are also found for NO_2 and SO_2 in different seasons (Fig. S17c and d of the supplement). The correlation coefficients range from 0.4 to 0.7 for NO_2 (see Fig. 11) and from 0.7 to 0.8 for SO_2 (see Fig. 12) in all seasons. The higher correlation coefficients for SO_2 than for NO_2 are probably related to the longer lifetime and thus more homogeneous vertical and horizontal distribution of SO_2 compared to NO_2 , especially in the layer from 0 to 200m. The worst correlation of NO_2 , especially in the afternoon (see Fig. S18 of the supplement) is found in summer probably because of the low NO_2 VMR near the surface, the small value range and the steep vertical gradient in the layer from 0 to 200m (see below). The generally positive absolute differences of NO_2 and SO_2 shown in Fig. 8c and d could be attributed to strong gradients in the layer from 0 to 200m as e.g. found from tower measurements in Beijing, Meng et al. (2008): they concluded that the largest values of the NO_2 and SO_2 concentrations are not directly located at the surface, but at an altitude of about 100 meters, especially in summer. However, it should be noted that the vertical gradients around Wuxi might be different from those in Beijing and thus also other reasons might contribute to the observed differences.

2.2.6 Evaluations of retrievals under cloudy and strong aerosol conditions.

The retrieval of AEs by PriAM from O_4 absorptions is based on a forward model, which does not include the effects of clouds. In principle it should be possible to also include cloud effects in the forward model (at least for horizontally homogenous clouds), but in the current version of our retrieval this is not yet accomplished. In this section, we investigate how strongly different types of clouds affect the MAX-DOAS retrieval results of aerosols and TGs. For that purpose we compare the MAX-DOAS results with independent data sets for different cloud types. For the characterization of the cloud conditions we use the cloud classification scheme described in Wang et al., 2015 (based on the concept of Wagner et al., 2014) to classify the sky conditions from the MAX-DOAS observations, i.e. radiance, colour index and O_4 absorption. The scheme differentiates between eight primary sky conditions (varying between clear skies with low aerosol load to continuous cloud cover) and two secondary sky conditions of fog and optically thick clouds. In this study we condense the eight primary sky conditions to five primary conditions by merging two types of cloud holes and two types of continuous clouds and



ignoring the rare condition of “extremely high midday CI” (Wang et al., 2015). The remaining five primary conditions are clear sky with low aerosol loads (“low aerosols”), clear sky with high aerosol loads (“high aerosol”), “cloud holes”, “broken clouds”, and “continuous clouds”. Each MAX-DOAS measurement scan is assigned to one of the five primary sky conditions. In addition, they can be assigned to the two secondary sky conditions of “fog” and “optically thick clouds”. Here it should be clarified that the “fog” sky condition does not exactly belong to the meteorology definition, but represents a sky condition derived from MAX-DOAS observations with a low visibility. In addition to the cloud effect, also the effect of high aerosol loads is evaluated (due to the unrealistic assumption of the pdf of the atmospheric state in the OE algorithm for high aerosol loads (see Eq. (1)).

Firstly measured and modelled dSCDs (results of the forward model) are compared under various sky conditions. In Fig. 13 (grey columns), the histograms of the differences between the measured and modelled dSCDs are shown for the four species (note Fig. 13 represents the differences for all non-zenith elevation angles). The histograms are symmetric and the maximum probabilities occur around zero for all four species. I.e., overall, there is no indication for a significant systematic retrieval bias. In the same figure, the relative frequencies for the different sky conditions are shown in different colours. In general, for cloudy sky conditions, especially for continuous clouds and optically thick clouds, larger discrepancies are found compared to cloud free sky conditions. The effect of clouds on the inversion is stronger for aerosols than for TGs. For the aerosol inversion, more negative differences are found for “fog”, which indicates that the strong extinction in “fog” is not well represented by the forward model (The phenomenon is also found in Fig. 15 and discussed below). To skip those inverted profiles, which probably differ largely from the real profiles, we only keep the profiles, for which the differences between measured and modelled dSCDs are smaller than 2×10^{42} molecules² cm⁻⁵ for the O₄ dSCDs (90.6% of the total observations) and 5×10^{15} molecules cm⁻² for NO₂ (89.8%), SO₂ (90.4%), and HCHO dSCDs (97.9%) for each elevation angle in one elevation sequence.

After this screening of potentially bad profiles, the mean profiles of AEs and TG mixing ratios as well as the corresponding total averaging kernels (which represent the sum of the averaging kernels at the individual altitudes) are shown in Fig. 14 for different sky conditions. While the total averaging kernels differ only slightly, the resulting profiles are quite different for different sky conditions. There are two interesting findings for the retrieved profiles: first, for all cloudy scenarios (incl. fog), the maximum AE is not found at the surface, but at higher altitudes, as observed also by Nasse et al., (2015). This can be explained by the fact that clouds act as a diffusing screen. The effect on MAX-DOAS observations is that the light paths, especially for low elevation angles, become longer than for cloud-free conditions. Consequently, also increased O₄ absorptions are measured for such conditions. A similar effect can also be caused by elevated aerosol layers. Since the forward model does not explicitly include clouds, usually elevated ‘cloud-induced’ aerosol layers are derived in the profile inversion under cloudy conditions. The diffusing screen effect depends on the cloud optical thickness. The most pronounced cloud-induced elevated aerosol layers are retrieved for optically thick clouds.

Interestingly, also for measurements under “fog” conditions, elevated aerosol layers are obtained from the MAX-DOAS inversion. This is at first sight surprising, but can be explained by two aspects: first, for most measurements classified as



“fog”, still a systematic dependence of the O_4 dSCDs on elevation angles is found, indicating that during most “fog” events the visibility is still not close to zero. Second, for most of the measurements classified as “fog” also the presence of clouds (including thick and broken clouds) was detected (Wang et al., 2015). This finding indicates that, for most observations classified as “fog”, increased aerosol scattering close to the surface occurred indeed, but at higher altitudes, even larger extinction was present. We also found a general larger value of the cost function under cloudy conditions (consistent with Fig. 13) and a systematic variation of the TG VCDs and near-surface VMRs for the different cloud scenarios. Besides measurement errors, these variations are probably also due to different photolysis rates and atmospheric dynamics (see Fig. S19 in the supplement).

In the following we compare the results from MAX-DOAS and other techniques under different sky conditions. Since the frequencies of different cloud conditions depend on season (Wang et al., 2015) and also the agreements between MAX-DOAS and other techniques were found to be different for different seasons (see section 2.2.5), the comparisons are done for individual seasons. In Figs. 15 to 19 the comparison results for autumn are shown (similar conclusion are found for other seasons and the relevant figures are shown in Fig. S20 – S23 of the supplement). Based on the comparisons of the retrieved profiles for different sky conditions (Fig. 14) and the comparison results with independent data sets (Figs. 15 – 19), we have developed recommendations, under which sky conditions which data product might be still useful or should better not be used. These recommendations, as summarized in Table 3, should not be seen as generally binding, but rather as a general indication of the usefulness of a given observation, and might change for improved inversion algorithms in the future.

In general we find that the aerosol results are more strongly affected by the presence of clouds. This is especially true for the retrieved AOD. Thus we recommend that retrieved AOD and AE profiles (except close to the surface) should not be used for all cloudy conditions. However, AE close to the surface can still well be retrieved under most cloudy conditions (except for thick clouds or fog). The TG results are less affected by clouds. Thus not only surface mixing ratios, but also TG profiles and tropospheric VCDs can still be well retrieved for most cloudy situations (except for thick clouds and fog). The MAX-DOAS data used in Section 3 are filtered by the recommendations listed in Table 3.

2.2.7 Error budgets

For the MAX-DOAS results, we derive the error estimates from different sources. Firstly we estimate the error budgets for the near surface values and column densities of the TGs and aerosols, which are summarized in Table 4. The following error sources are considered:

- (a) Smoothing and noise errors (fitting error of DOAS fits) on the near-surface values and column densities are derived from the averaged error of profiles from the retrievals (shown in Fig. S12b - S15b of the supplement), and amount on average to 10% and 6% for aerosols, 12% and 17% for NO_2 , 19% and 25% for SO_2 and 50% and 50% for HCHO, respectively.
- (b) Algorithm errors related to an imperfect minimum of the cost function, namely the discrepancy between the measured and modelled dSCDs. Based on the fact that measurements for 5° and 30° elevation angles are sensitive to the low and



high air layers, respectively, we estimate the algorithm errors on the near-surface values and the column densities using the averaged relative differences between measured and modelled dSCDs for 5° and 30° elevation angle, respectively. These errors on the near-surface values and the column densities are on average estimated at 4% and 8% for aerosols, 3% and 11% for NO₂, 4% and 10% for SO₂, 4% and 11% for HCHO, respectively.

- 5 (c) Cross section errors of O₄ (aerosols), NO₂, SO₂, and HCHO are 5%, 3%, 5% and 9%, respectively according to Thalman and Volkamer (2013), Vandaele et al. (1998), Bogumil et al. (2003) and Meller and Moortgat (2000).
- (d) The errors related to the temperature dependence of the cross sections are estimated in the following way. We firstly calculate the amplitude changes of the cross sections per kelvin using two cross sections at two temperatures from the same data sets. Then the amplitude changes per kelvin are multiplied by the variation magnitude of the ambient
 10 temperature (45 K during the whole measurement period, see Fig. 3). The corresponding systematic error of O₄ (aerosols), NO₂, SO₂ and HCHO are estimated to up to 10%, 2%, 3% and 6%, respectively.
- (e) The errors of TGs related to the errors of aerosols are estimated at 16% for VCDs and 15% for near-surface VMRs for the three TGs according to the total error budgets of aerosol retrievals.

The total error budgets on the TGs and aerosols are given by combining all the above error sources in the bottom row of
 15 Table 4. In general the sum of the smoothing and noise error is the dominant error source in the total error budget.

The error budgets of the profiles also consist of the five (four for aerosol profiles) error sources. The error (a) depends on the height, has much larger (relative) error at high altitudes and is already shown in Fig. S12b - S15b of the supplement. The error (b) can not be realistically estimated because of the difficulty of assigning discrepancies between measured and modelled dSCDs to each altitude of profiles. The error (c) and (d) have the identical number at all the altitudes and are same
 20 as the estimations for the near surface values and column densities above. The error (e) of TG profiles can be estimated as the total error budgets of aerosol profiles. However because of error (b) is unknown, the error (e) can not be quantified at the moment.

2.3 Comparisons between geometrical VCD and VCD from profile inversion

The geometric approximation (e.g. Brinksma et al., 2008) is often used to convert the dSCD for an elevation angle of α
 25 ($dSCD_{\alpha}$) to the tropospheric VCD_{geo} :

$$VCD_{geo} = \frac{dSCD_{\alpha}}{\frac{1}{\sin(\alpha)} - 1} \quad (2)$$

The elevation angles between about 30° and 20° are usually used for the application of the geometric approximation (e.g., Ma et al., 2013 and Shaiganfar et al., 2011). The tropospheric VCD (VCD_{pro}) can also be derived by the vertical integration of the retrieved profiles. The relative differences ($Diff_{total}$) between VCD_{pro} and VCD_{geo} for NO₂, SO₂ and HCHO are
 30 calculated by Eq. (3):

$$Diff_{total} = \frac{VCD_{geo} - VCD_{pro}}{VCD_{pro}} \quad (3)$$



In Fig. 20, the average relative differences for elevation angles of 30° and 20° are shown as function of the relative azimuth angle (RAA), i.e. the difference between the azimuth angles of the sun and the viewing direction of the telescope. In general, the discrepancy is larger for an elevation angle of 30° than for 20°. In addition, also an increase of the difference with increasing relative azimuth angle is found. Both findings have different magnitudes for the different TGs. The observed dependencies could be attributed to two reasons: first, the validity of the geometric approximation is limited, especially if the last scattering event occurs in the TG layer of interest. The respective probability depends on the layer height, wavelength, aerosol load and viewing geometry. A second reason for the observed differences is the uncertainty of the profile inversion. Some studies already reported systematic errors of the geometrical approximation:

- 1) Ma et al. (2013) showed that the systematic error of the NO₂ VCDs calculated by the geometrical approximation for an elevation angle of 30° is about 20% on average, which is quite similar with the value in Fig. 20b. Also, the error is larger for larger elevation angles and larger RAA, which is also consistent with the results shown in Fig. 20a and b.
- 2) The simulation studies for an elevation angle of 22° in Shaiganfar et al. (2011) show that the error of the geometrical approximation depends on the layer height of the TGs and aerosols. They found that a higher layer of TGs leads to a larger negative error. This finding is consistent with the results shown in Fig 20e, where the largest biases are found for HCHO, which has a higher layer than NO₂ and SO₂ (see Fig. 7)

To identify the dominating error source, we split the total difference ($Diff_{total}$) between VCD_{geo} and VCD_{pro} into two parts: The first part is the difference between VCD_{geo} and VCD_{geo}^m . Here VCD_{geo}^m is calculated by applying the geometric approximation to the modelled dSCD (from the forward model of the profile inversion) for the same elevation angle. This difference describes the error from the profile inversion and is referred to as $Diff_{inversion}$:

$$Diff_{inversion} = \frac{VCD_{geo} - VCD_{geo}^m}{VCD_{pro}} \quad (4)$$

The second part is the difference ($Diff_{geometry}$) between VCD_{geo}^m and VCD_{pro} :

$$Diff_{geometry} = \frac{VCD_{geo}^m - VCD_{pro}}{VCD_{pro}} \quad (5)$$

$Diff_{geometry}$ describes the error due to the limitations of the geometric approximation. $Diff_{inversion}$ and $Diff_{geometry}$ are also shown in Fig. 20 with red and blue colours, respectively. It is found that $Diff_{inversion}$ is mostly smaller than 4% for the 30° elevation angle and smaller than 2% for the 20° elevation angle. Moreover, the variation of $Diff_{total}$ along RAA is similar with $Diff_{geometry}$. Both findings clearly indicate that the error due to the limitation of the geometric approximation is the dominating error contributing to $Diff_{total}$. Moreover the systematic errors of the geometric approximation become significant when the aerosol load is large (see the section 4 of the supplement). Thus in the following, we integrate the retrieved profiles to extract the respective tropospheric VCD.



3 Results and discussion

In this section, MAX-DOAS results of column densities, near-surface concentrations and vertical profiles of aerosols and TGs are shown and discussed for a) seasonal variations and inter-annual trends, b) diurnal variations, c) weekly cycles as well as wind dependencies.

5 3.1 Meteorological conditions

The ground based weather station near the MAX-DOAS instrument records the ambient temperature, wind speed and direction, and relative humidity during the whole observation period. Fig 21 shows their seasonally mean diurnal variations. A large seasonal difference occurs only for the ambient temperature, but not for the wind speed and relative humidity. Similar diurnal variations for the three meteorology parameters are found for the different seasons. The ambient temperature and the relative humidity reach the maximum and minimum values around noon, respectively. The wind speed has the maximum value around 16:00 LT. The wind directions recorded by the same weather station are shown by the wind roses for the individual seasons in Fig. 22, indicating that the dominant wind is from the northeast in all seasons. In spring and summer the non-dominant wind directions occur more frequently than in winter and autumn.

3.2 Seasonal variations and inter-annual trends of daytime NO₂, SO₂, HCHO and aerosols

15 The time series of monthly averaged (after daily averaging) TG VCDs and near-surface VMRs as well as AODs and near-surface AEs (all the data are filtered by the recommended scheme in Table 3) derived from MAX-DOAS observations are presented in Fig. 23. Also shown are AODs and AEs obtained from AERONET and visibility meter, respectively. Similar annual variations are found for TG VCDs and near-surface VMRs. The seasonal cycles of NO₂ and SO₂ show minimum values (NO₂ and SO₂ VCD of $9\text{-}17 \times 10^{15}$ and $12\text{-}23 \times 10^{15}$ molecules cm⁻², respectively; NO₂ and SO₂ VMR of 5-11 and 4-11 ppb, respectively) in summer and maximum values (NO₂ and SO₂ VCD of $27\text{-}35 \times 10^{15}$ and $33\text{-}54 \times 10^{15}$ molecules cm⁻², respectively; NO₂ and SO₂ VMR of 12-16 ppb and 14-18 ppb) in winter. These characteristics are already well-known over urban areas in the eastern China region (Richter et al., 2005, Ma et al., 2013; Hendrick et al., 2014, Qi et al, 2012 and Wang et al., 2014a). In contrast, HCHO shows an opposite seasonality compared to NO₂ and SO₂. The HCHO VCD and near-surface VMR are $16\text{-}20 \times 10^{15}$ molecules cm⁻² and 4-6 ppb in summer, respectively, $7\text{-}10 \times 10^{15}$ molecules cm⁻² and 2-4 ppb in winter, respectively. A similar seasonality of HCHO in the eastern China region was already reported by De Smedt et al., (2010 and 2015).

For AOD and AE no pronounced seasonal cycle is found. The MAX-DOAS results mostly reveal similar levels like the other two techniques. Note that the data in 2014 is not available from both the AERONET Taihu station and the visibility meter. The AOD is typically larger than 0.7 and the AE typically larger than 0.5 km⁻¹. Note that the extremely low values in July and August of 2013 are unrepresentative because of low statistics caused by the temporal shutdown of the instrument (see Fig. 23c).



The observed seasonal variations of the different species are related to three factors: the seasonal variation of emissions (or chemistry formation mechanism), removal mechanisms, and atmospheric transports (Wang et al., 2010; Lin et al., 2011). Different from the column densities, the near-surface concentrations of all species can be systematically affected by the seasonality of the boundary layer (BL) height (Baars et al., 2008). The compression effect of the lower BL height in winter than in summer systematically increases the near-surface concentrations.

The details for the different species are discussed as follows:

1) NO₂ and SO₂

NO₂ (rapidly formed from NO_x after its emission) and SO₂ originate mostly from direct emissions. It is assumed that about 94% of total NO_x emission in the Wuxi region is emitted from the power plants, industrial fuel combustions and vehicles (Huang et al., 2011), which emit similar amounts in different seasons. Thus the seasonal variation of the MAX-DOAS results cannot be explained by the variation of the NO_x emissions. However, the SO₂ emissions might vary by about 20% due to the seasonal use of boilers for domestic heating (Huang et al., 2011). Because of the short lifetime of NO_x under urban pollution (about some hours, e.g. Beirle et al., 2011 and Liu et al., 2015), most NO_x should be from local emissions (Liu et al., 2015), and NO_x long-range transport could be negligible in Wuxi. It needs to be noted that because of the longer life time of NO_x in winter (Schaub et al., 2015) than in summer, transport of NO₂ from a nearby pollution area in winter might play a role on the seasonality of NO₂. Due to the large range of SO₂ residence time (from less than one hour to 2 weeks and longer in winter than in summer, e.g. von Glasow et al., 2009; Lee et al., 2011; Beirle et al., 2014), transport from the highly polluted regions in the east and north likely play a role, especially in winter. Here it is interesting to note that indications for long range transport of SO₂ are also found in the elevated SO₂ profiles in winter as shown in Fig 25b. Because of the strong seasonal variation of the SO₂ emissions due to domestic heating in the North (Wang et al., 2014a), long range transport from these regions could strongly impact the SO₂ amount in Wuxi in winter, thus contributing to the seasonality. In conclusion, the seasonality of NO₂ can be mostly attributed to the removal mechanisms due to the OH radical, which has a minimum in winter and maximum in summer (Stavrakou et al., 2013). The same removal mechanism could be partly responsible for SO₂ seasonality (Lee et al., 2011). Additional heterogeneous reactions (Oppenheimer et al., 1998) might also play a role. Since we find a high correlation between the NO₂ and SO₂ VCDs and near surface VMRs (see Fig. S24 of the supplement), we conclude that also for SO₂ the seasonality of the removal mechanism is the most important factor controlling the seasonality of the SO₂ VCDs and near-surface VMRs.

2) HCHO

HCHO originates mainly from the oxidation degradation of many VOCs by the OH radical. But because the OH radical also plays a role in the removal mechanism of HCHO, the seasonal variation of the OH radical level contributes to the seasonality of HCHO in a complex way. Apart from the ubiquitous background levels of HCHO from the methane oxidation, emissions of non-methane VOCs (NMVOCs) (including HCHO) from biogenic sources, biomass burning and anthropogenic sources control local HCHO concentrations. Therefore, in addition to the seasonality of OH, also the seasonal variations of the VOC emissions should be important factors for the HCHO seasonality. Firstly stronger biogenic emissions are expected in the



growing period, namely from spring to autumn. Based on a study in Beijing (Xie et al., 2008) a relative contribution of biogenic emissions to the total VOC levels is estimated at about 13%. Secondly, biomass burning events frequently occur in May and June (Cheng et al., 2014) in the Wuxi region. Thirdly anthropogenic emissions contribute a lot to the VOCs amounts. However the dominating sources, such as non-combustion industrial processes and vehicles (Huang et al., 2011), do not show an obvious seasonality. Thus, their effect on the HCHO seasonality can be probably ignored. Fourth, biogenic primary emissions of HCHO could be another factor contributing to the HCHO seasonality due to its significant differences between in summer and winter (Chen et al., 2014).

3) Aerosols

The local aerosol sources, including primary aerosol emissions and secondary aerosol formations, and transport of aerosols can in principle both contribute to the local aerosol amount. The contribution of transported aerosols has an obvious seasonality: In May and June, the transport from biomass burning might contribute to up to 37% of the PM_{2.5} amount based on a case study in summer 2011 (Cheng et al., 2014). In spring and autumn dust storms from Mongolia can reach Wuxi (Liu et al., 2012; Fu et al., 2014b and Li et al., 2014). The polluted air from the eastern area (for example, Shanghai) and northern area (for example Jing-Jin-Ji region) (Jiang et al., 2015) could also move to Wuxi under appropriate meteorological conditions (Liu et al., 2012). Haze events frequently occur in autumn and winter (Fu et al., 2014a).

The inter-annual trends of TGs and aerosols are presented in Fig. 24. Because of missing observations in some months and inner-annual variations of abundances of the species, only data in May to November are used. SO₂ shows a clear decreasing trend from 2011 to 2014. However NO₂, HCHO and aerosols almost maintain constant amounts.

The monthly mean profiles of NO₂, SO₂ and HCHO (under clear and cloudy sky conditions except thick clouds and fog) and aerosols (only under clear sky conditions) (screened by the scheme in Table 3) are presented in Fig. 25. The monthly mean TG profiles under clear sky conditions (see Fig. S25 of the supplement) are almost identical to those under various sky conditions except fog and thick clouds in Fig. 25. During all seasons, NO₂ shows an exponentially decreasing profile (see Fig. 25a). On average the NO₂ VMR at 0.5 km is about half of the near-surface VMR and it rapidly decreases above 0.5km to about 2 ppb at 1.5 km. Aircraft measurements of NO_x in October 2007 in the Yangtze River Delta region by Geng et al. (2009) presented similar vertical profiles. The profile shape of NO₂ can be mostly attributed to its near-surface emission sources and short life time.

The SO₂ layer is found at a higher altitude compared to NO₂ (see Fig. 25b). A more box-like shape up to the altitude of about 0.7km to 1km is found in autumn and winter when the SO₂ load is large and also long-range transport might effectively contribute to the SO₂ amounts in Wuxi. In contrast, for the rather small SO₂ loads in summer, an exponential profile shape is found. Similar profile shapes are also obtained from aircraft measurements during September to October of 2007 over Wuxi (Xue et al., 2009). One interesting finding is the lofted SO₂ layer at around 0.7 km in February and March 2012, which is probably related to long distance transport from a heavily polluted region. This interpretation is supported by the dominating wind direction (coming from the nearby polluted area around Shanghai) in March 2012 (see Fig. S26 of the supplement) compared to other years.



In all seasons, the HCHO profile shape consists of three parts (see Fig. 25c): a decrease from the surface to about 0.3 km, an almost constant value from about 0.3 km to about 1.1 km, and a steep decrease above. The high values at the surface are probably caused by primary emissions and rapid formation from particular VOCs near the surface. Transport of longer lived VOCs to higher altitudes and subsequent destruction probably contributes to the increased values at up to about 1 km. While other measurements of tropospheric profiles of HCHO are not available around Wuxi, it is still reasonable to compare our results with the aircraft measurements of HCHO over Bresso near Milano during summer of 2003 (Junkermann, 2009; Wagner et al., 2011) because both of the measurements took place in polluted urban regions. They found a layer height with high HCHO concentration values of up to 1km and the highest values were found normally close to the ground. This feature is consistent with our results in Wuxi.

Fig. 25d shows the aerosol profiles representing a box-like shape near the surface and an exponential decrease above 0.5 to 1 km. The box-like part in winter is systematically lower than in other seasons probably due to the lower BL in winter. Baars et al. (2008) reported such a seasonal dependence of the top height of the BL obtained by lidar observations in Germany over a one-year period. A similar seasonal dependence of the BL can be expected in Wuxi. From May to October the highest aerosol extinction is found at an elevated altitude of up to 0.7km, especially in 2014. This feature could indicate long distance transports of aerosols, probably from biomass burning events.

3.3 Diurnal variations of NO₂, SO₂, HCHO and aerosols

Fig. 26 shows the seasonally averaged diurnal variations of TG VCDs and near-surface VMRs as well as AODs and near-surface AEs from 2011 to 2014. The morning and afternoon averaged profiles of aerosols and TGs are also shown in winter and summer, respectively, in Fig. S27 of the supplement. The diurnal variations can probably be attributed to the complex interaction of the primary and secondary sources, depositions and atmospheric transport processes in the BL. The diurnal variation of the BL height (Baars et al., 2008) can systematically affect the diurnal patterns of near-surface VMRs and AEs, but has almost no impact on the TG VCDs and AOD.

As seen in Fig. 26a, the seasonality of the diurnal variation of the NO₂ VCDs is quite similar to the MAX-DOAS observations in Beijing (Ma et al., 2013). They conclude that the phenomenon is probably caused by the complex interplay of the emission, chemistry and transport, with generally higher emission rates and a longer NO₂ lifetime in winter. In Fig. 26b, the SO₂ VCD shows almost constant values during the whole day in summer (with a slight decrease in the afternoon). In winter high values persist until 13:00 LT and then rapidly decrease. In autumn and spring the highest values occur around noon. The SO₂ variation mostly happens in the layer below 0.5 km (see Fig. S27 of the supplement). The variation features are different from the observations in Beijing (Wang et al., 2014a), probably caused by different sources, transport and life time at the two locations. In Fig. 26c it is shown that the HCHO VCDs increase rapidly after sunrise with a faster increase in summer. HCHO has a stronger variation at the layer from 0.5km to 1km. This diurnal pattern is probably mainly related to the photochemical formation of HCHO and the VOCs emitted by vehicles and biogenic emissions (Kesselmeier and Staudt, 1999). In Fig. 26d similar relative diurnal variations of AODs and AE are found for the different seasons. The decrease of



AOD from sunrise to around 9:00 LT might be caused by the decrease of the relative humidity after sunrise as shown in Fig. 21c. The increase of AOD from about 9:00 LT to noon might be caused by the photochemical formation of second aerosol particles. The decrease of AOD in the afternoon might indicate a reduced formation reaction rate.

3.4 Weekly cycles of NO₂, SO₂, HCHO and aerosol extinction

5 In urban areas, anthropogenic sources often control the amounts of pollutants. Because human activities are usually strongest during the working days, weekly cycles of NO₂, SO₂, HCHO and aerosols can provide information on the contributions from natural and anthropogenic sources (Beirle et al., 2003 and Ma et al., 2013). As shown in Fig. 27, weekly cycles are found for NO₂ and SO₂. The relative differences of the VCDs and near-surface VMRs between the average working day level (from Monday to Friday) and the value on Sunday are 11% and 18% for NO₂, 13% and 11% for SO₂, respectively. For HCHO
10 smaller weekly cycles (7% of VCD and 12% of near-surface VMR) are found. In contrast, no clear weekend reduction is found for aerosols. The negligible weekly cycle of aerosols is probably caused by the rather long life time of aerosols and the effect of long-range transport, e.g. from biomass burning and dust. Fig. S28 of the supplement shows that the diurnal variations of the three TGs are almost the same on different days of a week indicating similar sources during the working days and weekends.

15 3.5 Source analysis of the pollutants

3.5.1 Relation between the precursors and aerosols

Huang et al. (2014) showed that secondary aerosols including organic and inorganic aerosols (nitrates and sulfates) contribute to about 74% of the PM_{2.5} mass collected during high pollution events in January 2013 at the urban site of Shanghai. The aerosol in Wuxi close to Shanghai is expected to have similar properties. NO_x (NO₂ and NO) and SO₂ are the
20 precursors of secondary inorganic aerosols through their conversion into nitrates and sulfates, respectively. HCHO can be used as a proxy for the local amount of VOCs, which are precursors of secondary organic aerosols (Claeys et al., 2004). We have investigated the relationship between aerosols and their precursors through a correlation study as in Lu et al. (2010), Veefkind et al. (2011) and Wang et al. (2014a). Table 5 lists the correlation coefficients between the TG VCDs and AODs as well as the TG VMRs and AEs near the surface. The correlations of near-surface values are always higher than those of the
25 column densities. This finding could be probably explained by the effect of long-range transport, which typically occurs at elevated layers. For long-range transport, the effect of different atmospheric lifetimes is especially large probably leading to weaker correlations between the aerosol and its precursors. In contrast, close to the surface, local emissions dominate the concentrations of TG and aerosols and the effect of different lifetimes is negligible.

In general, correlations in spring are worst probably due to the transport of dust and biomass burning aerosols. The
30 correlations between aerosols and HCHO are higher in winter than in summer. This finding may be explained by the fact that anthropogenic emissions dominate the (primary and secondary) sources of HCHO and aerosols simultaneously in winter.



Meanwhile the correlations between aerosols and HCHO are higher than those between aerosols and NO₂ or SO₂ in winter and autumn. This finding can be possible explained by the fact that both HCHO and aerosols are dominated by secondary sources, while NO₂ and SO₂ are mostly from primary emissions in this region.

3.5.2 Wind dependence of the pollutants

5 The MAX-DOAS station is located on the boundary of the urban and suburban areas as shown in Fig. 1b. Several iron factories, cement factories, and petroleum industries are operated in the south-west industrial area. The industrial activities and vehicle operations in the industrial area lead to significant emissions of NO₂, SO₂, VOCs as well as aerosols (Huang et al., 2011). In the urban centre area, traffic, construction sites and other anthropogenic emissions emit significant amounts of NO₂, VOCs as well as particles. Some factories, such as an oil refinery, are located in the north-west of the urban centre,
10 emitting pollutants including SO₂ and VOCs. In addition, one power plant located at about 50km in the north and the Suzhou city in the south-east direction of the MAX-DOAS station might contribute to the observed pollutants in Wuxi depending on the meteorological condition.

We analysed the distributions of column densities and near-surface values of the TGs and aerosols for different wind directions in Fig. 28. In principle, the near surface pollutants are expected to be dominated by nearby emission sources,
15 while the column densities can be additionally affected by transport of pollutants from remote sources. Long-range transport can weaken the dependence of the column densities on the wind direction because of the complex trajectories the air masses might have followed. For all four species, the highest values are observed for south-westerly winds, especially for the near-surface pollutants. This finding implies that the industrial area emits large amounts of NO_x, SO₂, VOCs and aerosols. Fig. 28c shows that the HCHO southwest peak is only present in winter. This finding is probably caused by the fact that in winter anthropogenic sources (of precursors and direct HCHO emissions) dominate the HCHO amounts, while in other seasons natural sources dominate the HCHO amounts. Another peak of NO₂ and SO₂ is found in the northwest, obviously in winter, indicating considerable emissions in the urban centre. Fig 28d shows a weaker dependence of AODs on the wind direction than the VCDs of the TGs, which probably indicates the stronger contribution of long-range transport to the local aerosol levels compared to the TGs. In addition for daily averaged wind speed of smaller than 1 m/s, the averaged TGs VCDs and
25 near-surface VMRs are higher than those for larger wind speeds (shown in Fig. 29a and b), indicating that dispersion of local emissions is more important than the transport from distant sources. For aerosols, a wind speed dependency is only observed for near-surface AEs, but not for AODs (see Fig. 29c), indicating the higher importance of transport for aerosols than for TGs.

4 Conclusions

30 The long-term characteristics of the spatial and temporal variation of NO₂, SO₂, HCHO and aerosols in Wuxi (part of the Yangtze River delta region) are characterized by automatic MAX-DOAS observations from May 2011 to Dec 2014. The



PriAM OE-based algorithm was applied to MAX-DOAS observations to acquire vertical profiles, VCDs (AODs) and near-surface VMRs (AEs) of TGs (aerosols) in the layer from the surface to an altitude of about 3 km.

The AODs and near-surface AEs and the VMRs of NO₂ and SO₂ from MAX-DOAS are compared with coincident data sets (for one year) obtained by a sun photometer at the AERONET Taihu station, a nearby visibility meter and a LP-DOAS, respectively. In general good agreement was found: Under clear sky conditions, correlation coefficients of 0.56–0.91 for AODs, 0.31–0.71 for AEs, 0.42–0.64 for NO₂ VMRs and 0.68–0.81 for SO₂ VMRs as well as the low systematic bias of -0.16–0.029 for AODs, 0.05–0.19 km⁻¹ for AEs, -2.23–5.11 ppb for NO₂ VMRs and 1.8–6.1 ppb for SO₂ VMRs are found in different seasons.

Further comparisons were performed for different cloud conditions identified by the MAX-DOAS cloud classification scheme (Wagner et al., 2014 and Wang et al., 2015). For most cloud conditions (except optically thick clouds and fog) similar agreement as for clear sky conditions is found for the results of near-surface TG VMRs and AEs. However, the AOD results are more strongly affected by clouds and we recommend to only retrieve near-surface AEs for cloudy observations. In the presence of fog and optically thick clouds, no meaningful profile inversions for TGs and aerosols are possible. Thus for further interpretations, we considered TG results and near-surface AEs for clear and cloudy sky conditions (except fog and optically thick clouds), but AOD only for clear sky conditions.

In this study we also investigated two important aspects of the MAX-DOAS data analysis: For the first time the effect of the seasonality of temperature and pressure on the MAX-DOAS retrievals of aerosols was investigated. Such an effect is especially important for the measurements in Wuxi, because strong and systematic variations of temperature and pressure are regularly found. Accordingly the O₄ VCD changes systematically with seasons, which was in our study for the first time explicitly taken into account for the aerosol profile retrieval. It was shown that without this correction, deviations of the AOD of up to 20% can occur.

Moreover, we systematically compared trace gas VCDs derived either by the so-called geometric approximation with those derived by integration of the derived vertical profiles. Such discrepancies were reported in previous studies. We could show that the difference between both methods can be clearly assigned to limitations of the geometric approximation. This error becomes especially significant when the aerosol load is strong, which is the situation in most industrialised regions. Thus we conclude that in general the integration of the retrieved profiles is the more exact way to extract the tropospheric TG VCDs, and we used this method in this study.

A prominent seasonality of all TGs is found in agreement with many previous studies based on satellite and ground-based observations. NO₂ and SO₂ have maxima and minima in winter and summer, respectively, while HCHO has an opposite seasonality. No pronounced seasonality of aerosols is found. From 2011 to 2014, only SO₂ shows a clear decreasing trend, while NO₂, HCHO and aerosol levels stay almost constant.

Different profile shapes are found for the different species: for NO₂ exponentially decreasing profiles with a scale height of about 0.6km are observed in different seasons. SO₂ profiles extend to slightly higher altitudes than NO₂, probably due to the



longer lifetime of SO₂. Especially in winter often elevated layers of enhanced SO₂ are found between about 0.7km and 1km (especially in early 2012), probably indicating the importance of long range transport of SO₂. HCHO reaches up to even higher altitudes (up to > 1 km) than NO₂ and SO₂, probably indicating the effect of the secondary formation from VOCs. However, typically the largest HCHO VMRs are still found near the surface (like for NO₂ and SO₂). The aerosol profiles
5 typically show constant values close to the surface (below about 0.5km), but decrease exponentially above that layer. Especially in winter often elevated layers (between 0.5km and 0.7km) are observed.

Different diurnal variations are found for the different species: For the NO₂ VCDs, depending on season, a decrease or increase is found during the day. For the NO₂ VMRs and SO₂ VCDs and VMRs, typically a slight decrease during the day is observed. The diurnal variations of HCHO and aerosols are more complex and show a pronounced maximum around noon in
10 summer indicating photochemical production. Systematic weekly cycles occur for NO₂ and SO₂ with the maximum values on Thursday or Friday and minimum values on Sunday indicating a large contribution of anthropogenic emissions. In contrast, the amplitudes of the weekly cycles for HCHO and aerosols are rather small.

We performed correlation analyses between the different TG results versus the aerosol results for individual seasons. For all TGs and seasons positive correlations (correlation coefficient between 0.12 and 0.65) were found with the highest
15 correlations in winter. In general the highest correlation is found for HCHO in winter probably indicating a similar secondary formation process for both species. In general, higher correlations are found for the near-surface products (VMRs versus AE) compared to the column products (VCDs versus AOD).

We found a clear wind direction dependence of TG and aerosols results, especially for the near-surface concentrations. The dependencies indicate that the largest sources of the observed pollutants in Wuxi are anthropogenic emissions from the
20 nearby industrial area (including traffic emissions). In addition the obvious lower TG results for high wind speed than for low wind speed indicate that the dispersion of local emissions is more important than the transport from distant sources. Interestingly, for HCHO, a considerable dependence on the wind direction is only observed in winter probably indicating significant VOC emissions from natural sources in the growing seasons.

The data sets of the TGs and aerosols are also valuable to validate tropospheric products from satellite observations and
25 chemical transport models. This study is in progress.

Acknowledgements: We thank the Wuxi CAS Photonics Co. Ltd for their contributions to operate the observations of the MAX-DOAS instrument, the long path DOAS instrument, the visibility meter and the weather station in Wuxi. We thank the Institute of Remote Sensing / Institute of Environmental Physics, University of Bremen, Bremen, Germany for their freely
30 accessible radiative transfer model SCIATRAN. We thank Belgian Institute for Space Aeronomy (BIRA-IASB), Brussels, Belgium for their freely accessible WINDOAS software and generating the mean map of SO₂ and HCHO tropospheric VCDs derived from OMI observations over eastern China. We thank Goddard Space Flight Center, NASA for their freely accessible archive of AERONET data. We thank Prof. Ma Ronghua in Nanjing Institute of Geography & Limnology Chinese Academy of Sciences for his effort to operate the Taihu AERONET station. We thank Royal Netherlands



Meteorological Institute for their freely accessible archive of OMI tropospheric NO₂ data. We thank Trissevgeni Stavrakou in BIRA-IASB, Hang Su and Yangfang Cheng in MPIC for their help to interpret the correlations between aerosols and the trace gases. This work was supported by Max Planck Society-Chinese Academy of Sciences Joint Doctoral Promotion Programme, and National Natural Science Foundation of China (Grant No.: 41275038 and 41530644) and Monitoring and
5 Assessment of Regional air quality in China using space Observations, Project Of Long-term sino-european co-Operation (MarcoPolo), FP7 (Grant No: 606953).

10

References

- Aliwell, S. R., Van Roozendaal, M., Johnston, P. V., Richter, A., Wagner, T., Arlander, D. W., Burrows, J. P., Fish, D. J., Jones, R. L., Tørnkvist, K. K., Lambert, J.-C., Pfeilsticker, K., and Pundt, I.: Analysis for BrO in zenith-sky spectra: An intercomparison exercise for analysis improvement, *J. Geophys. Res.*, 107, D140, doi:10.1029/2001JD000329, 2002.
- 15 Baars, H., Ansmann, A., Engelmann, R., and Althausen, D.: Continuous monitoring of the boundary-layer top with lidar, *Atmos. Chem. Phys.*, 8, 7281-7296, doi:10.5194/acp-8-7281-2008, 2008.
- Beirle, S., Platt, U., Wenig, M., and Wagner, T.: Weekly cycle of NO₂ by GOME measurements: a signature of anthropogenic sources, *Atmos. Chem. Phys.*, 3, 2225–2232, doi: 10.5194/acp-3-2225-2003, 2003.
- Beirle, S., Boersma, K. F., Platt, U., Lawrence, M. G., and Wagner, T.: Megacity emissions and lifetimes of nitrogen oxides
20 probed from space, *Science*, 333, 1737–1739, 2011.
- Beirle, S., Hörmann, C., Penning de Vries, M., Dörner, S., Kern, C., and Wagner, T.: Estimating the volcanic emission rate and atmospheric lifetime of SO₂ from space: a case study for Kīlauea volcano, Hawai'i, *Atmos. Chem. Phys.*, 14, 8309-8322, doi:10.5194/acp-14-8309-2014, 2014.
- Bobrowski, N., Honninger, G., Galle, B. and Platt, U.: Detection of bromine monoxide in a volcanic plume, *Nature*, 423,
25 273–276, 2003.
- Boersma, K. F., Eskes, H. J., Veefkind, J. P., Brinksma, E. J., van der A, R. J., Sneep, M., van den Oord, G. H. J., Levelt, P. F., Stammes, P., Gleason, J. F. and Bucsela, E. J.: Near-real time retrieval of tropospheric NO₂ from OMI, *Atmos. Chem. Phys.*, 7, 2103–2118, 2007.
- Boersma, K.F., H.J. Eskes, R. J. Dirksen, R. J. van der A, J. P. Veefkind, P. Stammes, V. Huijnen, Q. L. Kleipool, M. Sneep,
30 J. Claas, J. Leitao, A. Richter, Y. Zhou, and D. Brunner, An improved retrieval of tropospheric NO₂ columns from the Ozone Monitoring Instrument, *Atmos. Meas. Tech.*, 4, 1905-1928, 2011.



- Bogumil, K., Orphal, J., Homann, T., Voigt, S., Spietz, P., Fleischmann, O. C., Vogel, A., Hartmann, M., Kromminga, H., Bovensmann, H., Frerick, J., and Burrows, J. P.: Measurements of molecular absorption spectra with the SCIAMACHY pre-flight model: instrument characterization and reference data for atmospheric remote-sensing in the 230–2380 nm region, *J. Photoch. Photobio. A*, 157, 167–184, 2003.
- 5 Brinksma, E. J., Pinardi, G., Volten, H., Braak, R., Richter, A., Schönhardt, A., van Roozendaal, M., Fayt, C., Hermans, C., Dirksen, R. J., Vlemmix, T., Berkhout, A. J. C., Swart, D. P. J., Oetjen, H., Wittrock, F., Wagner, T., Ibrahim, O. W., de Leeuw, G., Moerman, M., Curier, R. L., Celarier, E. A., Cede, A., Knap, W. H., Veeffkind, J. P., Eskes, H. J., Allaart, M., Rothe, R., PETERS, A. J. M., and Levelt, P. F.: The 2005 and 2006 DANDELIONS NO₂ and aerosol intercomparison campaigns, *J. Geophys. Res.*, 113, D16S46, 2008.
- 10 Chen, W. T., Shao, M., Lu, S. H., Wang, M., Zeng, L. M., Yuan, B., and Liu, Y.: Understanding primary and secondary sources of ambient carbonyl compounds in Beijing using the PMF model, *Atmos. Chem. Phys.*, 14, 3047–3062, doi:10.5194/acp-14-3047-2014, 2014.
- Cheng, Z., Wang, S., Fu, X., Watson, J. G., Jiang, J., Fu, Q., Chen, C., Xu, B., Yu, J., Chow, J. C., and Hao, J.: Impact of biomass burning on haze pollution in the Yangtze River delta, China: a case study in summer 2011, *Atmos. Chem. Phys.*, 14, 4573–4585, doi:10.5194/acp-14-4573-2014, 2014.
- 15 Claeys, M., Graham, B., Vas, G., Wang, W., Vermeylen, R., Pashyn-ska, V., Cafmeyer, J., Guyon, P., Andreae, M. O., Artaxo, P., and Maenhaut, W.: Formation of secondary organic aerosols through photooxidation of isoprene, *Science*, 303, 1173–1176, 2004.
- Clemer, K., Van Roozendaal, M., Fayt, C., Hendrick, F., Hermans, C., Pinardi, G., Sperr, R., Wang, P., and De Maziere, M.: Multiple wavelength retrieval of tropospheric aerosol optical properties from MAXDOAS measurements in Beijing, *Atmos. Meas. Tech.*, 3, 863–878, 2010.
- 20 Crippa, M., Ciarelli, G., Piazzalunga, A., Schwikowski, M., Abbaszade, G., Schnelle-Kreis, J., Zimmermann, R., An, Z., Szidat, S., Baltensperger, U., El Haddad, I., and Prevot, A. S.: High secondary aerosol contribution to particulate pollution during haze events in China, *Nature*, 514, 218–222, 2014.
- 25 De Smedt, I., Stavrou, T., Müller, J. F., van der A, R. J., and Van Roozendaal, M.: Trend detection in satellite observations of formaldehyde tropospheric columns, *Geophys. Res. Lett.*, 37(18), L18808, doi:10.1029/2010GL044245, 2010.
- De Smedt, I., Stavrou, T., Hendrick, F., Danckaert, T., Vlemmix, T., Pinardi, G., Theys, N., Lerot, C., Gielen, C., Vigouroux, C., Hermans, C., Fayt, C., Veeffkind, P., Müller, J.-F., and Van Roozendaal, M.: Diurnal, seasonal and long-term variations of global formaldehyde columns inferred from combined OMI and GOME-2 observations, *Atmos. Chem. Phys.*, 15, 12519–12545, doi:10.5194/acp-15-12519-2015, 2015.
- 30 Environmental Protection Agency: National air quality and emissions trends report 1998, Rep. EPA 454/R-00-003, 1998.
- Erle, F., Pfeilsticker, K., Platt, U., On the influence of tropospheric clouds on zenith scattered light measurements of stratospheric species, *Geophys. Res. Lett.*, 22, 2725–2728, 1995.



- Fayt, C. and van Roozendael, M.: WinDOAS 2.1 Software User Manual, IASB/BIRA (<http://www.oma.be/GOME/GOMEBro/WinDOAS-SUM-210b.pdf>), 2009.
- Frieß U., Monks, P. S., Remedios, J. J., Rozanov A., Sinreich R., Wagner T., and Platt, U.: MAX-DOAS O₄ measurements: A new technique to derive information on atmospheric aerosols: 2. Modeling studies, *J. Geophys. Res.*, 111, D14203, 2006, doi:10.1029/2005JD006618.
- Frieß U., Sihler H, Sander R. The vertical distribution of BrO and aerosols in the Arctic: Measurements by active and passive differential optical absorption spectroscopy, *J. Geophys. Res.*, 116, D00R04, 2011.
- Frieß U., Klein Baltink, H., Beirle, S., Clèner, K., Hendrick, F., Henzing, B., Irie, H., de Leeuw, G., Li, A., Moerman, M. M., van Roozendael, M., Shaiganfar, R., Wagner, T., Wang, Y., Xie, P., Yilmaz, S., and Zieger, P.: Intercomparison of aerosol extinction profiles retrieved from MAX-DOAS measurements, *Atmos. Meas. Tech. Discuss.*, doi:10.5194/amt-2015-358, 2016.
- Fu, G. Q., Xu, W. Y., Yang, R. F., Li, J. B., and Zhao, C. S.: The distribution and trends of fog and haze in the North China Plain over the past 30 years, *Atmos. Chem. Phys.*, 14, 11949-11958, doi:10.5194/acp-14-11949-2014, 2014a.
- Fu, X., Wang, S., Zhao, B., Xing, J., Cheng, Z., Liu, H., and Hao, J.: Emission inventory of primary pollutants and chemical speciation in 2010 for the Yangtze River Delta region, China, *Atmos. Environ.*, 70, 39–50, doi:10.1016/j.atmosenv.2012.12.034, 2013.
- Fu, X., Wang, S. X., Cheng, Z., Xing, J., Zhao, B., Wang, J. D., and Hao, J. M.: Source, transport and impacts of a heavy dust event in the Yangtze River Delta, China, in 2011, *Atmos. Chem. Phys.*, 14, 1239-1254, doi:10.5194/acp-14-1239-2014, 2014b.
- Geng, F., Zhang, Q., Tie, X., Huang, M., Ma, X., Deng, Z., Yu, Q., Quan, J., Zhao, C.: Aircraft measurements of O₃, NO_x, CO, VOCs, and SO₂ in the Yangtze River Delta region. *Atmospheric Environment*, 43(3), 584-593, 2009.
- Hartl, A. and Wenig, M. O.: Regularisation model study for the least-squares retrieval of aerosol extinction time series from UV/VIS MAX-DOAS observations for a ground layer profile parameterisation, *Atmos. Meas. Tech.*, 6, 1959-1980, doi:10.5194/amt-6-1959-2013, 2013.
- Hendrick, F., Müller, J.-F., Clèner, K., Wang, P., De Mazière, M., Fayt, C., Gielen, C., Hermans, C., Ma, J. Z., Pinardi, G., Stavrou, T., Vlemmix, T., and Van Roozendael, M.: Four years of ground-based MAX-DOAS observations of HONO and NO₂ in the Beijing area, *Atmos. Chem. Phys.*, 14, 765-781, doi:10.5194/acp-14-765-2014, 2014.
- Hendrick, F., Gielen, C., Lerot, C., Stavrou, T., De Smedt, I., Fayt, C., Hermans, C., Müller, J. F., Pinardi, G., Volkamer, R., Wang, P., and Van Roozendael, M.: Retrieval of CHOCHO from MAX-DOAS measurements in the Beijing area, 7th DOAS workshop 2015, Brussels, Belgium, 7 July 2015.
- Heney, L. G. and Greenstein J. L.: Diffuse radiation in the galaxy, *Astrophysical Journal*, 93, 70-83, 1941.
- Ho, K. F., Lee, S. C., Louie, P. K. K., and Zou, S. C.: Seasonal variation of carbonyl compound concentrations in urban area of Hong Kong, *Atmos. Environ.*, 36, 1259–1265, 2002.



- Holben, B. N., Eck, T. F., Slutsker, I., Tanre, D., Buis, J. P., Set-zer, A., Vermote, E., Reagan, J. A., Kaufman, Y., Nakajima, T., Lavenue, F., Jankowiak, I., and Smirnov, A.: AERONET – A federated instrument network and data archive for aerosol characterization, *Remote Sens. Environ.*, 66, 1–16, 1998.
- Holben, B. N., Tanre, D., Smirnov, A., Eck, T. F., Slutsker, I., Abuhassan, N., Newcomb, W. W., Schafer, J., Chatenet, B.,
5 Lav-enué, F., Kaufman, Y. J., Van de Castle, J., Setzer, A., Markham, B., Clark, D., Frouin, R., Halthore, R., Karnieli, A., O’Neill, N. T., Pietras, C., Pinker, R. T., Voss, K., and Zibordi, Z.: An emerg-ing ground-based aerosol climatology: Aerosol optical depth from AERONET, *J. Geophys. Res.*, 106, 12067–12097, 2001
- Hönniger, G. and Platt, U.: Observations of BrO and its vertical distribution during surface ozone depletion at Alert, *Atmos. Environ.*, 36, 2481–2489, 2002.
- 10 Hönniger, G., Friedeburg, C. von and Plat, U., Multi axis differential optical absorption spectroscopy (MAX-DOAS), *Atmos. Chem. Phys.*, 4, 231–254, 2004
- Huang, C., Chen, C. H., Li, L., Cheng, Z., Wang, H. L., Huang, H. Y., Streets, D. G., Wang, Y. J., Zhang, G. F., and Chen, Y. R.: Emission inventory of anthropogenic air pollutants and VOC species in the Yangtze River Delta region, China, *Atmos. Chem. Phys.*, 11, 4105–4120, doi:10.5194/acp-11-4105-2011, 2011.
- 15 Huang, R.-J., Zhang, Y., Bozzetti, C., Ho, K.-F., Cao, J., Han, Y., Dällenbach, K. R., Slowik, J. G., Platt, S. M., Canonaco, F., Zotter, P., Wolf, R., Pieber, S. M., Bruns, E. A., Crippa, M., Ciarelli, G., Piazzalunga, A., Schwikowski, M., Abbaszade, G., Schnelle-Kreis, J., Zimmermann, R., An, Z., Szidat, S., Baltensperger, U., Haddad, I. E., and Prévôt, A. S. H.: High secondary aerosol contribution to particulate pollution during haze events in China, *Nature*, 514, 218–222, 2014.
- Irie, H., Kanaya, Y., Akimoto, H., Iwabuchi, H., Shimizu, A., and Aoki, K.: First retrieval of tropospheric aerosol profiles
20 using MAX-DOAS and comparison with lidar and sky radiometer measurements, *Atmos. Chem. Phys.*, 8, 341–350, 2008.
- Irie, H., Takashima, H., Kanaya, Y., Boersma, K. F., Gast, L., Wittrock, F., Brunner, D., Zhou, Y., and Van Roozendael, M.: Eight-component retrievals from ground-based MAX-DOAS observations, *Atmos. Meas. Tech.*, 4, 1027–1044, 2011.
- Jiang, C., Wang, H., Zhao, T., Li, T., and Che, H.: Modeling study of PM_{2.5} pollutant transport across cities in China's Jing–Jin–Ji region during a severe haze episode in December 2013, *Atmos. Chem. Phys.*, 15, 5803–5814, doi:10.5194/acp-15-
25 5803-2015, 2015.
- Junkermann, W.: On the distribution of formaldehyde in the western Po-Valley, Italy, during FORMAT 2002/2003, *Atmos. Chem. Phys.*, 9, 9187–9196, doi:10.5194/acp-9-9187-2009, 2009.
- Kanaya, Y., Irie, H., Takashima, H., Iwabuchi, H., Akimoto, H., Sudo, K., Gu, M., Chong, J., Kim, Y. J., Lee, H., Li, A., Si, F., Xu, J., Xie, P.-H., Liu, W.-Q., Dzhola, A., Postlyakov, O., Ivanov, V., Grechko, E., Terpigova, S., and Panchenko, M.:
30 Long-term MAX-DOAS network observations of NO₂ in Russia and Asia (MADRAS) during the period 2007–2012: instrumentation, elucidation of climatology, and comparisons with OMI satellite observations and global model simulations, *Atmos. Chem. Phys.*, 14, 7909–7927, doi:10.5194/acp-14-7909-2014, 2014.
- Kesselmeier, J. and Staudt, M.: Biogenic volatile organic compounds (VOC): an overview on emission, physiology and ecology. *J. Atmos. Chemistry* 33, 23–88, 1999.



- Kraus, S.: DOASIS, A Framework Design for DOAS, PhD-thesis, University of Mannheim, http://hci.iwr.uni-heidelberg.de/publications/dip/2006/Kraus_PhD2006.pdf, 2006.
- Lee, C., Martin, R. V., van Donkelaar, A., Lee, H., Dicker-son, R. R., Hains, J. C., Krotkov, N., Richter, A., Vinnikov, K., and Schwab, J. J.: SO₂ emissions and lifetimes: Estimates from inverse modeling using in situ and global, space-based
5 (SCIAMACHY and OMI) observations, *J. Geophys. Res.*, 116, D06304, doi:10.1029/2010JD014758, 2011.
- Levelt, P. F., Hilsenrath, E., Leppelmeier, G. W., van den Oord, G. H. J., Bhartia, P. K., Tamminen, J., de Haan, J. F. and Veefkind, J. P.: Science objectives of the Ozone Monitoring Instrument, *IEEE Trans. Geosci. Remote Sens.*, 44, 1199, 2006a.
- Levelt, P. F., van den Oord, G. H. J., Dobber, M. R., Malkki, A., Visser, H., de Vries, J., Stammes, P., Lundell, J. and Saari, H.: The Ozone Monitoring Instrument, *IEEE Trans. Geosci. Remote Sens.*, 44, 1093, 2006b.
- 10 Li X., Brauers, T. and Hofzumahaus, A.: MAX-DOAS measurements of NO₂, HCHO and CHOCHO at a rural site in Southern China. *Atmos. Chem. Phys. Discuss.*, 12, 3983-4029, 2012.
- Li X., Brauers, T., Shao, M., Garland, R. M., Wagner, T., Deutschmann, T., and Wahner, A.: MAX-DOAS measurements in southern China: retrieval of aerosol extinctions and validation using ground-based in-situ data. *Atmos. Chem. Phys.*, 10, 2079–2089, 2010.
- 15 Li, G. L., Zhou, M., Chen, C. H., Wang, H. L., Wang, Q., Lou, S. R., Qiao, L. P., Tang, X. B., Li, L., Huang H. Y., Chen M., H., Huang C., and Zhang, G. F.: Characteristics of particulate matters and its chemical compositions during the dust episodes in Shanghai in spring, 2011, *Environmental Science*, 35(5), 1644-1653, 2014
- Lin, W., Xu, X., Ge, B., and Liu, X.: Gaseous pollutants in Beijing urban area during the heating period 2007–2008: variability, sources, meteorological, and chemical impacts, *Atmos. Chem. Phys.*, 11, 8157–8170, doi:10.5194/acp-11-8157-
20 2011, 2011.
- Liu, F., Beirle, S., Zhang, Q., Dörner, S., He, K. B., and Wagner, T.: NO_x lifetimes and emissions of hotspots in polluted background estimated by satellite observations, *Atmos. Chem. Phys. Discuss.*, 15, 24179-24215, doi:10.5194/acpd-15-24179-2015, 2015.
- Liu, J., Zheng, Y., Li, Z., Flynn, C., and Cribb, M.: Seasonal variations of aerosol optical properties, vertical distribution and
25 associated radiative effects in the Yangtze Delta region of China. *Journal of Geophysical Research: Atmospheres* (1984–2012), 117(D16), 2012.
- Lu, Z., Streets, D. G., Zhang, Q., Wang, S., Carmichael, G. R., Cheng, Y. F., Wei, C., Chin, M., Diehl, T., and Tan, Q.: Sulfur dioxide emissions in China and sulfur trends in East Asia since 2000, *Atmos. Chem. Phys.*, 10, 6311–6331, doi:10.5194/acp-10-6311-2010, 2010.
- 30 Ma, J. Z., Beirle, S., Jin, J. L., Shaiganfar, R., Yan, P., and Wagner, T.: Tropospheric NO₂ vertical column densities over Beijing: results of the first three years of ground-based MAX-DOAS measurements (2008–2011) and satellite validation, *Atmos. Chem. Phys.*, 13, 1547-1567, doi:10.5194/acp-13-1547-2013, 2013.
- Meller, R. and Moortgat, G. K.: Temperature dependence of the absorption cross sections of formaldehyde between 223 and 323 K in the wavelength range 225–375 nm, *J. Geophys. Res.*, 105, 7089–7101, 2000



- Meng, Z. Y., Ding, G. A., Xu, X. B., Xu, X. D., Yu, H. Q., and Wang, S. F.: Vertical distributions of SO₂ and NO₂ in the lower atmosphere in Beijing urban areas, China. *Science of the Total Environment*, 390(2), 456-465, 2008.
- Nasse, J. M., Zielcke, J., Frieß U., Lampel, J., König-Langlo, G. and Platt, U.: Inference of cloud altitude and optical properties from MAX-DOAS measurements, EGU General Assembly 2015, Wien, 12 April 2015 - 17 April 2015, 5 hdl:10013/epic.45412, <http://hdl.handle.net/10013/epic.45412>.
- Oppenheimer, C., Francis, P., and Stix, J.: Depletion rates of sulfur dioxide in tropospheric volcanic plumes, *Geophys. Res. Lett.*, 25, 2671–2674, doi:10.1029/98GL01988, 1998.
- Pinardi, G., Van Roozendaal, M., Abuhassan, N., Adams, C., Cede, A., Cléner, K., Fayt, C., Frieß U., Gil, M., Herman, J., Hermans, C., Hendrick, F., Irie, H., Merlaud, A., Navarro Comas, M., Peters, E., PETERS, A. J. M., Puentedura, O., Richter, A., 10 Schönhardt, A., Shaiganfar, R., Spinei, E., Strong, K., Takashima, H., Vrekoussis, M., Wagner, T., Wittrock, F., and Yilmaz, S.: MAX-DOAS formaldehyde slant column measurements during CINDI: intercomparison and analysis improvement, *Atmos. Meas. Tech.*, 6, 167-185, doi:10.5194/amt-6-167-2013, 2013.
- Platt, U. and Stutz, J.: *Differential Optical Absorption Spectroscopy*. Springer-Verlag Heidelberg, Berlin, 229-375, 2008.
- Qi, H., Lin, W., Xu, X., Yu, X., and Ma, Q.: Significant downward trend of SO₂ observed from 2005 to 2010 at a 15 background station in the Yangtze Delta region, China. *Science China Chemistry*, 55(7), 1451-1458, 2012.
- Qin, M., Xie, P. H., Liu, W. Q., Li, A., Dou, K., Fang, W., Liu, J. G. Zhang, W. J.: Observation of atmospheric nitrous acid with DOAS in Beijing, China, *Journal of Environmental Sciences*, 18, 69-75, 2006.
- Richter, A., Burrows, J. P., Nüß H., Granier, C., and Niemeier, U.: Increase in tropospheric nitrogen dioxide over China observed from space. *Nature*, 437(7055), 129-132, 2005
- 20 Rodgers, C. D.: *Inverse methods for atmospheric sounding, theory and practice*, Series on Atmospheric, Oceanic and Planetary Physics, World Scientific, 2000.
- Roscoe, H. K., Van Roozendaal, M., Fayt, C., du Piesanie, A., Abuhassan, N., Adams, C., Akrami, M., Cede, A., Chong, J., Cléner, K., Friess, U., Gil Ojeda, M., Goutail, F., Graves, R., Griesfeller, A., Grossmann, K., Hemerijckx, G., Hendrick, F., Herman, J., Hermans, C., Irie, H., Johnston, P. V., Kanaya, Y., Kreher, K., Leigh, R., Merlaud, A., Mount, G. H., Navarro, 25 M., Oetjen, H., Pazmino, A., Perez-Camacho, M., Peters, E., Pinardi, G., Puentedura, O., Richter, A., Schönhardt, A., Shaiganfar, R., Spinei, E., Strong, K., Takashima, H., Vlemmix, T., Vrekoussis, M., Wagner, T., Wittrock, F., Yela, M., Yilmaz, S., Boersma, F., Hains, J., Kroon, M., PETERS, A., and Kim, Y. J.: Intercomparison of slant column measurements of NO₂ and O₄ by MAX-DOAS and zenith-sky UV and visible spectrometers, *Atmos. Meas. Tech.*, 3, 1629-1646, doi:10.5194/amt-3-1629-2010, 2010.
- 30 Rozanov, A., Rozanov, V., Buchwitz, M., Kokhanovsky, A., and Burrows, J.: SCIATRAN 2.0 - A new radiative transfer model for geophysical applications in the 175-2400 nm spectral region, in: *Atmospheric Remote Sensing: Earth's Surface, Troposphere, Stratosphere and Mesosphere - I*, edited by Burrows, J. and Eichmann, K., vol. 36 of *ADVANCES IN SPACE RESEARCH*, 1015-1019, 2005.



- Schaub, D., Brunner, D., Boersma, K. F., Keller, J., Folini, D., Buchmann, B., Berresheim, H., and Staehelin, J.: SCIAMACHY tropospheric NO₂ over Switzerland: estimates of NO_x lifetimes and impact of the complex Alpine topography on the retrieval, *Atmos. Chem. Phys.*, 7, 5971-5987, doi: 10.5194/acp-7-5971-2007, 2007.
- Seinfeld, J. H. and Pandis, S. N.: *Atmospheric Chemistry and Physics—From Air Pollution to Climate Change*. John Wiley, New York, 1998.
- Shaiganfar, R., Beirle, S., Sharma, M., Chauhan, A., Singh, R. P., and Wagner, T.: Estimation of NO_x emissions from Delhi using Car MAX-DOAS observations and comparison with OMI satellite data, *Atmos. Chem. Phys.*, 11, 10871-10887, doi:10.5194/acp-11-10871-2011, 2011.
- Sinreich, R., Merten, A., Molina, L., and Volkamer, R.: Parameterizing radiative transfer to convert MAX-DOAS dSCDs into near-surface box averaged mixing ratios and vertical profiles, *Atmos. Meas. Tech.*, 6, 1521-1532, 2013.
- Smirnov, A., Holben, B. N., Eck, T. F., Dubovik, O. and Slutsker, I.: Cloud-Screening and Quality Control Algorithms for the AERONET Database, *Remote Sensing of Environment*, 73, 337, 2000.
- Stavrakou, T., Müller, J.-F., Boersma, K. F., van der A, R. J., Kurokawa, J., Ohara, T., and Zhang, Q.: Key chemical NO_x sink uncertainties and how they influence top-down emissions of nitrogen oxides, *Atmos. Chem. Phys.*, 13, 9057–9082, doi:10.5194/acp-13-9057-2013, 2013.
- Theys, N., De Smedt, I., Gent, J., Danckaert, T., Wang, T., Hendrick, F., Stavrakou, T., Bauduin, S., Clarisse, L., Li, C., Krotkov, N., Yu, H., Brenot, H., and Van Roozendael, M.: Sulfur dioxide vertical column DOAS retrievals from the Ozone Monitoring Instrument: Global observations and comparison to ground - based and satellite data. *Journal of Geophysical Research: Atmospheres*, 120(6), 2470-2491, 2015.
- Vandaele, A. C., Hermans, C., Simon, P. C., Carleer, M., Colin, R., Fally, S., Mérienne, M.-F., Jenouvrier, A., and Coquart, B.: Measurements of the NO₂ absorption cross section from 42000 cm⁻¹ to 10000 cm⁻¹ (238–1000 nm) at 220 K and 294 K, *J. Quant. Spectrosc. Ra.*, 59, 171–184, 1998.
- Van Roozendael, M., Fayt, C., Post, P., Hermans, C., Lambert, J.-C.: Retrieval of BrO and NO₂ from UV-Visible Observations, in: *Sounding the troposphere from space: a new Era for Atmospheric Chemistry. The TROPOSAT Final Report*. Peter Borrell, Patricia M. Borrell, John P. Burrows and Ulrich Platt (editors), Springer Verlag, 155-166, 2003
- Veefkind, J. P., Boersma, K. F., Wang, J., Kurosu, T. P., Krotkov, N., Chance, K., and Levelt, P. F.: Global satellite analysis of the relation between aerosols and short-lived trace gases, *Atmos. Chem. Phys.*, 11, 1255–1267, doi:10.5194/acp-11-1255-2011, 2011.
- Vlemmix, T., Eskes, H. J., Piters, A. J. M., Schaap, M., Sauter, F. J., Kelder, H., and Levelt, P. F.: MAX-DOAS tropospheric nitrogen dioxide column measurements compared with the Lotos-Euros air quality model, *Atmos. Chem. Phys.*, 15, 1313-1330, doi:10.5194/acp-15-1313-2015, 2015a.
- Vlemmix, T., Hendrick, F., Pinardi, G., De Smedt, I., Fayt, C., Hermans, C., Piters, A., Wang, P., Levelt, P., and Van Roozendael, M.: MAX-DOAS observations of aerosols, formaldehyde and nitrogen dioxide in the Beijing area: comparison of two profile retrieval approaches, *Atmos. Meas. Tech.*, 8, 941-963, doi:10.5194/amt-8-941-2015, 2015b.



- Vlemmix, T., PETERS, A. J. M., BERKHOUT, A. J. C., GAST, L. F. L., WANG, P., and LEVELT, P. F.: Ability of the MAX-DOAS method to derive profile information for NO₂: can the boundary layer and free troposphere be separated?, *Atmos. Meas. Tech.*, 4, 2659–2684, 2011
- Vlemmix, T., PETERS, A. J. M., STAMMES, P., WANG, P., and LEVELT, P. F.: Retrieval of tropospheric NO₂ using the MAX-DOAS method combined with relative intensity measurements for aerosol correction, *Atmos. Meas. Tech.*, 3, 1287–1305, 2010.
- Von Glasow, R., Bobrowski, N., and Kern, C.: The effects of volcanic eruptions on atmospheric chemistry, *Chem. Geol.*, 263, 131–142, doi:10.1016/j.chemgeo.2008.08.020, 2009.
- Wagner, T., Erie, F., Marquard, L., Otten, C., Pfeilsticker, K., Senne, T., Stutz, J. and Platt, U.: Cloudy sky optical paths as derived from differential optical absorption spectroscopy observations, *J. Geophys. Res.*, 103, 25307, 1998.
- Wagner, T., Friedeburg, C. von, Wenig M., Otten, C. and Platt, U.: UV/vis observations of atmospheric O₄ absorptions using direct moon light and zenith scattered sunlight under clear and cloudy sky conditions, *J. Geophys. Res.*, 107, D204424, 2002.
- Wagner, T., B. Dix, C. von Friedeburg, Frieß U., Sanghavi, S., Sinreich, R. and Platt, U.: MAX-DOAS O₄ measurements: A new technique to derive information on atmospheric aerosols—Principles and information content, *J. Geophys. Res.*, 109, D22205, 2004.
- Wagner, T., Beirle, S., and Deutschmann, T.: Three-dimensional simulation of the Ring effect in observations of scattered sun light using Monte Carlo radiative transfer models, *Atmos. Meas. Tech.*, 2, 113-124, 2009.
- Wagner, T., Beirle, S., Brauers, T., Deutschmann, T., Frieß U., Hak, C., Halla, J. D., Heue, K. P., Junkermann, W., Li, X., Platt, U. and Pundt-Gruber, I.: Inversion of tropospheric profiles of aerosol extinction and HCHO and NO₂ mixing ratios from MAX-DOAS observations in Milano during the summer of 2003 and comparison with independent data sets, *Atmos. Meas. Tech. Discuss.*, 4, 3891–3964, 2011.
- Wagner, T., Beirle, S., Dörner, S., Friess, U., Remmers, J. and Shaiganfar, R.: Cloud detection and classification based on MAX-DOAS observations, *Atmos. Meas. Tech.*, 7, 1289-1320, 2014
- Wang, T., Nie, W., Gao, J., Xue, L. K., Gao, X. M., Wang, X. F., Qiu, J., Poon, C. N., Meinardi, S., Blake, D., Wang, S. L., Ding, A. J., Chai, F. H., Zhang, Q. Z., and Wang, W. X.: Air quality during the 2008 Beijing Olympics: secondary pollutants and regional impact, *Atmos. Chem. Phys.*, 10, 7603-7615, doi:10.5194/acp-10-7603-2010, 2010.
- Wang, T., Hendrick, F., Wang, P., Tang, G., Clémer, K., Yu, H., Fayt, C., Hermans, C., Gielen, C., Müller, J.-F., Pinardi, G., Theys, N., Brenot, H., and Van Roozendaal, M.: Evaluation of tropospheric SO₂ retrieved from MAX-DOAS measurements in Xianghe, China, *Atmos. Chem. Phys.*, 14, 11149-11164, doi:10.5194/acp-14-11149-2014, 2014a.
- Wang, Y., Li, A., Xie, P. H., Chen, H., Xu, J., Wu, F. C., G., L. J., and Q., L. W.: Retrieving vertical profile of aerosol extinction by multi-axis differential optical absorption spectroscopy, *Acta Phys. Sin.*, 16, doi: 10.7498/aps.62.180705, <http://wulixb.iphys.ac.cn/EN/abstract/abstract54703.shtml#>, 2013a.



- Wang, Y., Li, A., Xie, P. H., Chen, H., Mou, F. S., Xu, J., Wu, F. C., Zeng, Y., Liu, J. G. and Liu, W. Q.: Measuring tropospheric vertical distribution and vertical column density of NO₂ by multi-axis differential optical absorption spectroscopy, *Acta Phys. Sin.*, 16, DOI:10.7498/aps.62.200705, <http://wulixb.iphy.ac.cn/EN/abstract/abstract56201.shtml>, 2013b.
- 5 Wang, Y., Li, A., Xie, P. H., Wagner, T., Chen, H., Liu, W. Q., and Liu, J. G.: A rapid method to derive horizontal distributions of trace gases and aerosols near the surface using multi-axis differential optical absorption spectroscopy, *Atmos. Meas. Tech.*, 7, 1663-1680, doi:10.5194/amt-7-1663-2014, 2014b.
- Wang, Y., Penning de Vries, M., Xie, P. H., Beirle, S., Dörner, S., Remmers, J., Li, A., and Wagner, T.: Cloud and aerosol classification for 2.5 years of MAX-DOAS observations in Wuxi (China) and comparison to independent data sets, *Atmos. Meas. Tech.*, 8, 5133-5156, doi:10.5194/amt-8-5133-2015, 2015.
- 10 Winterrath, T., Koruso, T. P., Richter, A. and Burrows, J. P.: Enhanced O₃ and NO₂ in thunderstorm clouds: convection or production, *Geophys. Res. Lett.*, 26, 1291, 1999.
- Wittrock, F., Oetjen, H., Richter, A., Fietkau, S., Medeke, T., Rozanov, A., and Burrows, J. P.: MAX-DOAS measurements of atmospheric trace gases in Ny-Alesund – Radiative transfer studies and their application, *Atmos. Chem. Phys.*, 4, 955–966, 15 2004.
- Wittrock, F.: The Retrieval of Oxygenated Volatile Organic Compounds by Remote Sensing Techniques. Ph.D., University of Bremen, Bremen, Germany, 2006, Available at: http://www.doas-bremen.de/paper/diss_wittrock_06.pdf (last accessed December 2015).
- Xie, X., Shao, M., Liu, Y., Lu, S., Chang, C. C., and Chen, Z. M.: Estimate of initial isoprene contribution to ozone formation potential in Beijing, China. *Atmospheric Environment*, 42(24), 6000-6010, 2008.
- 20 Xue, L., Ding, A., Gao, J., Wang, T., Wang, W., Wang, X., Lei, H., Jin, D., and Qi, Y.: Aircraft measurements of the vertical distribution of sulfur dioxide and aerosol scattering coefficient in China. *Atmospheric Environment*, 44(2), 278-282, 2010.
- Yilmaz, S.: Retrieval of Atmospheric Aerosol and Trace Gas Vertical Profiles using Multi-Axis Differential Optical Absorption Spectroscopy, Dissertation submitted to the Combined Faculties for the Natural Sciences and for Mathematics of the Ruperto-Carola University of Heidelberg, Germany for the degree of Doctor of Natural Sciences, 2012.
- 25 Thalman, R. M. and Volkamer, R.: Temperature Dependent Absorption Cross-Sections of O₂-O₂ collision pairs between 340 and 630 nm and at atmospherically relevant pressure, *Phys. Chem. Chem. Phys.*, 15, 15371–15381, doi:10.1039/c3cp50968k, 2013



Tables

Table 1 Setting used for the O₄, NO₂, SO₂ and HCHO DOAS analyses

Parameter	Data source	Fitting interval			
		O ₄	NO ₂	SO ₂	HCHO
Wavelength range		351-390nm	351-390nm	307.8-330nm	324.6-359nm
NO ₂	Vandaele et al. (1998), 220 K, 294 K	×	×	× (only 294 K)	× (only 294 K), I ₀ -corrected* (10 ¹⁷ molecules/cm ²)
O ₃	Bogumil et al., (2003), 223 K and 243 K	×(only 223 K)	×(only 223 K)	×	×(only 223 K) I ₀ -corrected* (10 ¹⁸ molecules/cm ²)
O ₄	Thalman and Volkamer (2013), 293 K	×	×	×	×
SO ₂	Bogumil et al. (2003), 293 K			×	×
HCHO	Meller and Moortgat (2000), 293 K	×	×	×	×
Ring	Two Ring spectra calculated with DOASIS (Kraus, 2006; Wagner et al., 2009)	×	×	×	×
Polynomial degree		3	3	5	5
Intensity offset		constant	constant	constant	constant

* solar I₀ correction, Aliwell et al., 2002



Table 2 Different filters and corresponding thresholds applied to the retrieved SCDs. Also the corresponding fractions of screened data are shown. (SZA: solar zenith angle; RIO: relative intensity offset; RMS: root mean square of the spectral residual)

O ₄ and NO ₂		SO ₂		HCHO	
filter	percentage	filter	percentage	filter	percentage
SZA < 75°	6.2%	SZA < 75°	5.8%	SZA < 75°	6.1%
RIO < 0.01	5.6%	RIO < 0.01	1.1%	RIO < 0.01	7.1%
RMS < 0.003	0.3%	RMS < 0.01	0.2%	RMS < 0.003	0.2%

- 5 Table 3 Filter scheme of aerosol and trace gas results derived from MAX-DOAS observations. Filled circles (●): use of measurement is recommended; Open circles (○): use of measurement is not recommended.

	AOD	Aerosol extinction near surface	Profile of aerosol extinction	VCD	VMR near surface	Profile of VMRs
Low aerosols	●	●	●	●	●	●
High aerosols	●	●	●	●	●	●
Cloud holes	○	●	○	●	●	●
Broken clouds	○	●	○	●	●	●
Continuous clouds	○	●	○	●	●	●
fog	○	○	○	○	○	○
Thick clouds	○	○	○	○	○	○



Table 4 Averaged error budget (in %) of the retrieved TG VCDs and AOD, and near-surface (0–200 m) TG VMRs and AE. The total uncertainty is calculated by adding the different error terms in Gaussian error propagation.

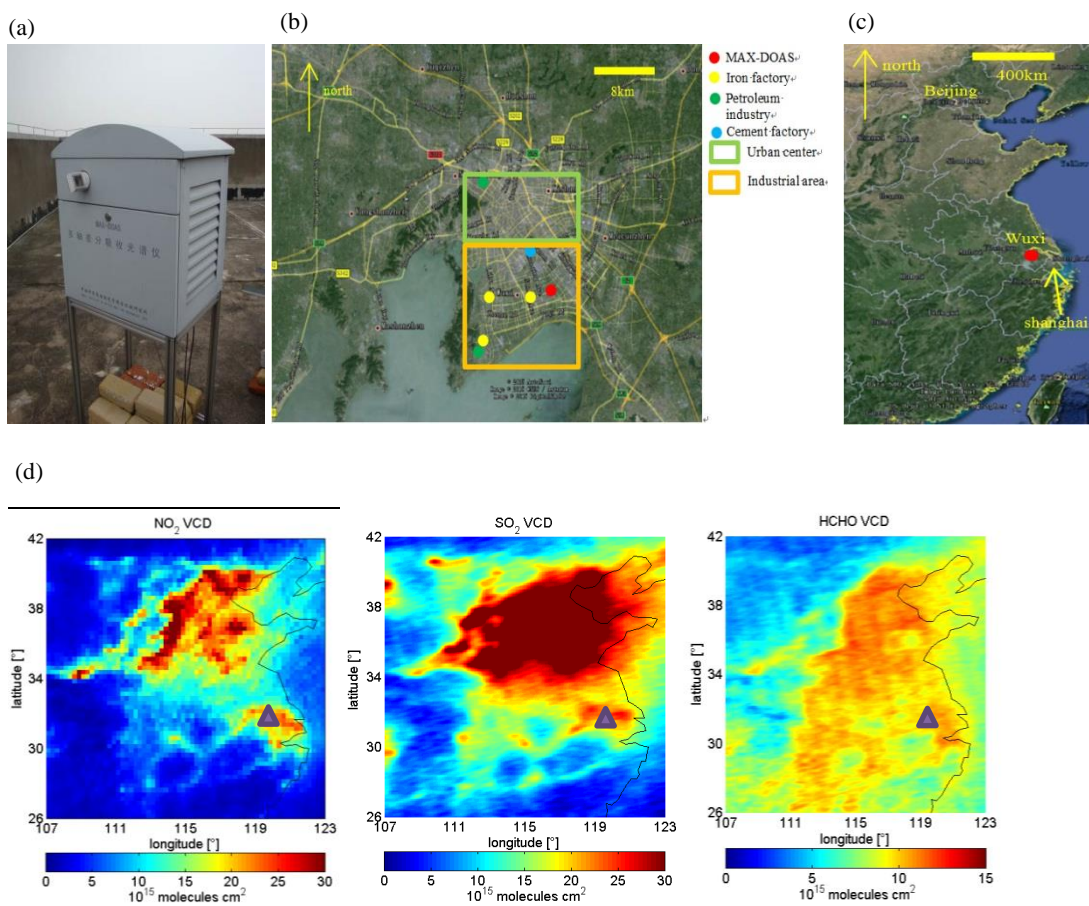
	0-200 m				VCD or AOD			
	AE	NO ₂	SO ₂	HCHO	AOD	NO ₂	SO ₂	HCHO
Smoothing and noise error	10	12	19	50	6	17	25	50
Algorithm error	4	3	4	4	8	11	10	11
Cross section error	5	3	5	9	5	3	5	9
Related to temperature dependence of cross section	10	2	3	6	10	2	3	6
Related to the aerosol retrieval (only for trace gases)	-	16	16	16	-	15	15	15
Total	16	21	26	54	15	25	31	54

Table 5 Correlation coefficients between hourly averaged trace gas VCDs and AODs (for clear sky conditions) as well as between VMRs and aerosol extinction near the surface (for clear and cloudy conditions except thick clouds and fog). The numbers of the data point use for the analysis are given for each season.

	winter		spring		summer		autumn	
	column	surface	column	surface	column	surface	column	surface
Number of observations	375	525	1339	1739	1308	1830	1142	1676
NO ₂	0.51	0.69	0.37	0.58	0.48	0.63	0.44	0.65
SO ₂	0.52	0.69	0.45	0.62	0.45	0.62	0.44	0.66
HCHO	0.77	0.81	0.51	0.62	0.35	0.62	0.57	0.69

10

15



5
10
Figure 1: The MAX-DOAS instrument (a) (also the long path DOAS and the visibility meter) is operated at the location marked by the red dot in subfigure (b) in Wuxi city (c). In subfigure (b), the dots with different colours indicate the positions of different types of emission sources; the green and orange blocks indicate the urban centre and industrial area, respectively. The mean maps of tropospheric VCDs of NO₂ (from DOMINO version 2), SO₂ (from BIRA, Theys et al., 2015) and HCHO (from BIRA, I. De Smedt et al., 2015) derived from OMI observations over eastern China in the period from 2011 to 2014 are shown in subfigure (d), in which the triangle flag indicates the location of Wuxi.

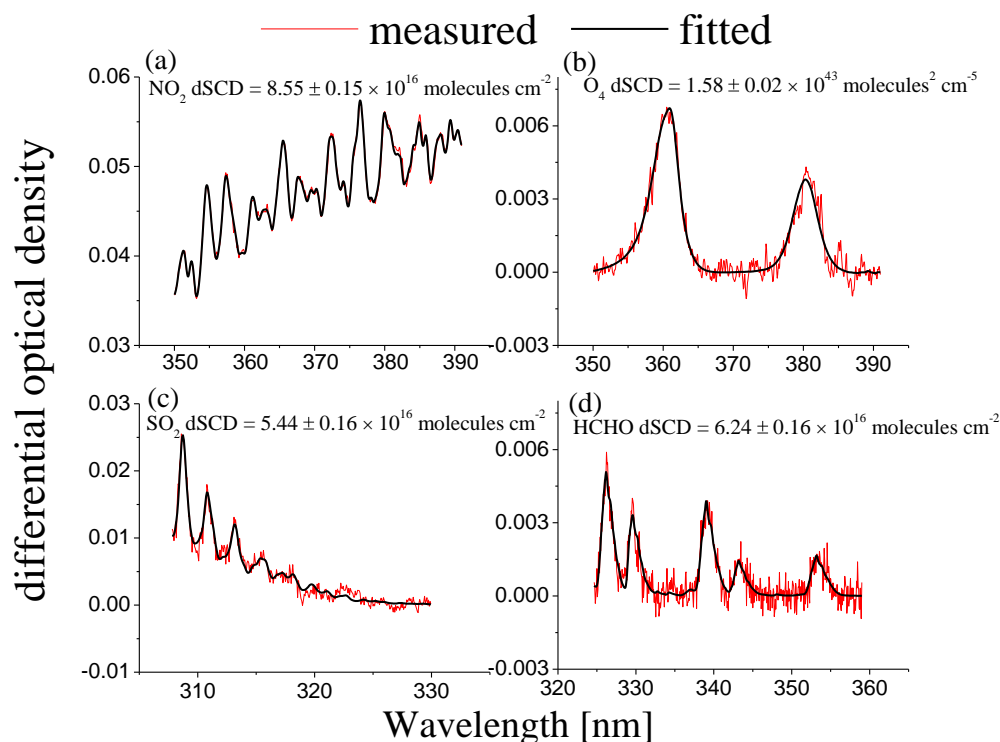
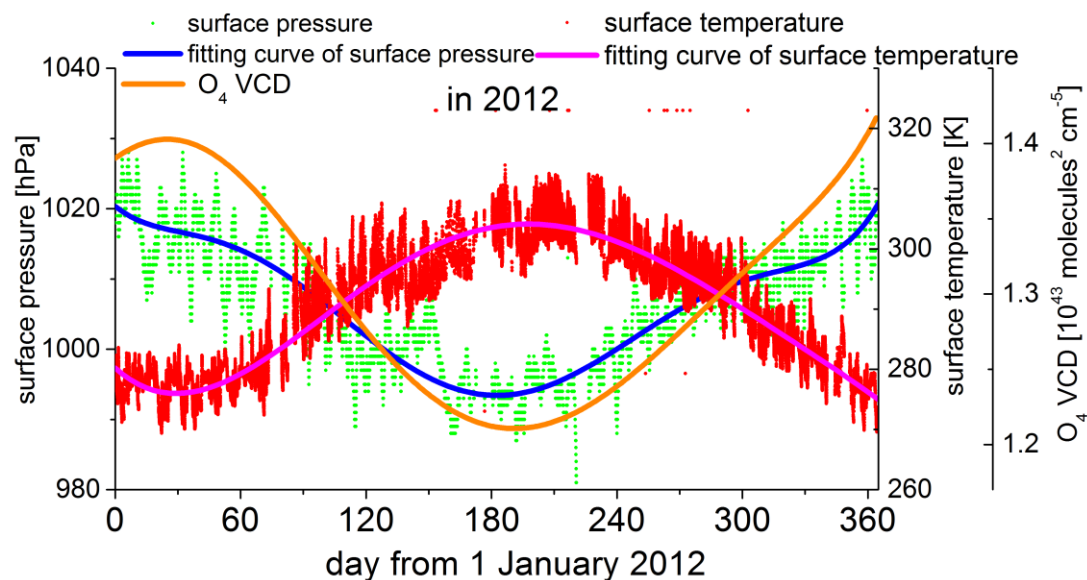
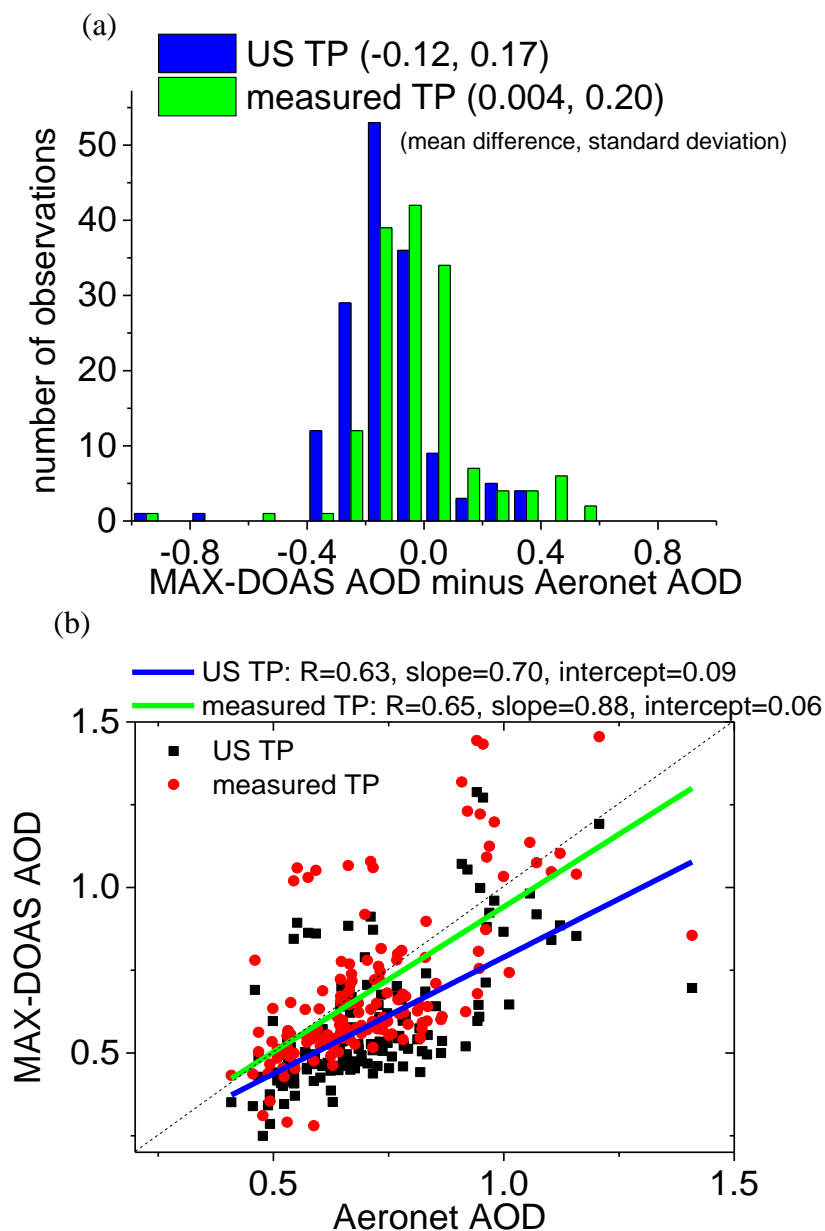


Figure 2: Examples of typical DOAS fits of NO_2 (a), O_4 (b) and SO_2 (c) at 11:37 on 1 December 2011 as well as HCHO at 11:34 on 12 July 2012. The fitted dSCDs of NO_2 , O_4 , SO_2 and HCHO are given in the corresponding subfigures. The black and red curves indicate the fitted absorption structures and the derived absorption structures from the measured spectra, respectively.

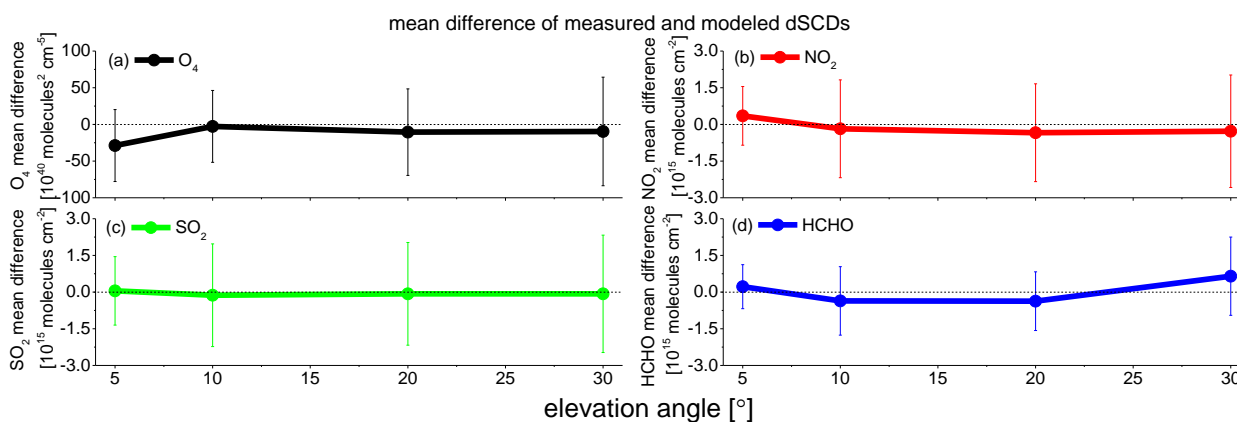


5

Figure 3: Annual variation of surface temperature, surface pressure as well as fitted 6th order polynomials in 2012. Also the O_4 VCDs calculated based on the fitted curves of the measured annual variations of surface temperature and pressure in 2012 is shown (similar results are found for other years).



5 **Figure 4: Dependence of retrieved AOD on temperature and pressure (TP) for clear sky conditions. (a): Frequency distribution of**
the differences of the AODs derived from MAX-DOAS and AERONET for January 2012. The MAX-DOAS results from the
retrieval using either the US standard summer TP profiles or the explicit TP from local measurements are indicated by blue and
green colours, respectively. The mean difference and standard deviation are shown in brackets. (b): The AODs retrieved from
MAX-DOAS observations (using either the US standard summer TP profile or the explicit TP from measurements) are plotted
 10 **against those from the Taihu AERONET station. The results of the linear regression are shown on top of the diagram.**



5 **Figure 5:** Mean differences and the standard deviations (error bars) between the measured and modelled dSCDs of O₄ (a), NO₂ (b), SO₂ (c) and HCHO (d) for clear sky conditions with low aerosols plotted against the elevation angles of MAX-DOAS measurements.

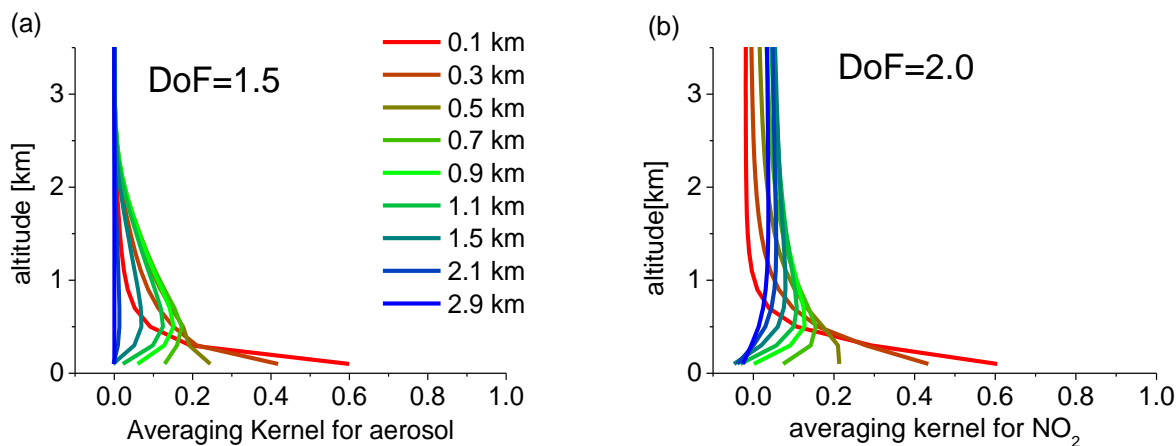
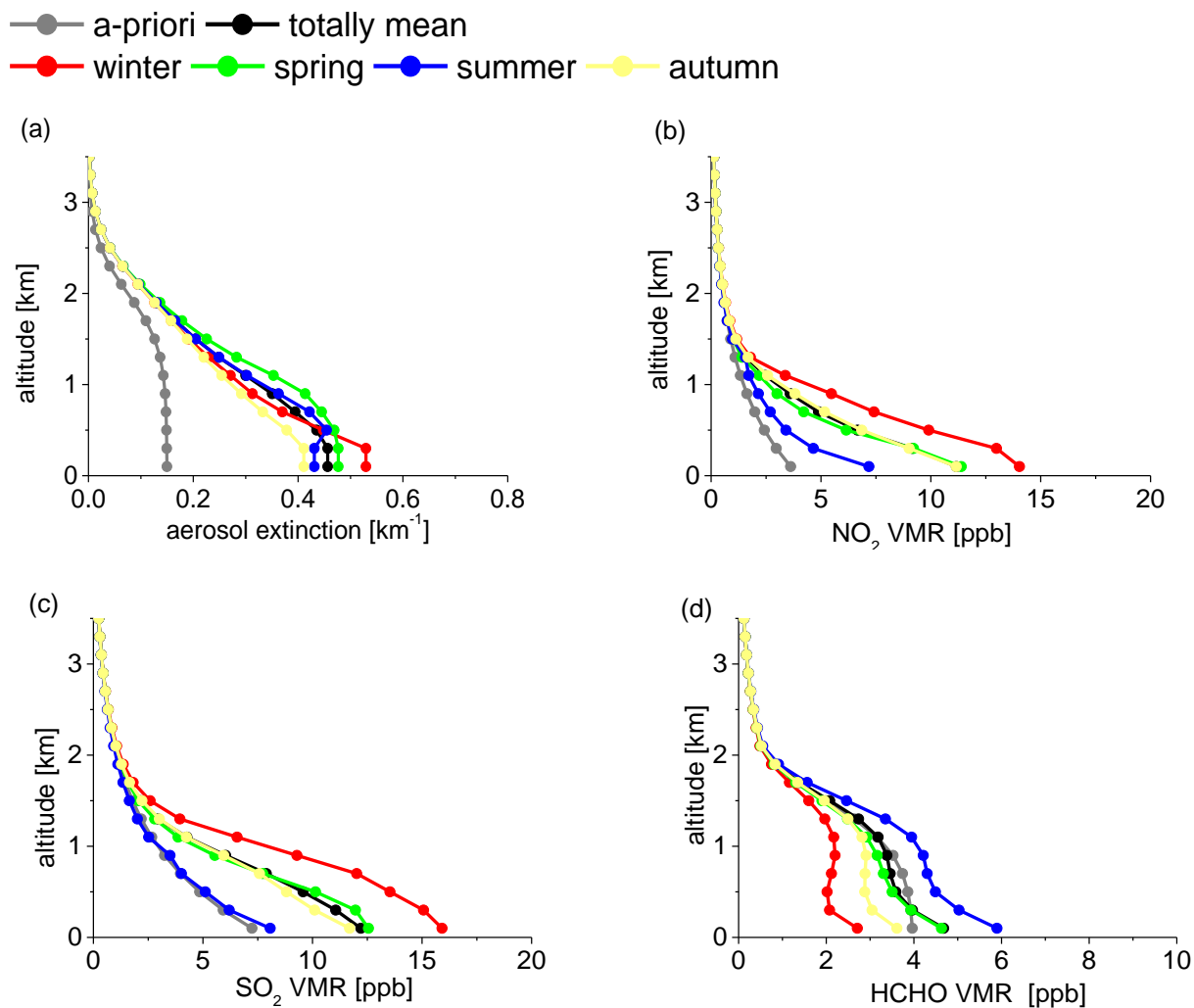


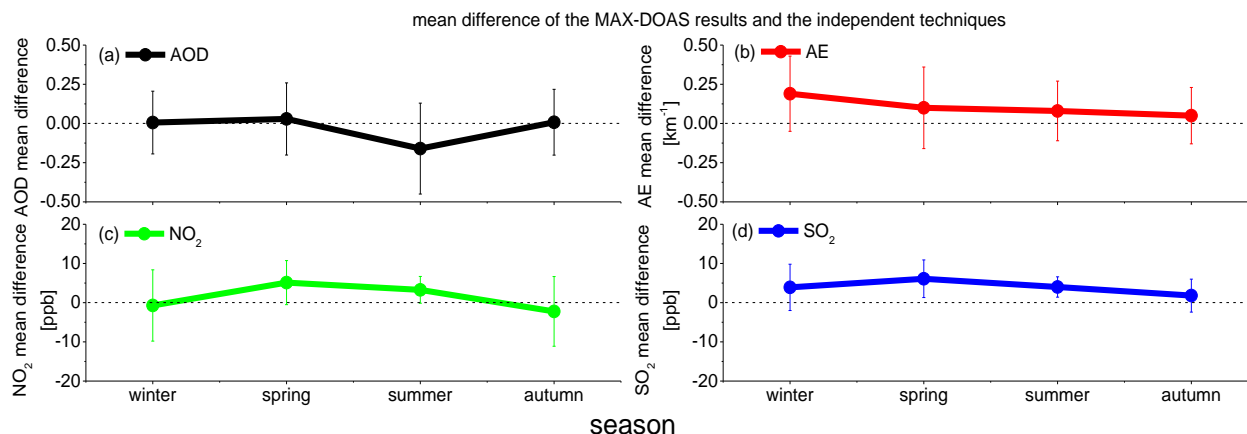
Figure 6: Averaged averaging kernels of aerosol (a) and NO₂ (b) retrievals for all the MAX-DOAS measurements for clear sky conditions with low aerosols. DoF is the degree of freedom related to the averaging kernel.

10

15



5 **Figure 7:** The averaged profiles retrieved from the measurements in the whole period and in different season for clear sky conditions with low aerosols: (a) aerosol extinction, (b) NO₂ VMR, (c) SO₂ VMR and (d) HCHO VMR. Also shown are the respective a-priori profiles.



5 **Figure 8:** Seasonally mean differences and standard deviations (shown as the error bar) between MAX-DOAS results and independent techniques for different seasons for clear sky conditions with low aerosols. Different colours denote AOD (a) (compared with the Taihu AERONET level 1.5 data sets), AE (b) (compared with the nearby visibility meter) and NO₂ (c) and SO₂ (d) (compared with the nearby long path DOAS instrument).

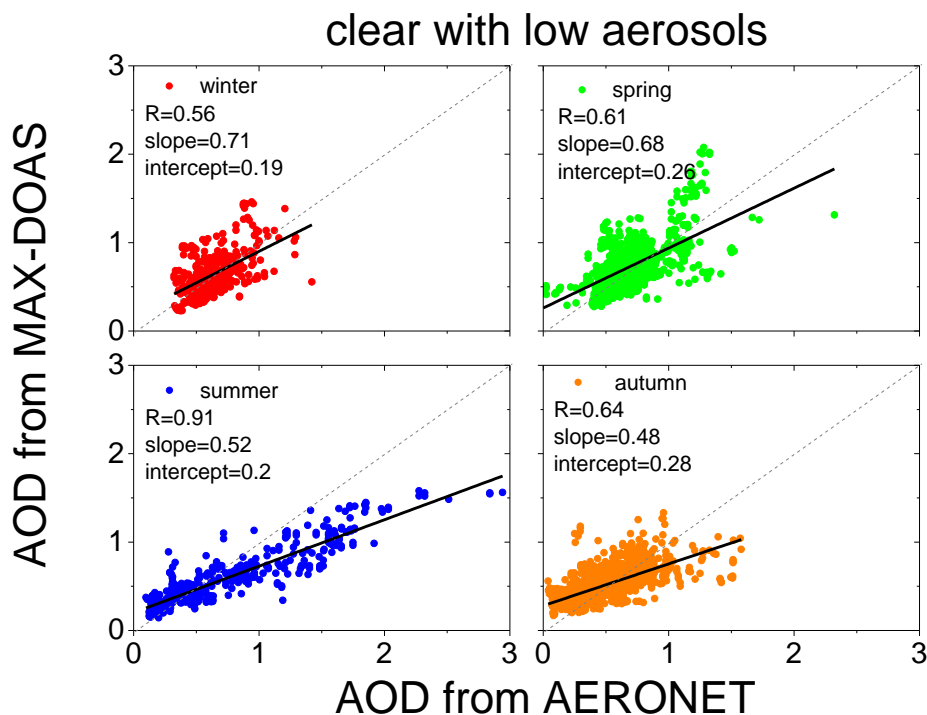


Figure 9: Scatter plots of the AODs derived from MAX-DOAS versus those from the Taihu AERONET station (level 1.5) in different seasons for clear sky conditions with low aerosols. Results of the linear regression are shown in the individual subfigures.

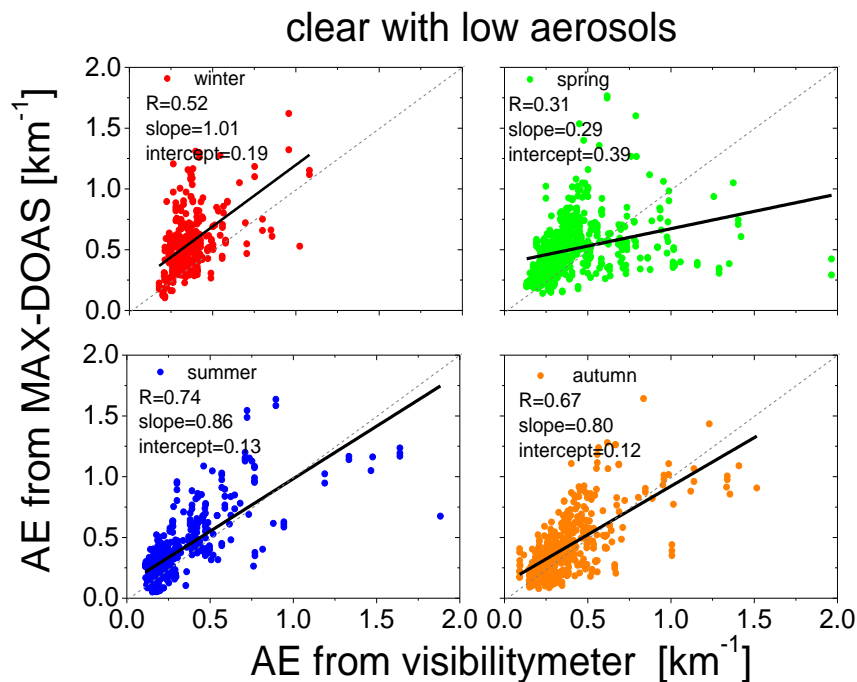
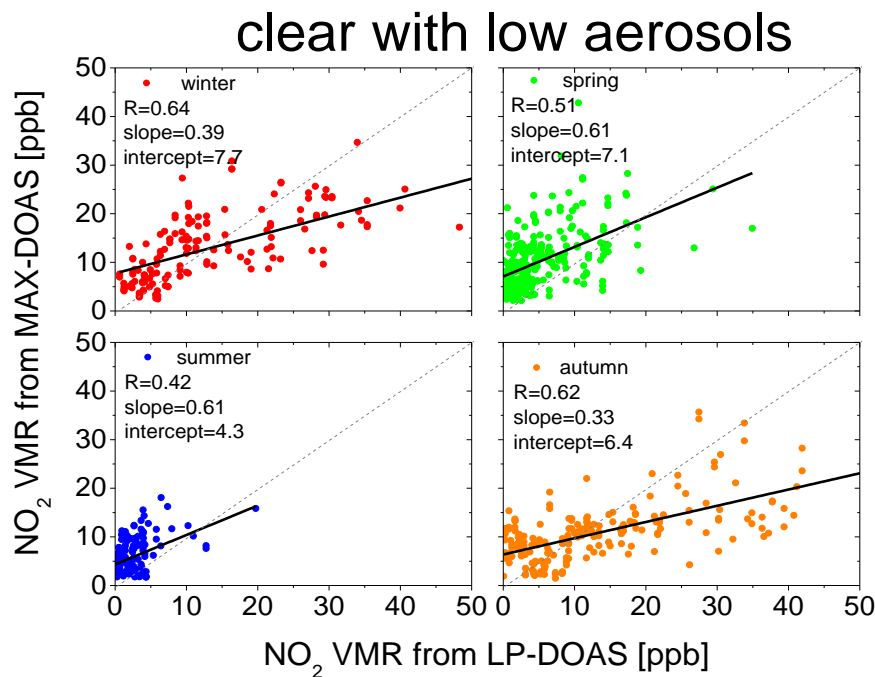


Figure 10: Same as Fig. 9 but for the comparison of the near surface aerosol extinction derived from MAX-DOAS and the visibility meter



5 Figure 11: Same as Fig. 9 but for comparison of the near surface NO_2 mixing ratios derived from MAX-DOAS and LP-DOAS.

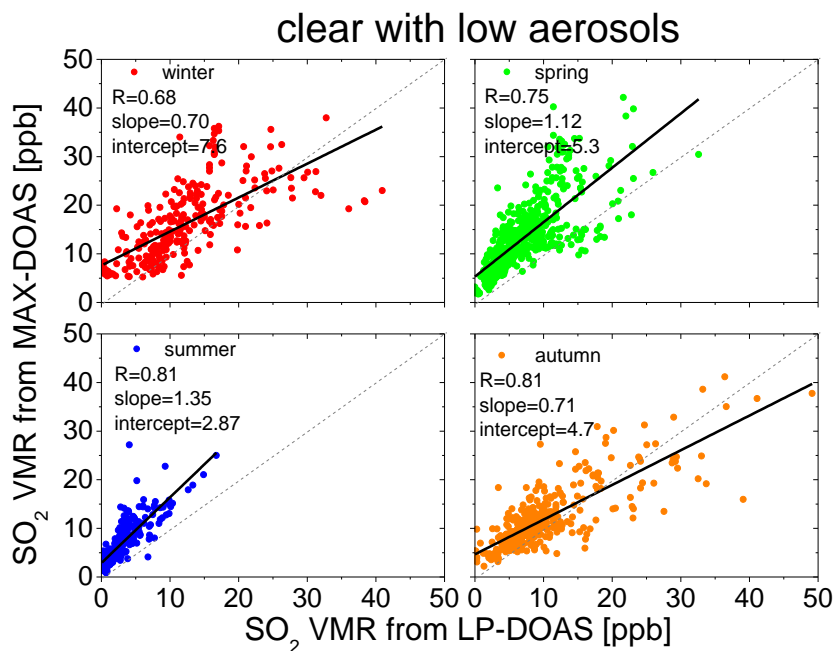
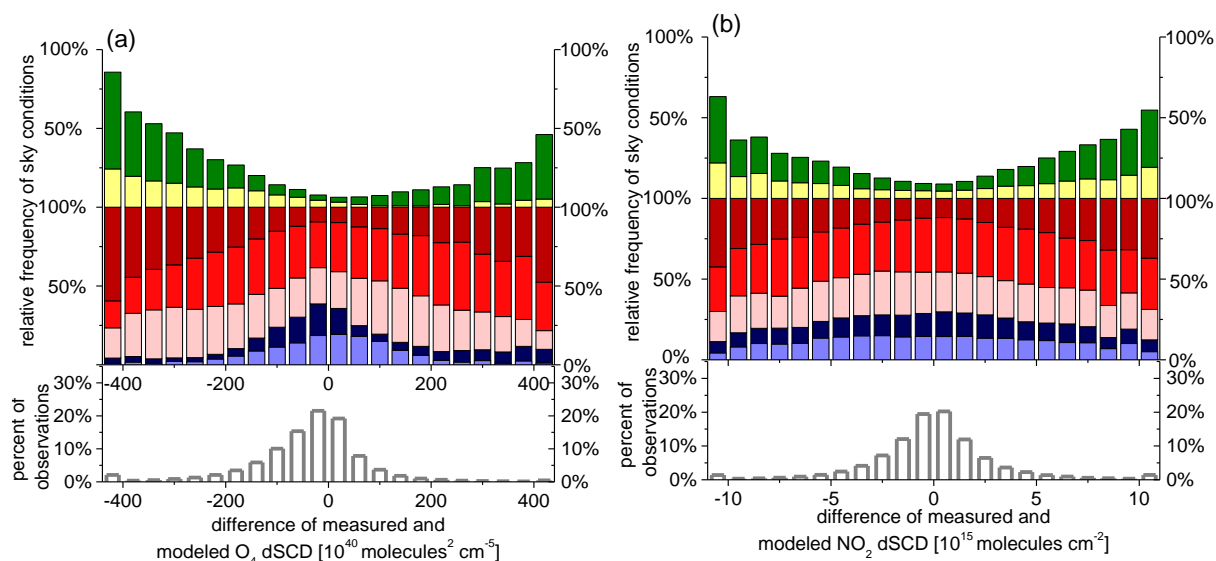


Figure 12: Same as Fig. 9 but for comparison of the near surface SO₂ mixing ratios derived from MAX-DOAS and LP-DOAS.



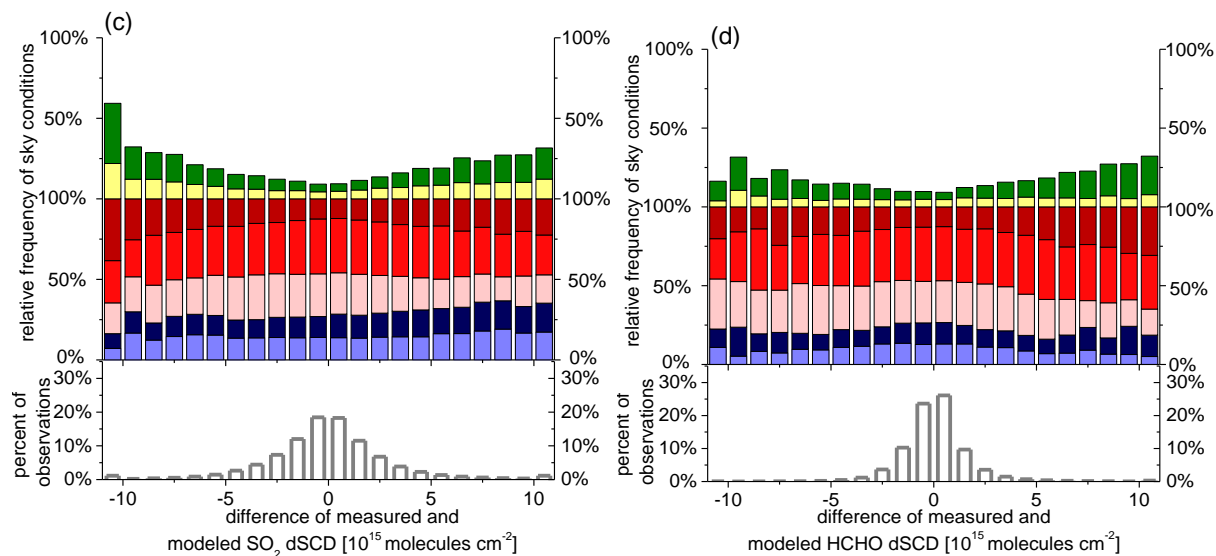
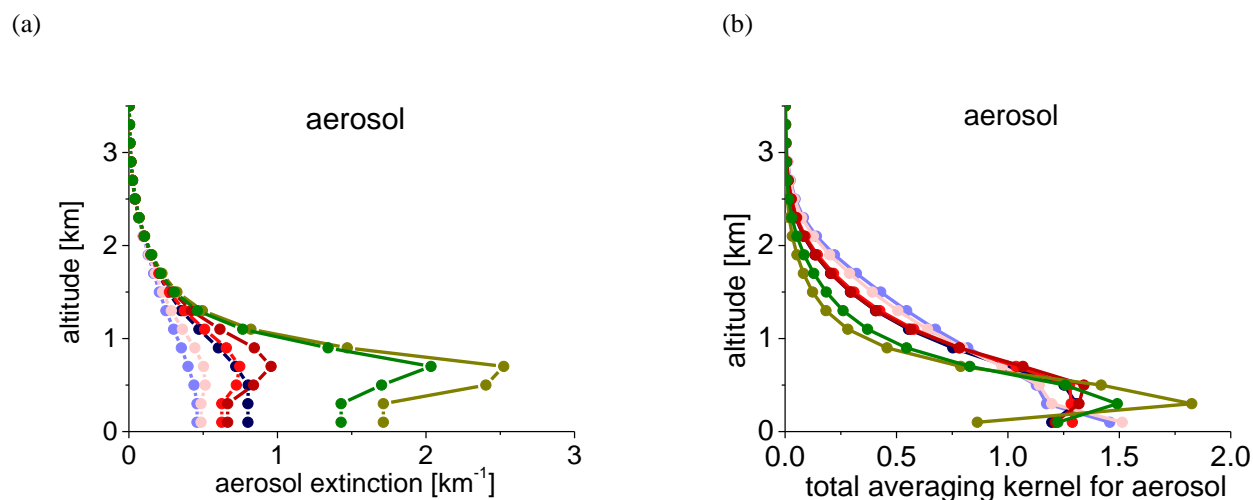


Figure 13: Histograms of the differences between the measured and modelled dSCDs of O₄ (a), NO₂ (b), SO₂ (c) and HCHO (d) for all elevation angles. The colour bars show the relative frequencies of the different sky conditions for each bin (top). The grey hollow bars (bottom) represent the relative frequencies of the number of measurements compared to the total number of observations.

5

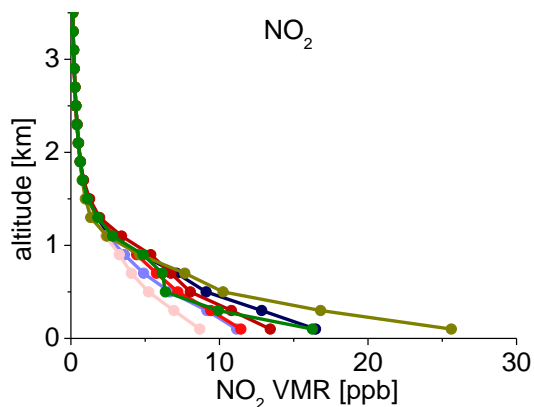
—●— low aerosols —●— high aerosols —●— cloud holes —●— broken clouds
 —●— continuous clouds —●— fog —●— thick clouds



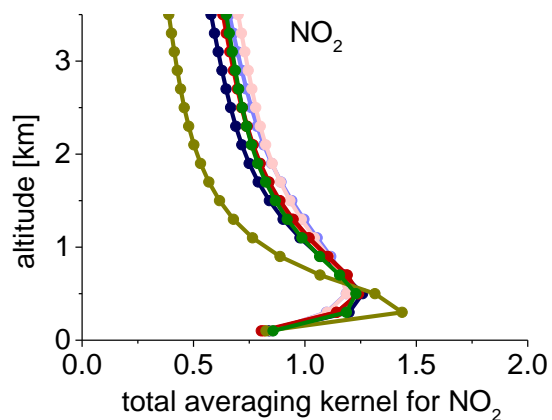
10



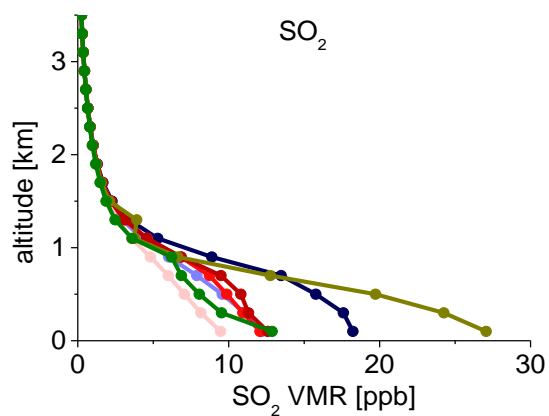
(c)



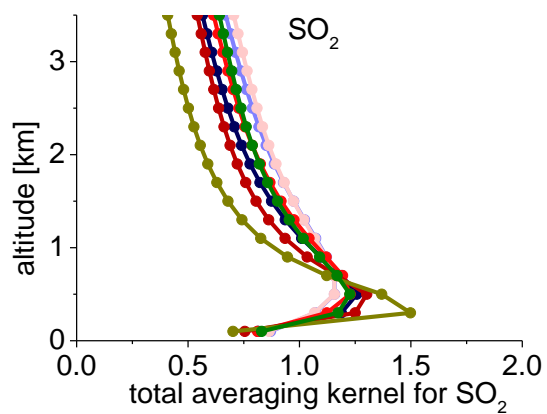
(d)



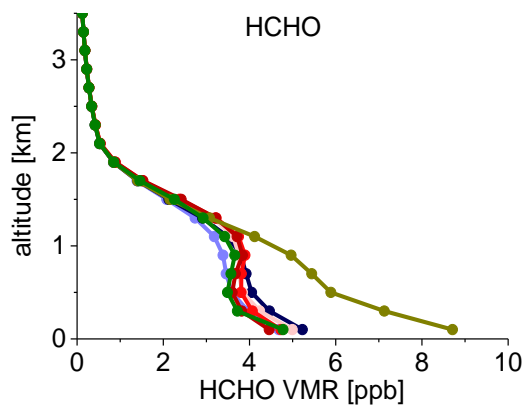
(e)



(f)



5 (g)



(h)

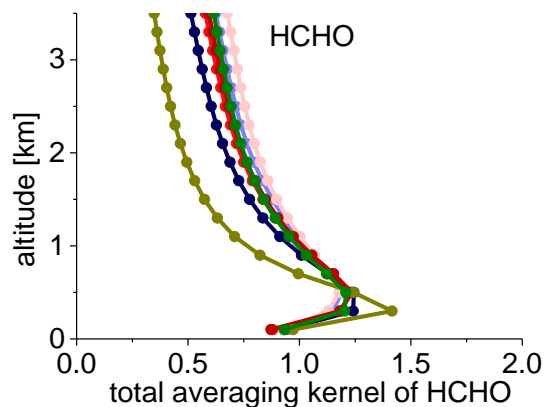
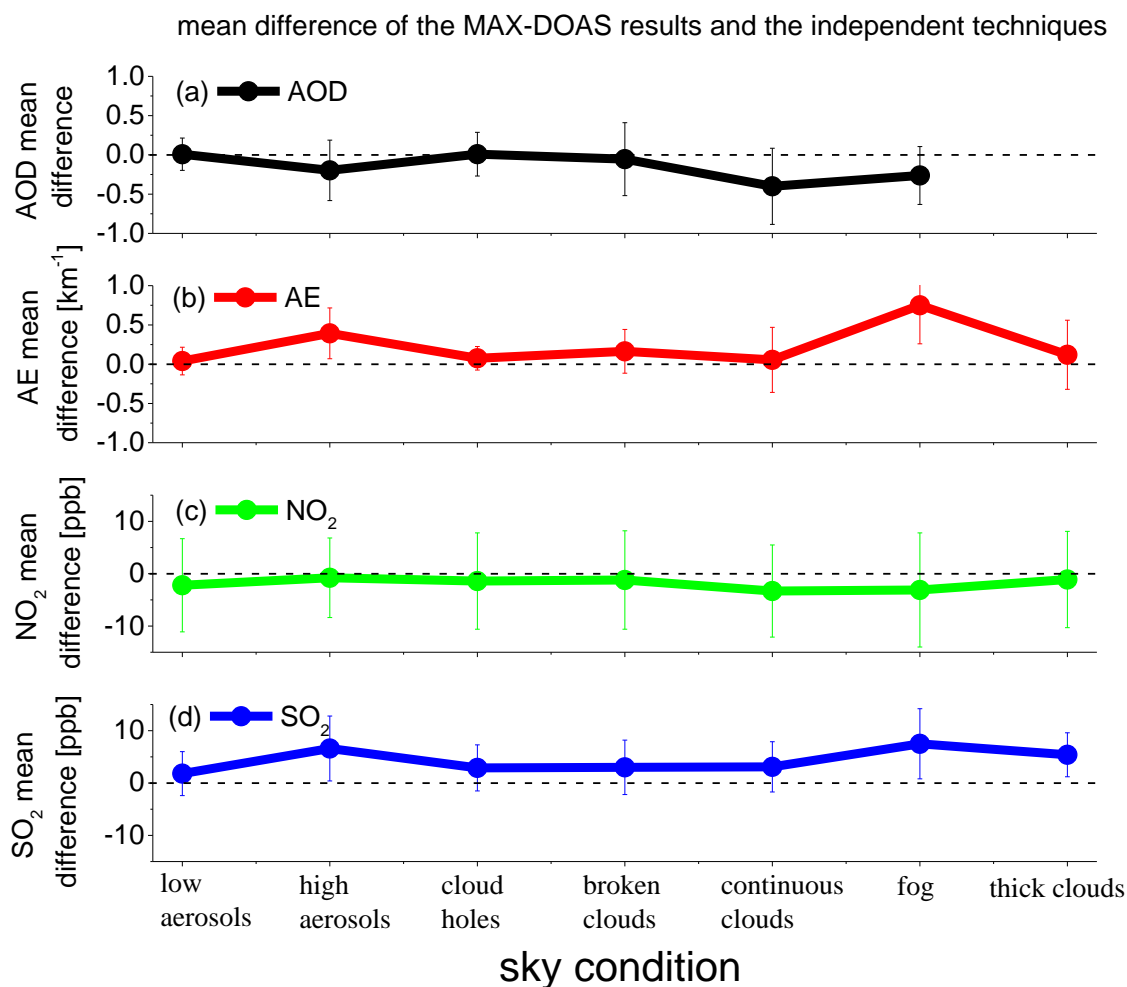




Figure 14: Mean profiles of aerosol extinctions (a), NO₂ VMRs (c), SO₂ VMRs (e) and HCHO VMRs (g) from all MAX-DOAS observations under individual sky conditions; the subfigures (b), (d), (f), (h) show the total averaging kernels of the four species under individual sky conditions.



5 **Figure 15:** Mean differences and the standard deviation (shown as the error bar) between MAX-DOAS results and independent techniques for different sky conditions. Different colours denote the values of AOD (compared with Taihu AERONET level 1.5 data sets), AE (compared with the visibility meter located nearby) and NO₂ and SO₂ (compared with the close long path DOAS instrument).

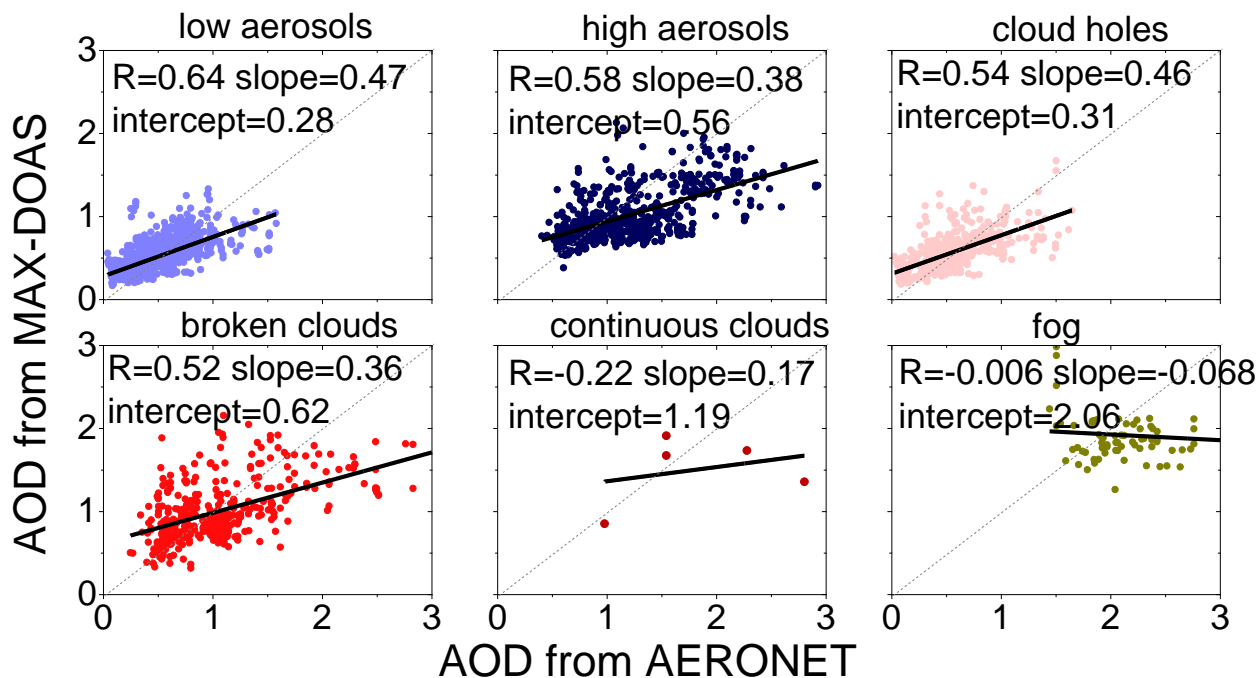
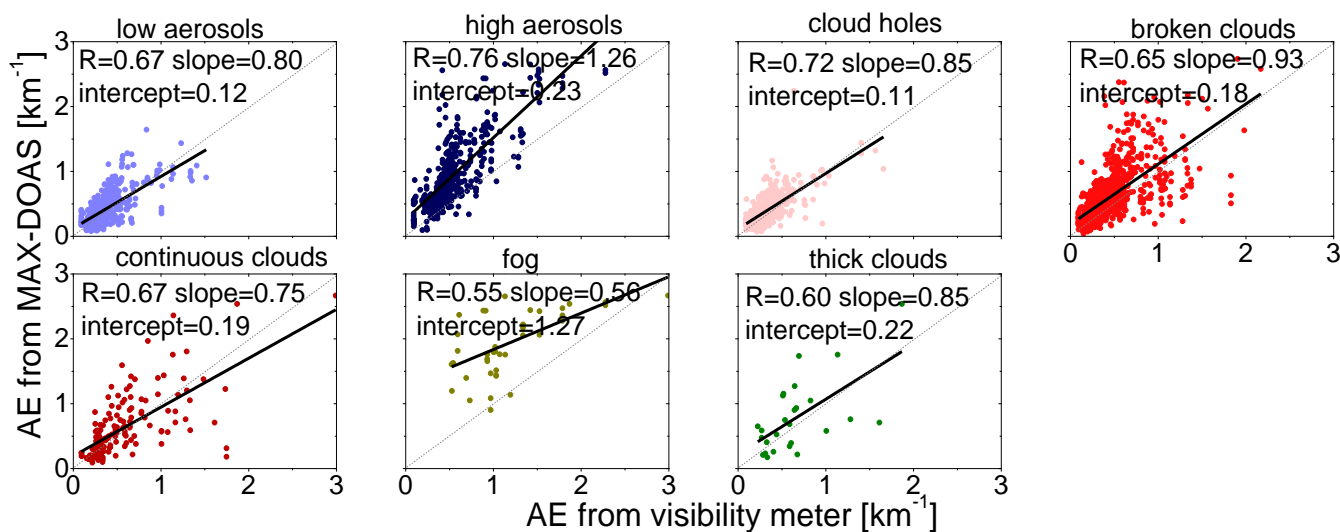


Figure 16: AODs derived from MAX-DOAS measurements in autumn are plotted against those from AERONET for different sky conditions. The linear regression parameters are shown in each subfigure. Note that no AERONET level 1.5 AOD data is available for thick clouds conditions because of the AERONET cloud screening scheme.



5

Figure 17: Same as Fig. 16 but for the comparisons of near surface aerosol extinctions with the visibility meter.

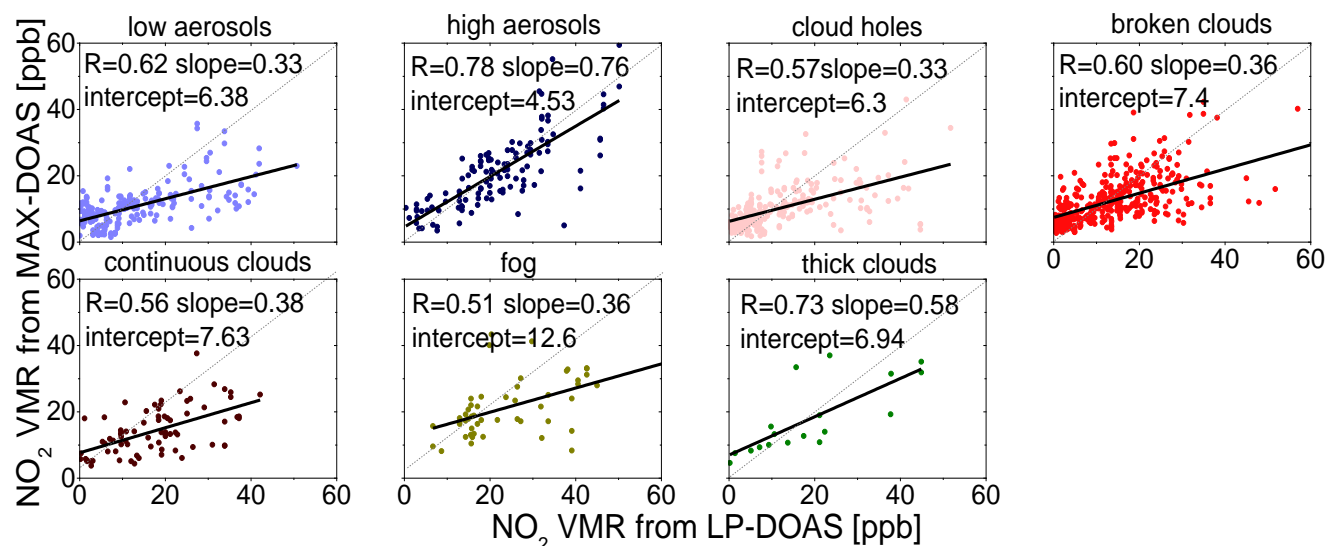


Figure 18: Same as Fig. 16 but for the comparisons of near surface NO_2 VMRs with the LP-DOAS.

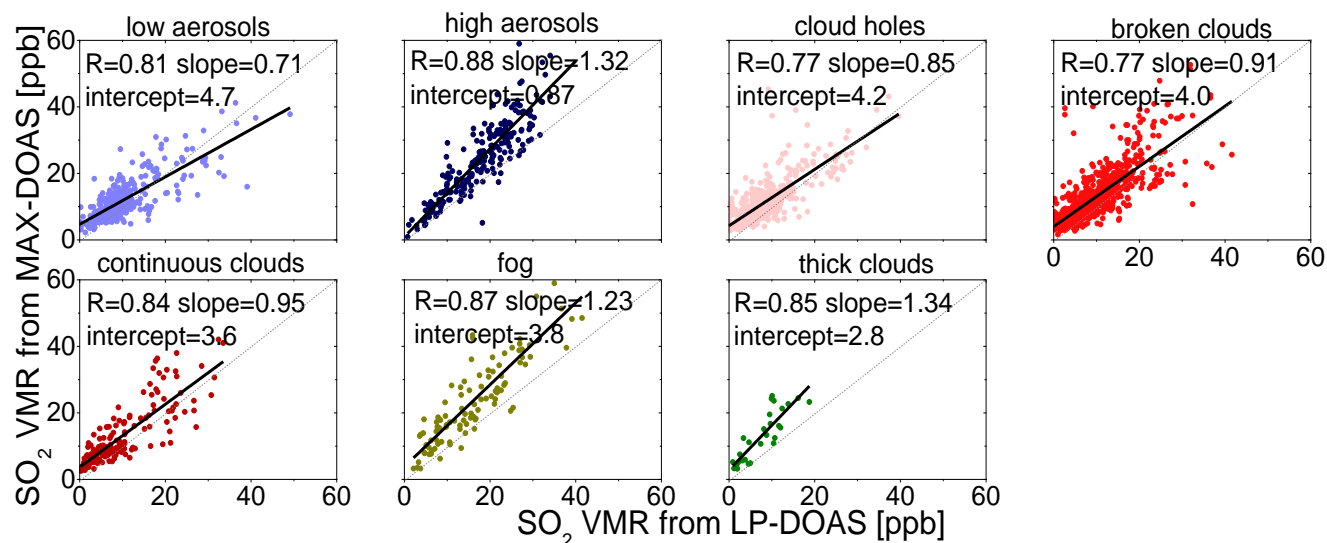
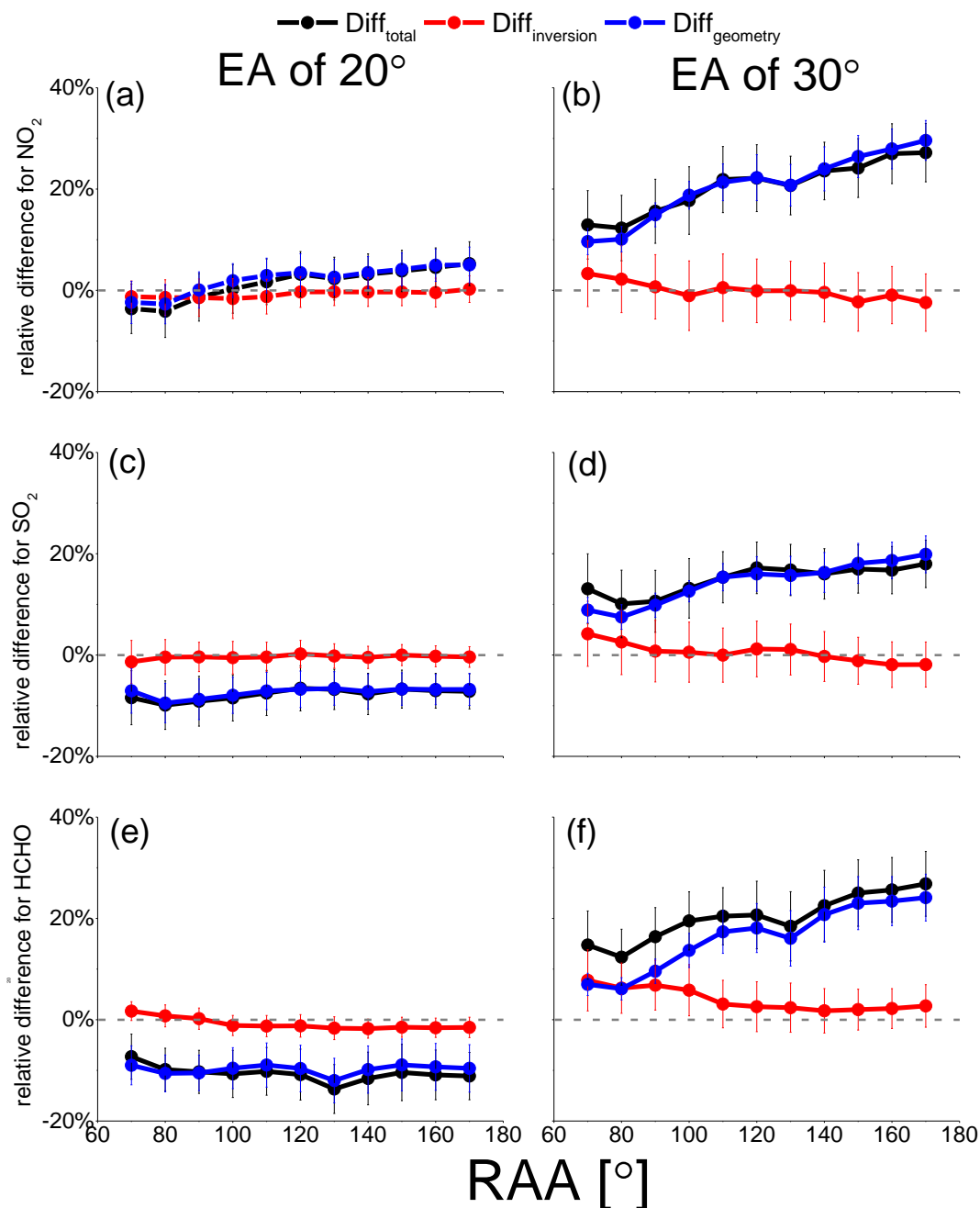
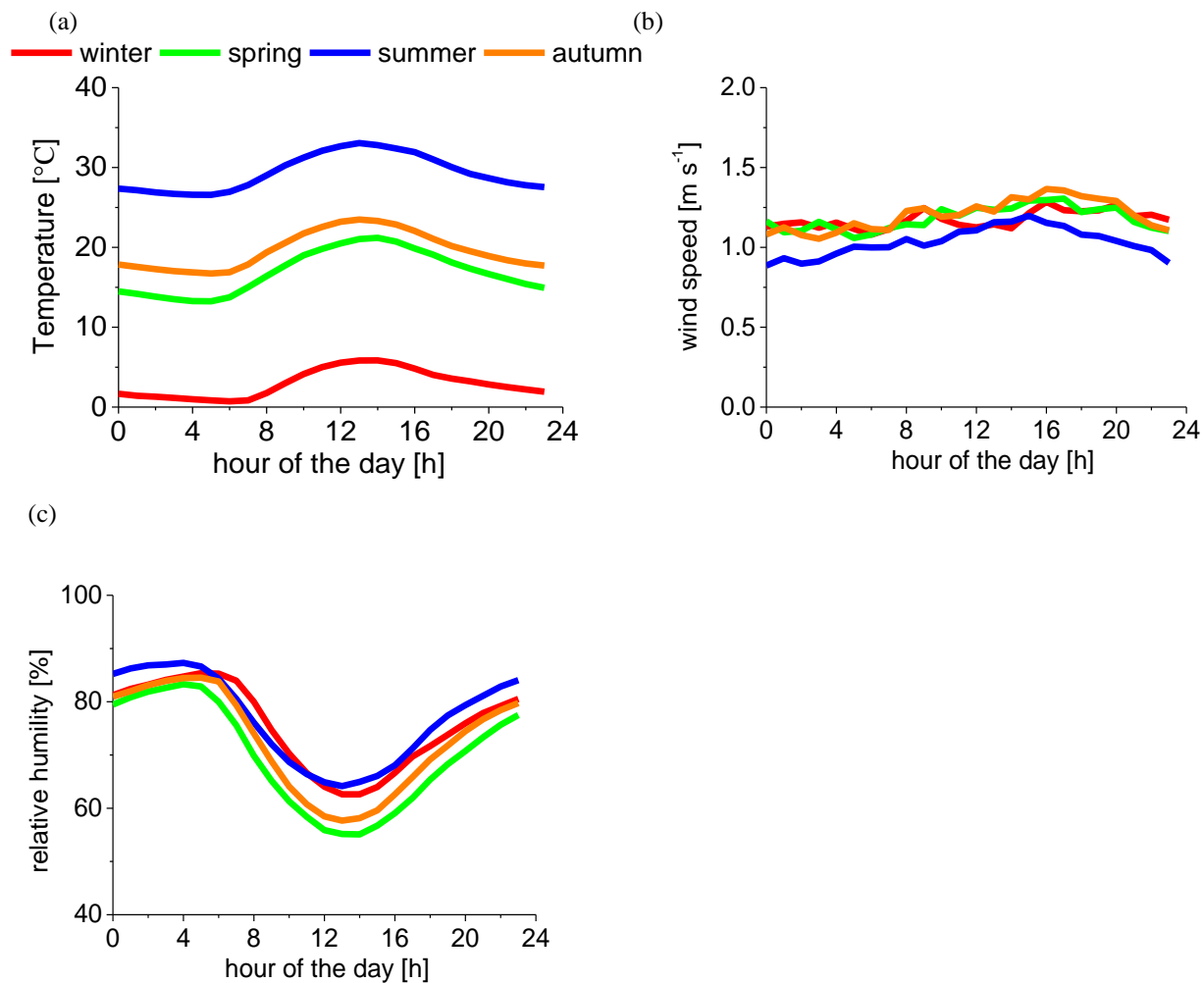


Figure 19: Same as Fig. 16 but for the comparisons of near surface SO_2 VMRs with the LP-DOAS.



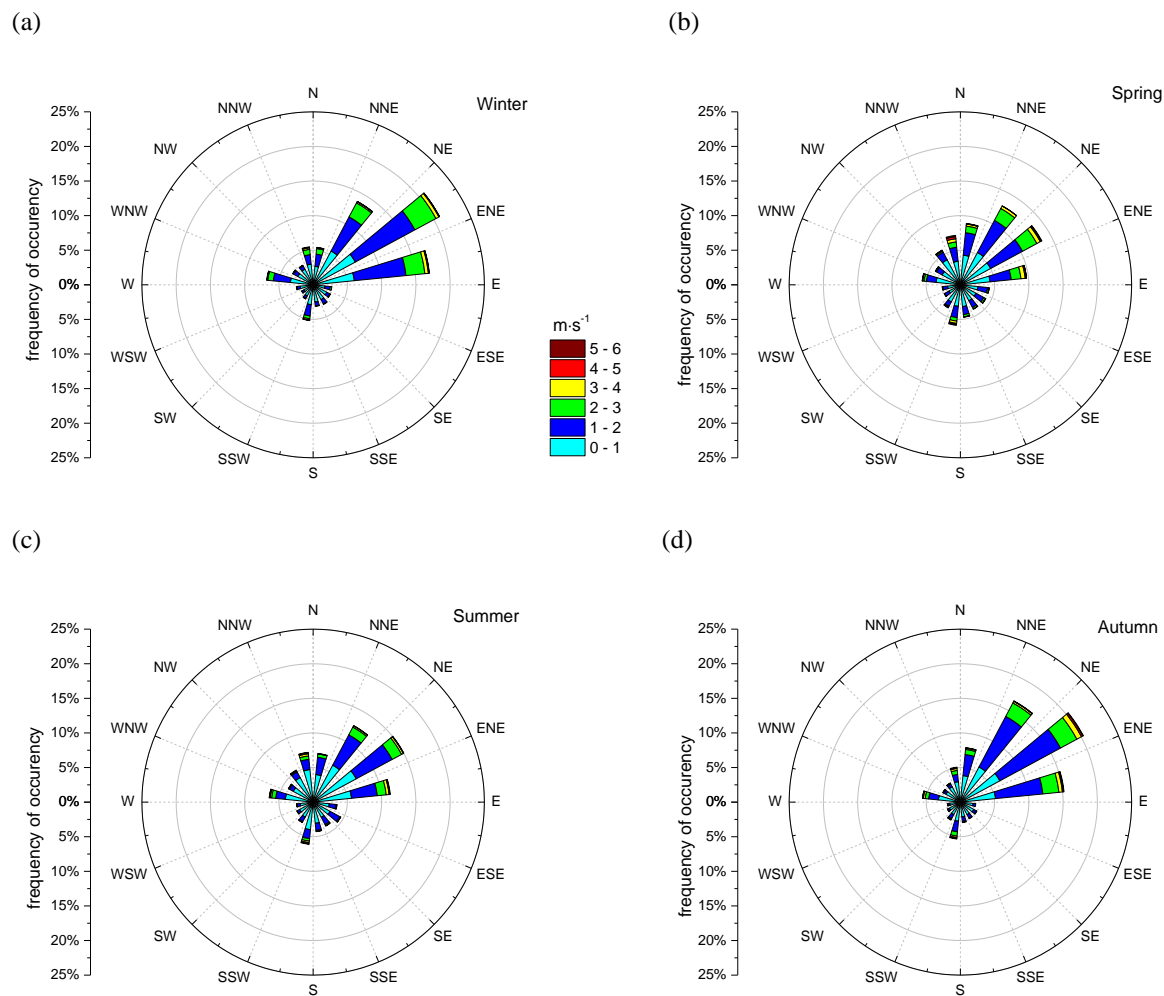
5 **Figure 20: Relative differences of the tropospheric NO₂ (top row), SO₂ (middle row) and HCHO (bottom row) VCDs derived by the geometric approximation and from the profile inversion ($Diff_{total}$, black dots) as function of the relative azimuth angle for elevation angles of 20 ° (left) and 30 ° (right). Also the differences caused by the errors of the profile retrieval ($Diff_{inversion}$, red dots) and of the geometric approximation ($Diff_{geometry}$, blue dots) are shown (see text).**



5 **Figure 21: Seasonally mean diurnal variations (2011 to 2014) of ambient temperature (a), wind speed (b) and relative humidity (c) obtained from the observations of the weather station nearby the MAX-DOAS instrument.**

10

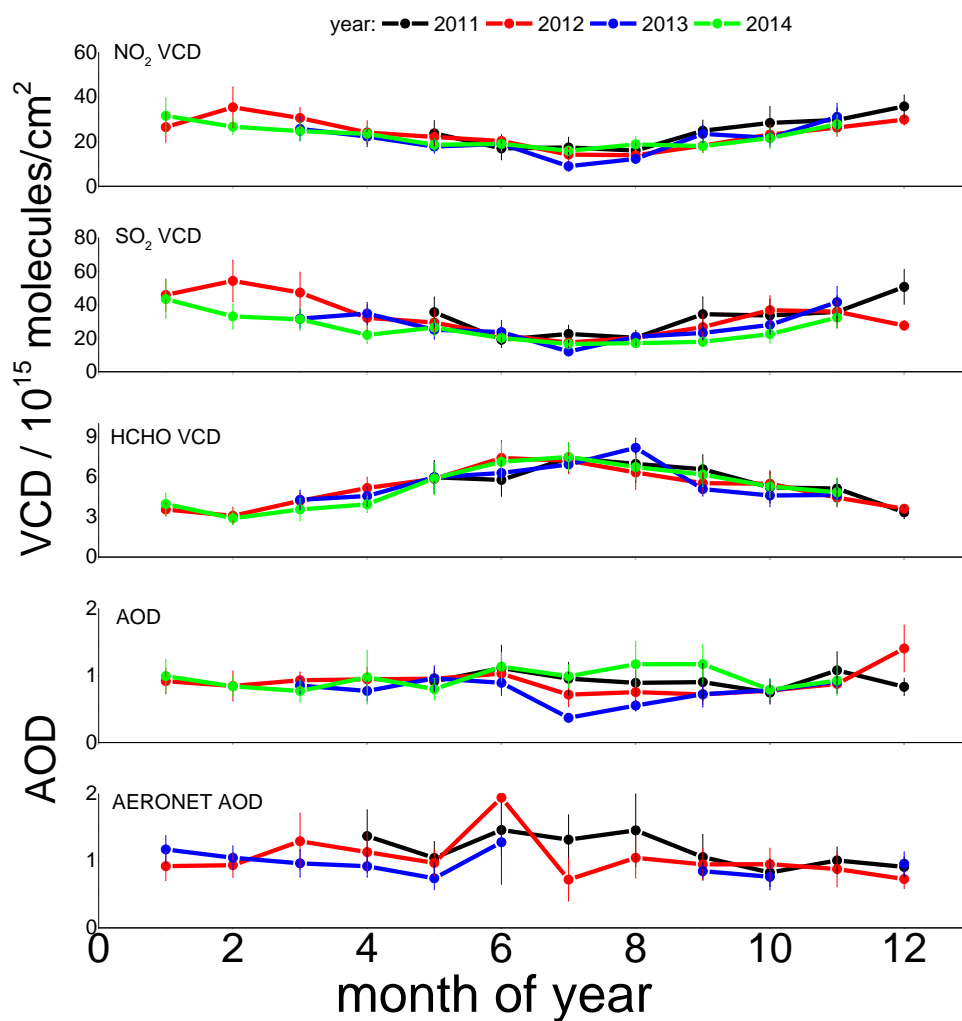
15



5 **Figure 22:** Wind rose diagrams based on all hourly averaged observations of the weather station for winter (a), spring (b), summer (c) and autumn (d) from 2011 to 2014.

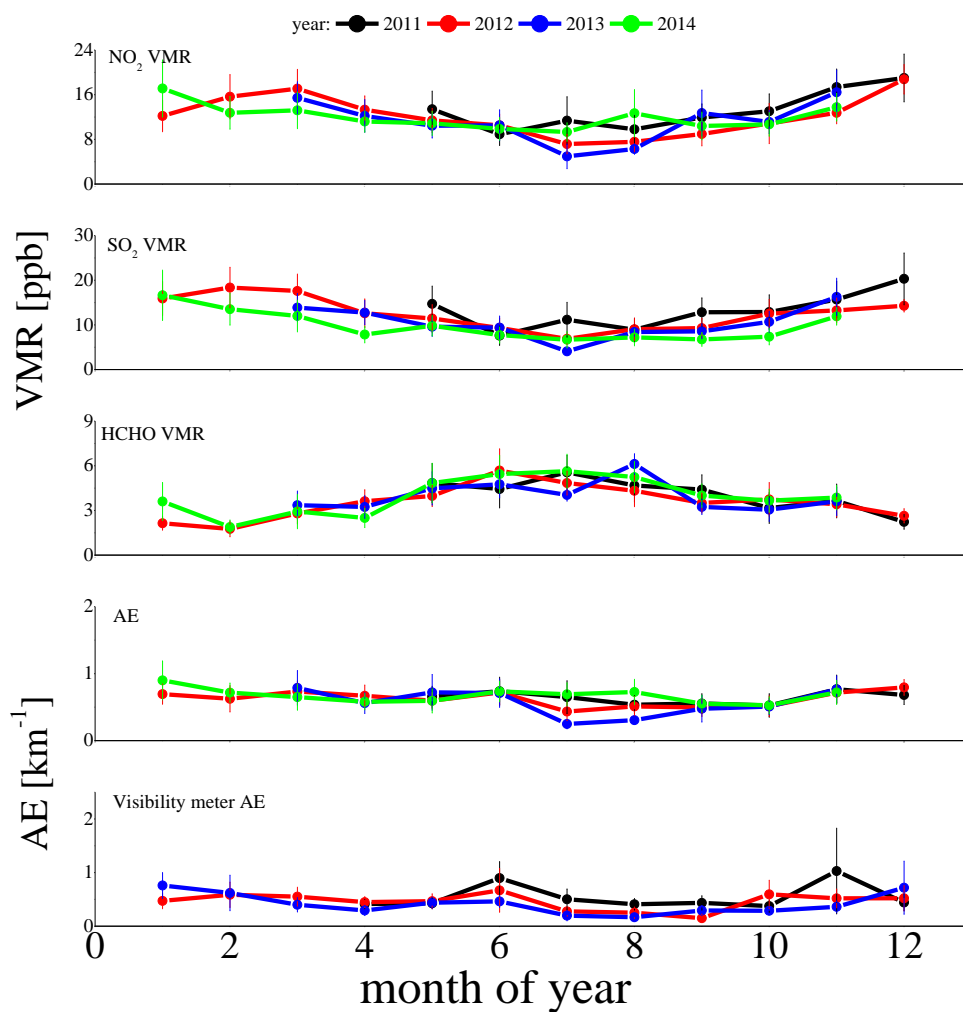


(a)





(b)





(c)

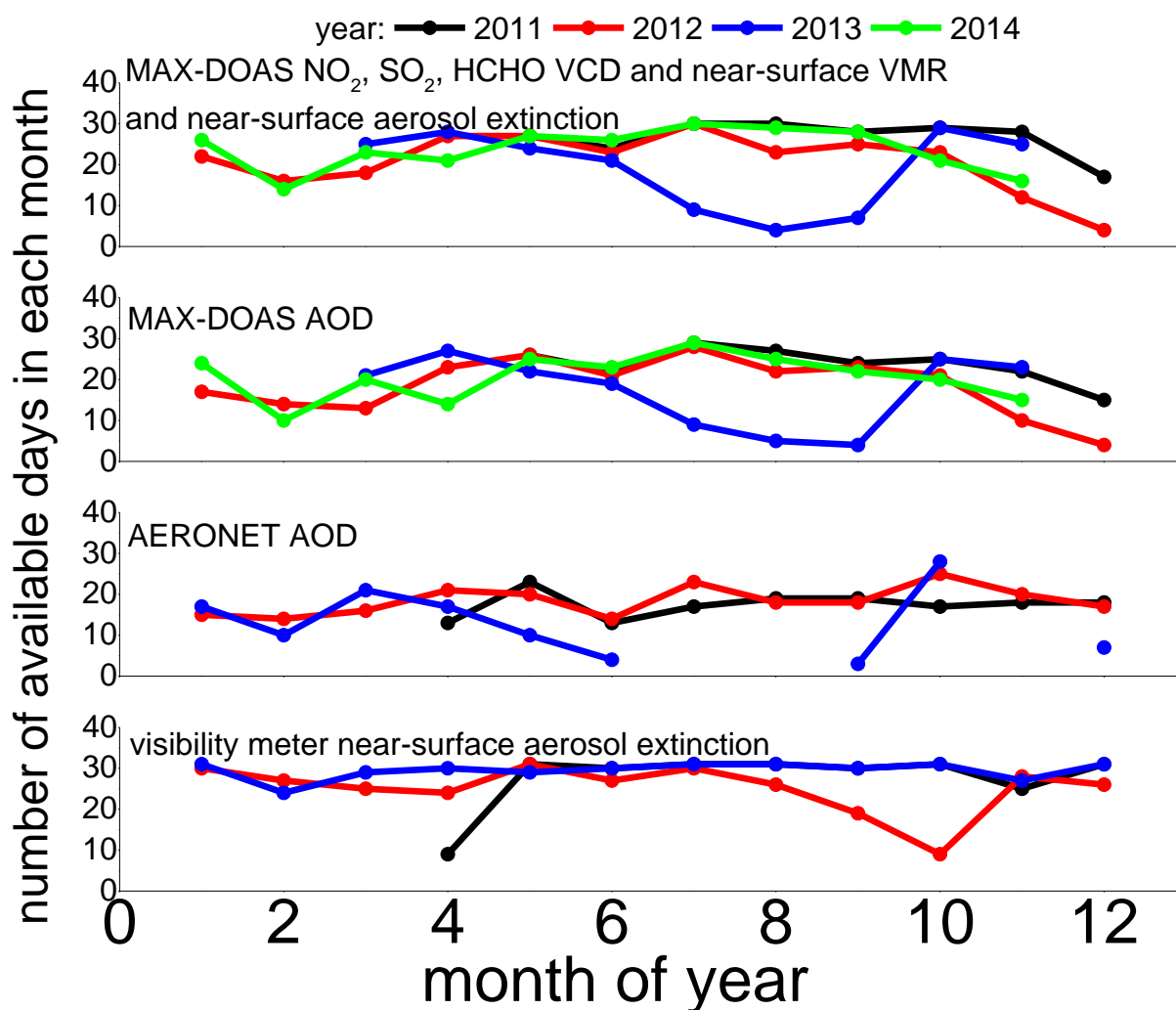


Figure 23: Seasonal cycle of monthly mean MAX-DOAS results: VCD and AOD (a), and near-surface VMR of NO₂, SO₂ and HCHO and AE (b) for May 2011 to November 2014. The error bars represent the standard deviations. In addition to the MAX-DOAS data also AOD and AE from AERONET and visibility meter are shown, respectively. The numbers of available days in each month for MAX-DOAS measurements, AERONET and visibility meter are shown in subfigure (c). The different numbers of available AOD and trace gas data derived from MAX-DOAS are caused by the filter scheme (see Table 3).

5

10

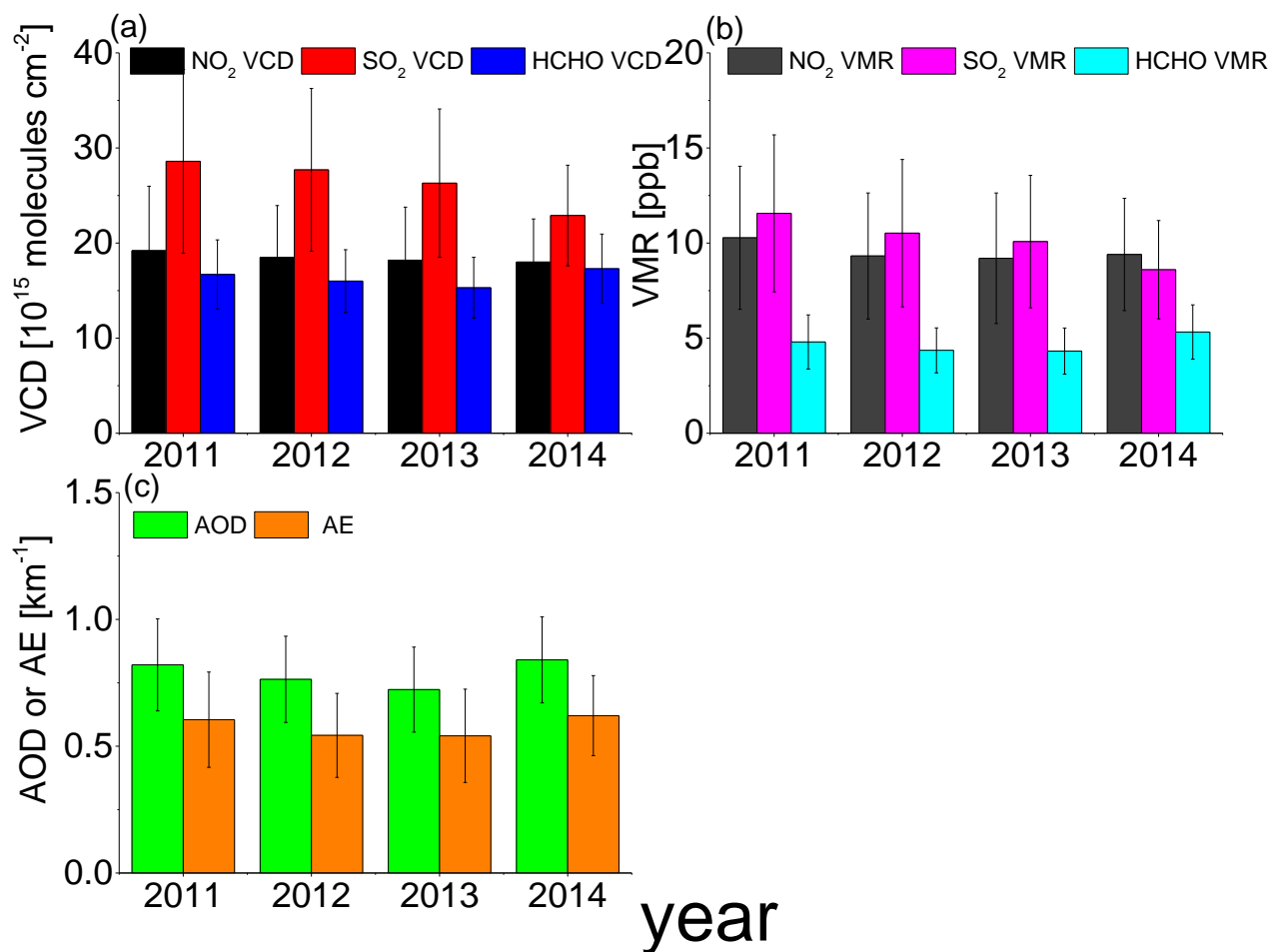


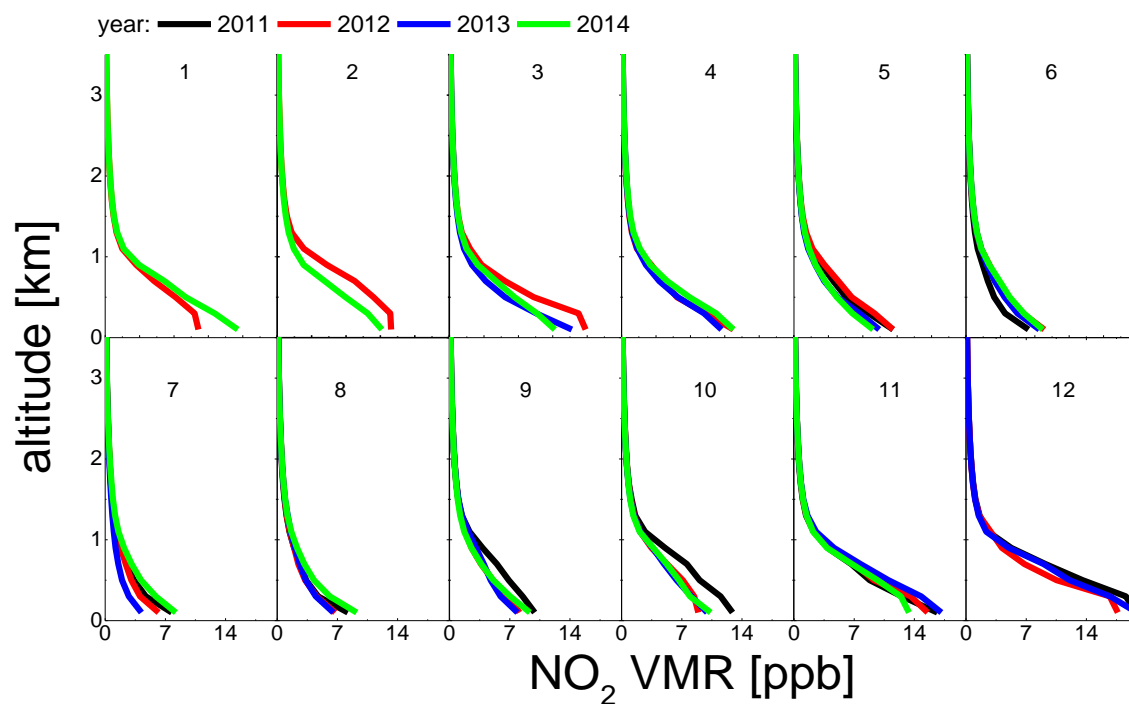
Figure 24: Mean (May to November) VCDs (a) and near surface VMRs (b) of NO₂, SO₂, HCHO as well as AODs and near surface aerosol extinctions (c) for each year.

5

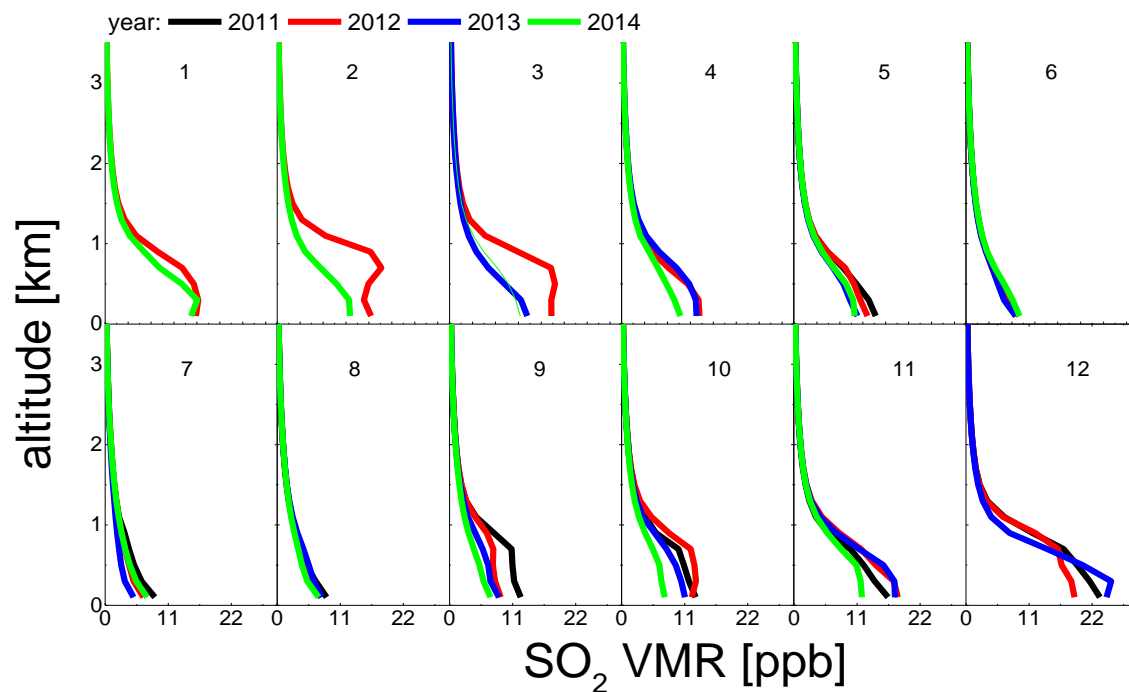
10



(a)

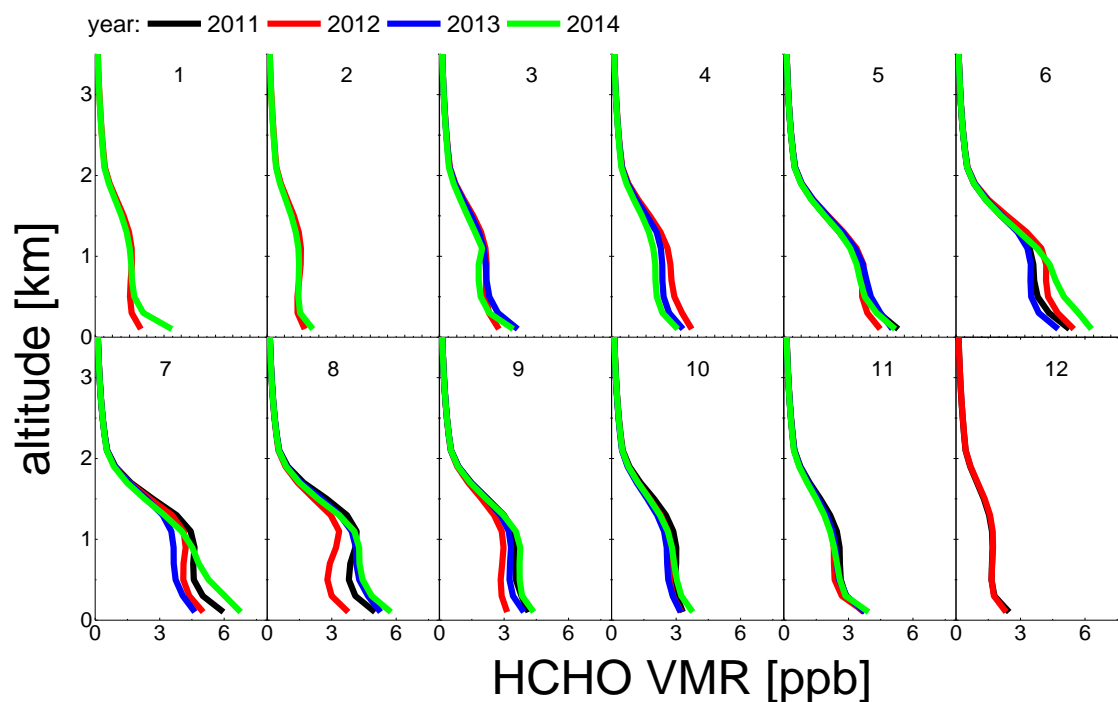


(b)





(c)



(d)

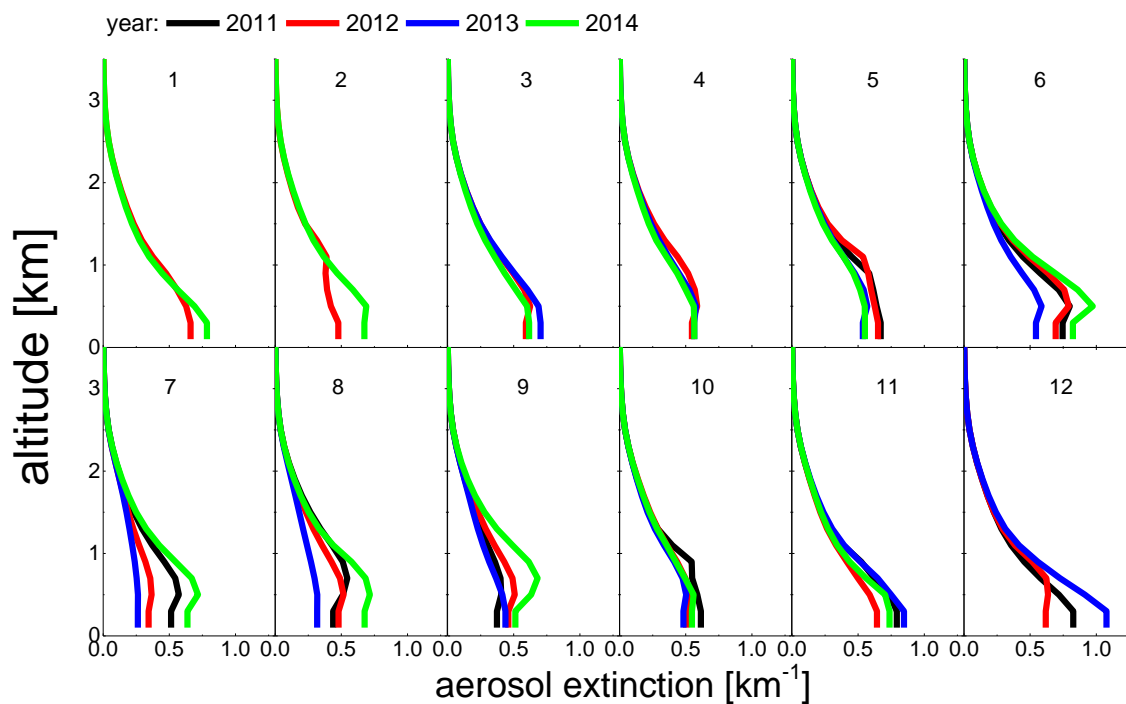




Figure 25: Monthly mean profiles of NO₂ (a), SO₂ (b), HCHO (c) VMRs (under clear and cloudy sky conditions except thick clouds and fog) and aerosol extinction (under clear sky conditions) (d) for May 2011 to November 2014.

2011: 2012: 2013: 2014:

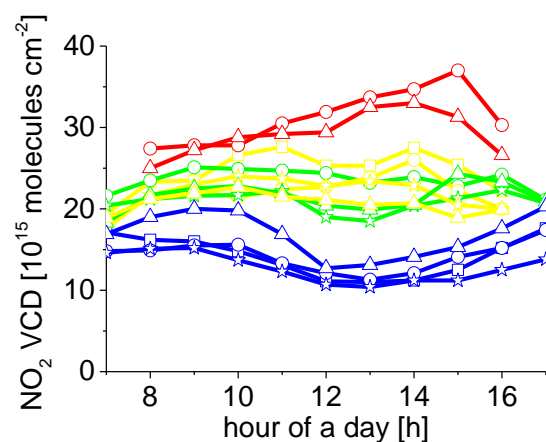
 ○ winter ○ winter ○ winter ○ winter

 ● spring ● spring ● spring ● spring

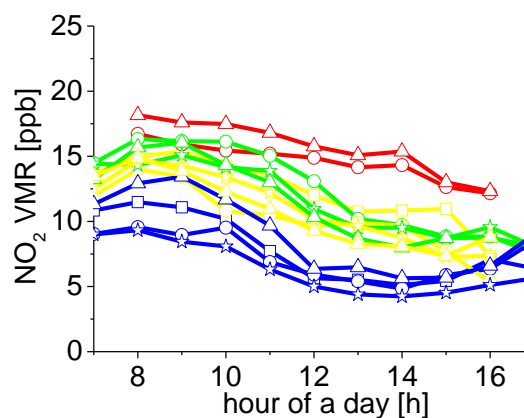
□ summer □ summer □ summer □ summer

□ autumn □ autumn □ autumn □ autumn

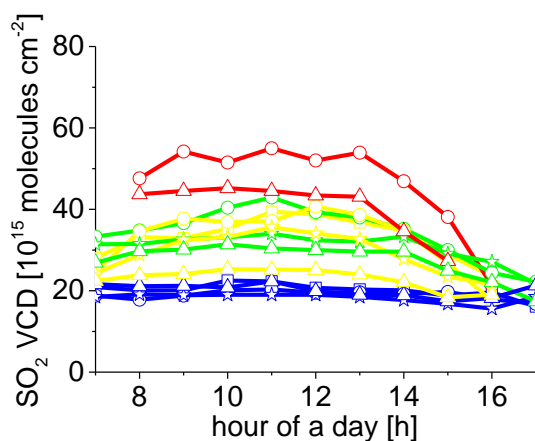
(a)



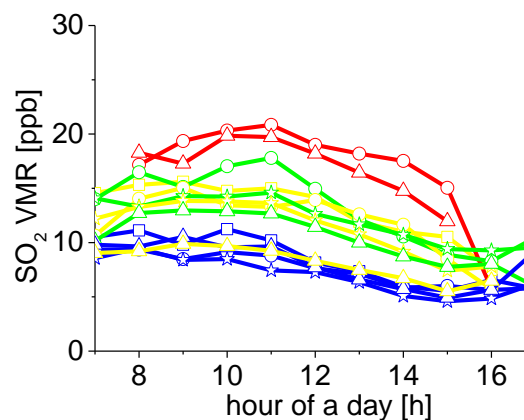
5

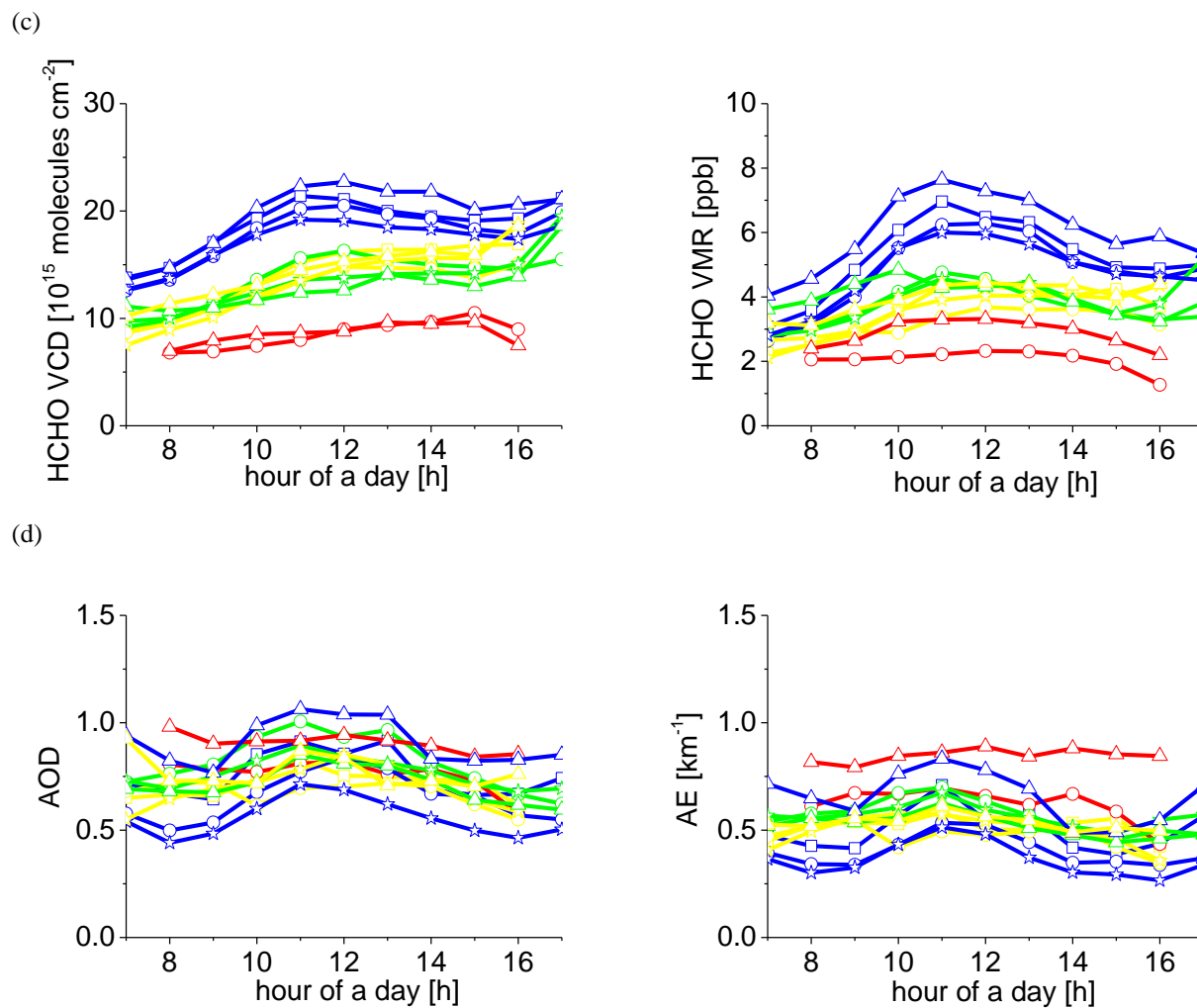


(b)

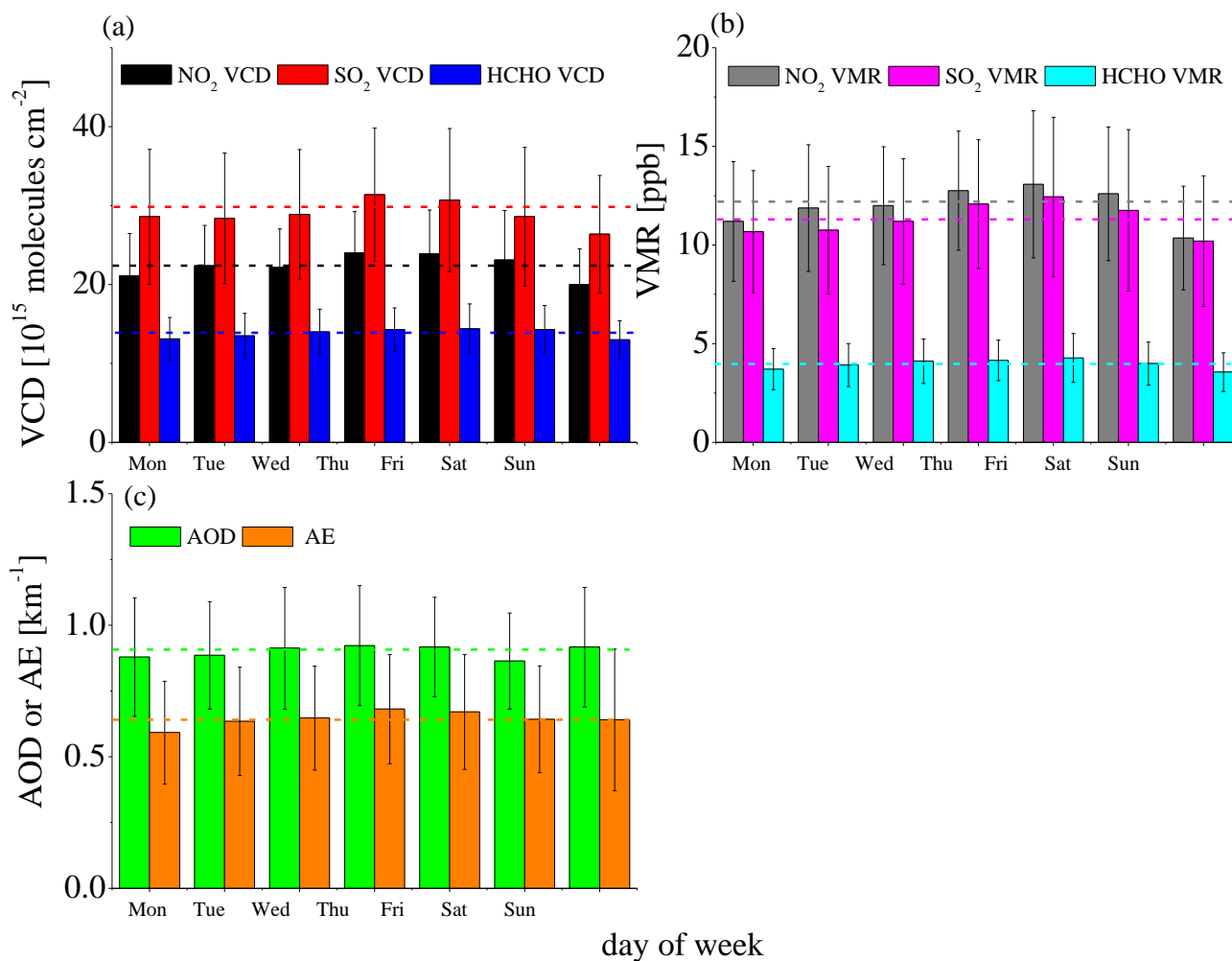


10





5 Figure 26: Seasonally averaged diurnal variations of TG VCDs and AOD (left) and near surface values (right) of NO_2 (a), SO_2 (b), HCHO (c) and aerosols (d) from 2011 to 2014.

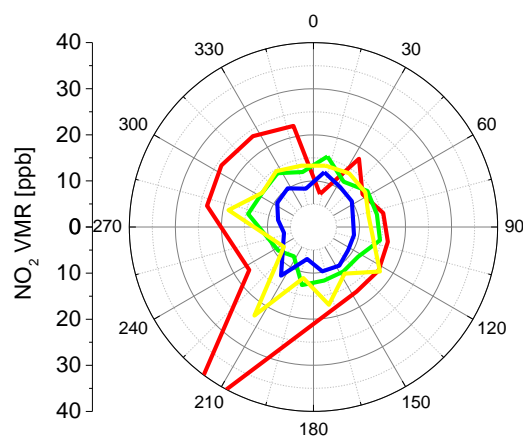
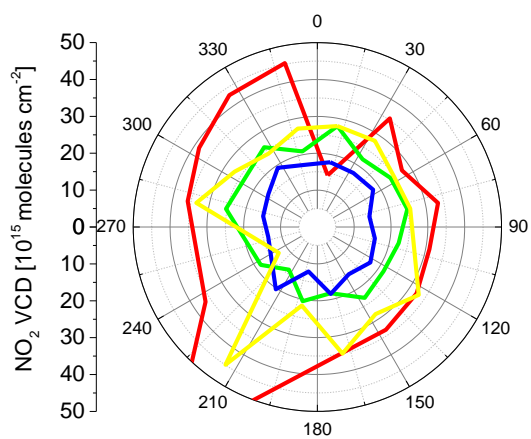


5 **Figure 27: Mean weekly cycles of VCDs (a) and near-surface VMRs (b) of NO₂, SO₂ and HCHO as well as the AODs and near-surface AEs (c) for all MAX-DOAS observations from 2011 to 2014. The dashed lines denote the mean values during the working days from Monday to Friday (same colours as for the daily averages).**

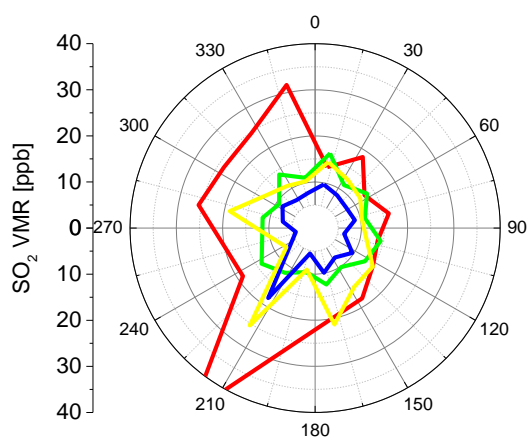
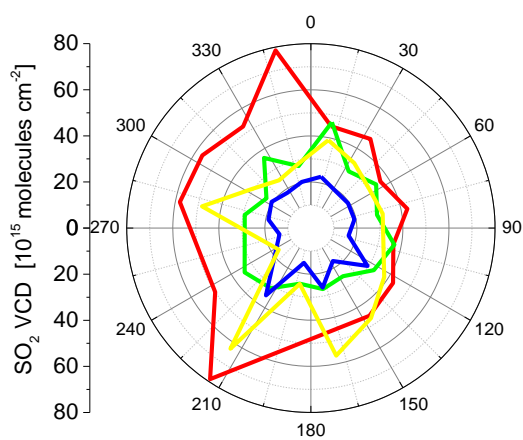


— winter — spring — summer — autumn

(a)



(b)

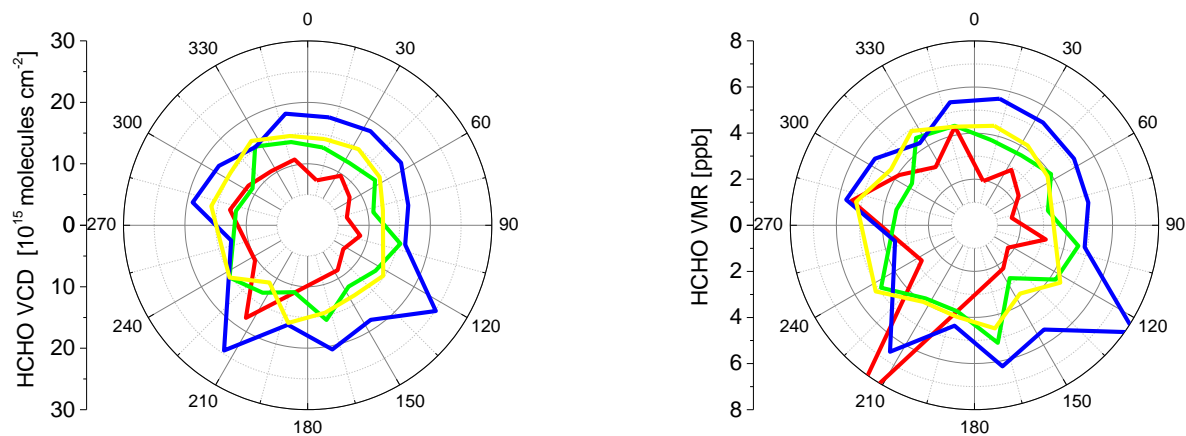


5

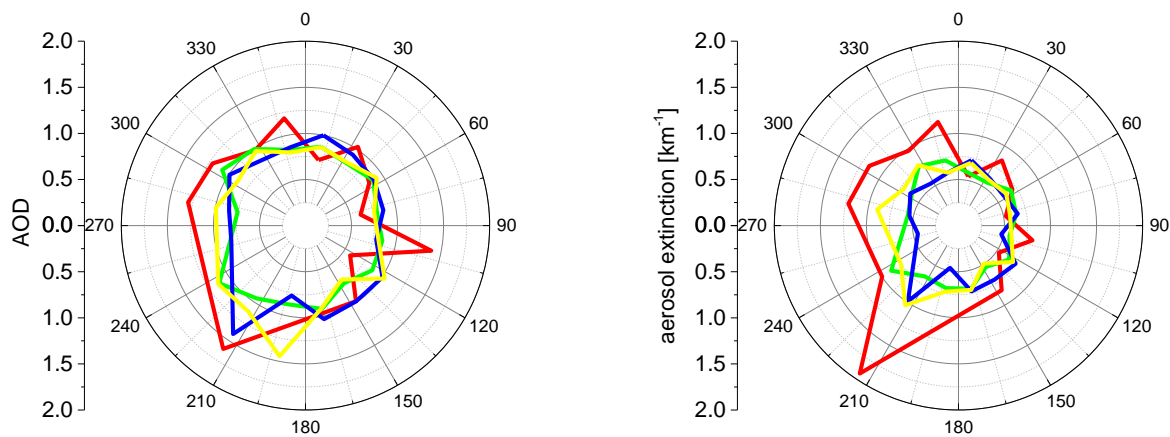
10



(c)



(d)



5 Figure 28: Dependencies of VCDs and AODs (left) and near-surface VMRs and AEs (right) of NO_2 (a), SO_2 (b), HCHO (c) and aerosols (d) on wind directions for individual seasons (different colours).

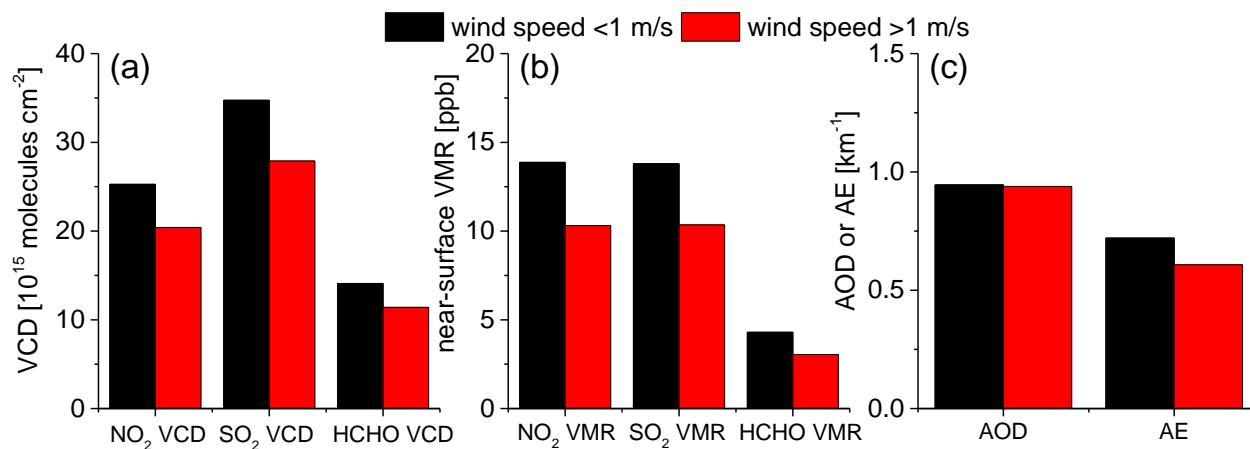


Figure 29: Comparisons of VCDs (a) and near-surface VMRs (b) of NO₂, SO₂ and HCHO, as well as AODs and near-surface AEs for different wind speeds (smaller than 1m/s or larger than 1m/s).